©2018

Hao Wang

ALL RIGHTS RESERVED

DESIGN AND SYNTHESIS OF MICROPOROUS METAL-ORGANIC FRAMEWORKS FOR ADSORPTION RELATED APPLICATIONS

by

HAO WANG

A dissertation submitted to the

School of Graduate Studies

Rutgers, The State University of New jersey

In partial fulfillment of the requirements

For the degree of

Doctor of Philosophy

Graduate Program in Chemistry and Chemical Biology

Written under the direction of

Jing Li

And approved by

_____

_____

_____

_____

New Brunswick, New Jersey

May, 2018

ABSTRACT OF THE DISSERTATION

Design and Synthesis of Microporous Metal-Organic Frameworks for Adsorption Related Applications

By HAO WANG

Dissertation Director:

Jing Li

Metal-organic frameworks (MOFs), constructed via self-assembly of metal ions (or clusters) and organic ligands through coordination bonds, represent a relatively new family of multifunctional porous materials. MOFs feature high porosity, tunable pore structure (pore size and pore shape) and functionality, making them hold great promise for adsorption related applications. Utilizing MOFs for industrially relevant adsorption related applications are explored.

With the strategy of topology directed design and synthesis, a series of Zr-MOFs with intriguing structure features have been achieved. They exhibit high porosity, good stability and optimal pore structure for separation of alkane isomers. Their ability of separating C6 alkane isomers, which is industrially critical for octane number upgrading of gasoline, outperforms the commercially used material zeolite 5A.

The feasibility of utilizing MOFs for adsorptive separation of noble gases has also been studied. After screening of a number of MOFs, a microporous MOF built on Co^{2+} and formate has been identified to show highly selective adsorption of Xe over Kr. In a separate work, we try to understand the interaction between noble gases and a flexible MOF structure from molecular level via single crystal X-ray diffraction. Noticeably, the framework exhibits an unprecedented temperature-dependent breathing phenomenon upon noble gas adsorption.

We have also evaluated the possibility of using MOFs in food chemistry. A moisture-sensitive MOF has been synthesized, which exhibits high uptake capacity and moisture-triggered controlled release of a natural food preservative. The mechanism of controlled release has also been investigated.

Other adsorption related applications such as chlorocarbon capture by highly hydrophobic MOFs have also been explored.

ACKNOWLEDGEMENTS

First of all, I would like to take this opportunity to express my deepest gratitude to my advisor, Prof. Jing Li, who has been an excellent role model as a scientist. Without her diligent mentorship, considerate support and insightful suggestions I would not be able to complete this task. Her dedication and enthusiasm in scientific research have constantly encouraged me to overcome the hurdles I have encountered and will continue benefit me in my future carrier.

I would also like to thank my advisory committee members, Prof. KiBum Lee, Prof. Deirdre O'Carroll, and Dr. Long Pan for their generous support and valuable suggestions; my previous and current group members, especially Dr. David H. Olson, Dr. Haohan Wu, Wei Liu, Dr. Sujing Wang, Dr. Jingming Zhang, Dr. Xiao Zhang, Dr. Debasis Banerjee, Dr. Qihan Gong, Dr. Zhichao Hu, Dr. Kecai Xiong, Dr. Feng Xu, Dr. Baiyan Li, Prof. Qibin Xia, Prof. Litao An, Benjamin J. Deibert, Yang Fang, Nathan D. Rudd, William Lustig, Yanyao Liu, Kun Zhu, Qianyou Wang, Junjie Peng, Xuan Qiu, Peiyao Du and Qining Wang whom I worked with closely; my collaborators around the world, especially Dr. Kui Tan, Dr. Xinglong Dong, Dr. Simon J. Teat, Dr. Jagiello Jacek, Dr. Stephanie Jensen; my friends at Rutgers and everyone else who helped in any way during the past five years.

Last but not least, I want to thank my parents for their love and support.

TABLE OF CONTENT

List of Tables

List of Figures

1. Introduction

1.1 Gas adsorption on porous materials

Adsorption is the enrichment of one or more compounds in an interfacial layer.[1] In this dissertation we consider gas adsorption on gas/solid interface where the solid is called adsorbent and the gas, which is being adsorbed, is called adsorbate. Adsorption processes can be divided into two categories of chemisorption and physisorption depending on the strength of the interaction. Chemisorption involves formation of chemical bonding between adsorbate and the solid surface, which is characterized by large interaction potentials. In contrast, physisorption, which is the focus of this dissertation, takes place through van der Waals's forces and is a reversible process with low heat of adsorption.

Gas adsorption has been widely employed as a powerful technique for the characterization of solids with regard to their surface area, pore size, pore volume, and density. With the development of porous solids over the past decades, gas adsorption has been proposed as a promising approach for addressing various energy and environment related issues. We take hydrogen storage and hydrocarbon separation as examples. Hydrogen has an energy density greater than gasoline and it emits no carbon dioxide after burning, making it one of the most promising candidates for the replacement of current carbon-based energy sources. However, the use of hydrogen as a fuel in automobiles requires the storage of a large liquid or pressurized hydrogen tank on board the vehicle which is neither safe nor practical. Thus the U.S. Department of Energy (DOE) has set up the targets for on-board hydrogen storage systems. A wide range of materials have been tested for hydrogen storage including metal hydrides,[2] clathrates,[3] inorganic nanotubes,[4] and porous solids represent one of the most promising candidates.[5,6] Hydrocarbon separation represents a critical

process in petrochemical industry. Various hydrocarbon mixtures which include olefin/paraffin, alkane isomers need to be separated to produce high quality gasoline, plastics and a number of other chemical products.[7] Traditional technique for hydrocarbon separation is distillation which is highly energy-intensive. Adsorptive separation with porous solids such as zeolites has shown great advantage with respect to energy efficiency and carbon dioxide emission over distillation. Therefore, gas adsorption related techniques represent safe, energy-efficient, and environmentally-benign approaches over traditional techniques. This, in turn, spurs the development of porous solids to meet the requirement for various applications.

1.2 MOFs: synthesis, structure, and application

Since the late 1990s when they were first reported, metal-organic frameworks (MOFs) have become one of the most extensively studied fields in Chemistry and materials science.[8-10] MOFs comprise of inorganic nodes (metal ions or clusters) which are linked by organic ligands through coordination bonds forming coordination networks that contain potential voids.[11] Since the structure of a MOF depends on its metal and organic ligand, there can be essentially unlimited number of the combinations and thus MOFs show a wide structural diversity.[12,13] MOFs bring together the features of the metal ions/clusters, the organic ligands, and also the resulting framework and thus they usually exhibit intriguing properties and they represent a promising family of materials for multifunctional applications.

Synthesis: MOFs are usually prepared through hydrothermal/solvothermal reactions at elevated temperatures ranging from 60 °C to 200 °C. The reaction media can be water or a variety of organic solvents such as DMF, DMA, alcohols, ketones, amines or a combination of two or three of these solvents.[14] For some MOFs, one or multiple modulators are needed

during the synthesis in order to obtain high quality crystalline products. Some other synthetic methods have also been developed for the preparation of MOFs which includes slow evaporation/diffusion, microwave synthesis, mechanical grinding etc.[15,16] Despite the fact that thousands of MOFs have been synthesized and characterized, the synthesis of MOFs especially those built on high valent metals such as Zr^{4+}, Ti^{4+}, Al^{3+}, Cr^{3+} remains challenging.

Structure: One of the most intriguing features of MOFs is their structural diversity.[17-19] The structure of a MOF is the result of the metal, the ligand or the combination of ligands, and the synthetic condition. The resulting structure depends on the inorganic building units, the geometry of the organic ligands, and their linking mode. A metal can form different inorganic building units in MOFs depending on the organic ligands and preparation conditions. For example, Zn^{2+} can form primary building units (PBUs, mononuclear metal center), or secondary building units (SBUs, polynuclear metal centers, can be a dimer, trimer, or tetramer etc.). Zr^{4+} usually forms Zr_6O_8 clusters with few exceptions. In Figure 1 we show the structure of some porotype MOFs and their building blocks.

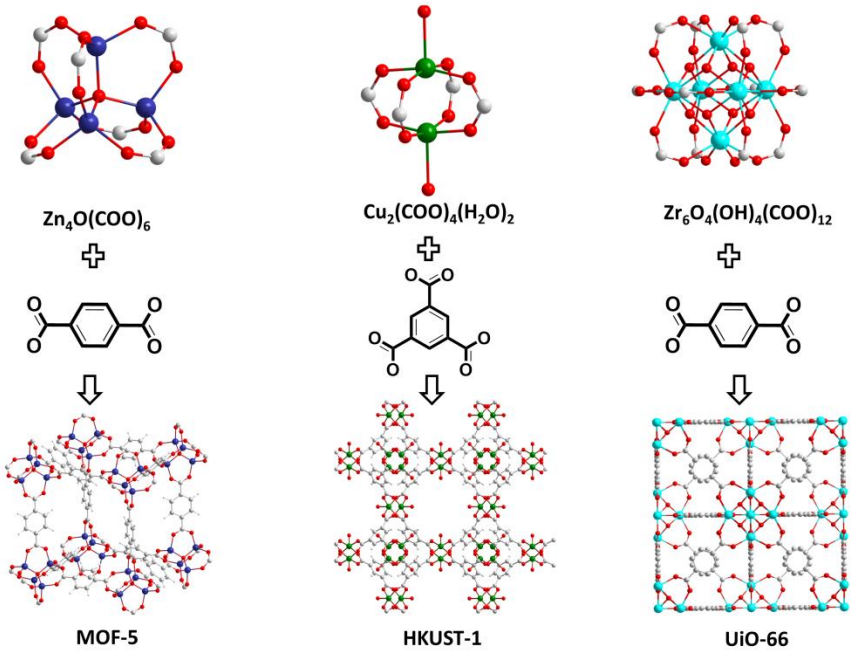

Figure 1. SBUs, organic ligands and crystal structure of three porotype MOFs.

Application: MOFs have been extensively investigated for various applications. These potential applications are related to their intriguing properties and these properties originate from the incorporated metal, or the organic ligand, or the resulting framework. Gas storage relies on the high porosity of MOFs.[20-22] MOFs show highly tunable pore structure and functionality which is advantageous for molecular separation.[20,23,24] MOFs incorporating luminescent metals or ligands may be emissive which can be used as phosphors or for chemical sensing.[25-27] Other applications include catalysis,[28,29] proton conductivity,[30,31] and drug delivery,[32,33] to name a few.

1.3 Adsorption based applications in MOFs

Among many attractive properties of MOFs, the most intriguing one would be their high porosity and tunable pore size/shape/functionality. By judicious design/selection of metals and organic ligands, and optimization of synthetic conditions, one can possibly obtain MOFs with targeted structure possessing expected porosity and pore functionality.

For gas storage: As one of the most promising porous solids for gas storage, MOFs have shown great potential in hydrogen storage and methane storage. By taking advantage of reticular chemistry, researchers are able to construct MOFs with exceptionally high porosity (BET surface area > 7000 m^2/g).[34] However, gas storage performance of MOFs is not always positively correlated to their porosity. For example, by looking into methane storage studies on a number of MOFs, we found the storage capacity (at ambient temperature and 65 bar) goes through a maximum as the BET surface area of MOFs increases (Figure 2) and the best performing MOFs possess BET surface area of 2000 – 3000 m^2/g.

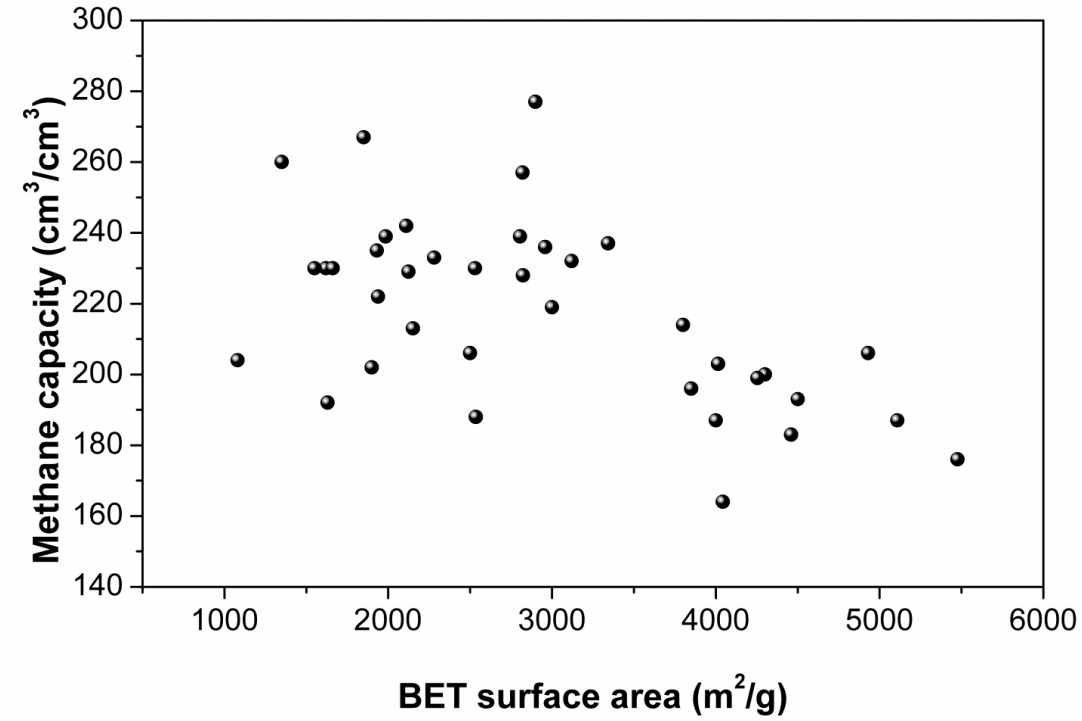

Figure 2. The correlation of methane storage capacity (at ambient temperature and 65 bar) and BET surface area of MOFs.

For molecular separation: MOFs show great advantage for molecular separation due to their highly tunable pore size, pore shape, and the functionality of pore surface.[35] For

example, by amine grafting on the uncoordinated metal centers in MOFs, one can enhance their selective carbon dioxide adsorption performance.[36-38] By fine-tuning the pore size of a series of isoreticular MOFs with ligands with different length, one can possibly realize separation of different adsorbates with different molecular size through selective size sieving.[39,40] As of today, MOFs have shown exceptional performances for certain industrially relevant separations which surpass any other porous materials. For example, Eddaoudi and coworkers have achieved clean separation of propane and propylene with a microporous MOF.[39]

For other adsorption related applications: A number of other adsorption related applications have been explored with MOFs making use of their unique structural properties. By taking advantage of the water sensitivity of a microporous MOF, controlled release of fragrance molecules from the MOF pore can be realized.[41] Also, by incorporating sulfur containing organic ligands, one can use MOFs for heavy metal removal from aqueous solution.[42]

2. Topologically guided design and synthesis of robust microporous Zr-MOFs for effective separation of alkane isomers

2.1 Background: alkane isomers separation

The separation of alkane isomers represents one of the most important and challenging tasks in petrochemical industry.[43] During oil refinement, alkanes are subject to catalyzed isomerization reactions resulting in linear alkanes and their isomers of different degree of branching (mainly C5 and C6).[44] These alkane isomers need to be separated as a function of their research octane number (RON). For example, in order to obtain gasoline of high quality, linear hexane (RON = 25) need to be separated from its branched isomers which have higher RON (See Table 1).

Table 1. RON of selected fuel components.

Fuel	RON
n-hexane	25
3-methylpentane	70
2,3-dimethylpentane	105
n-heptane	0
2-methylhexane	44
2,2,3-trimethylbutane	112
2,2,3-trimethylpentane	106

Current large scale industrial separation of alkane isomers relies on heat-driven distillation which is energy and capital intensive. Adsorptive separation by porous solids has been

proposed as a promising alternative to distillation for the separation of alkane isomers. Compared to distillation, adsorptive separation can not only offer higher energy efficiency, it will also emit less carbon dioxide.

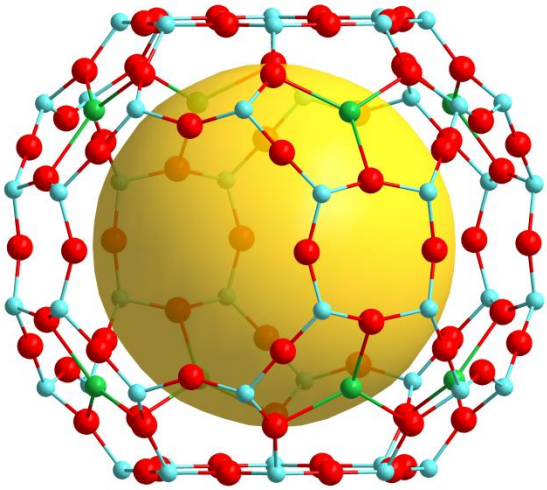

Figure 3. Structure of zeolite 5A. Yellow sphere indicates its cavity. Color scheme: cyan: Al/Si, red: O, green: Na

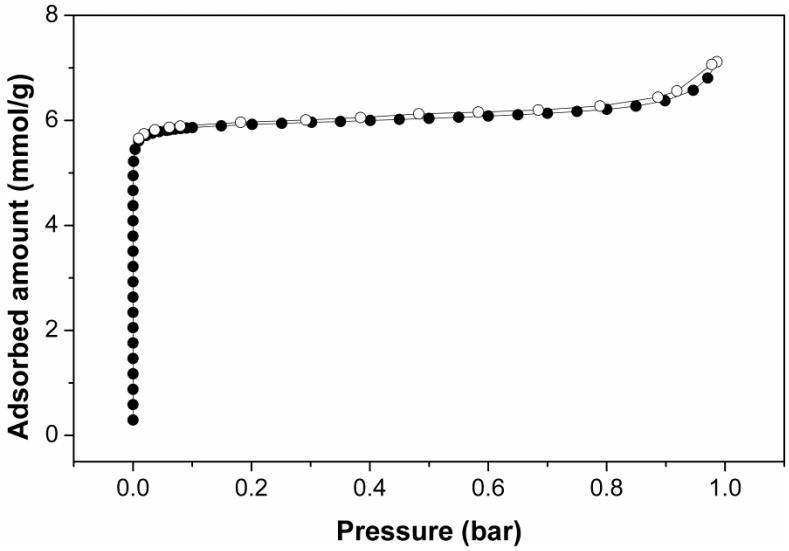

Figure 4. N_2 adsorption-desorption isotherm at 77 K.

Zeolite 5A has been recognized as the benchmark material for the separation of alkane isomers.[45] Zeolite 5A exhibits the LTA (Linde Type A) structure which possesses three-dimensional pore structure. The cavity is defined by the sodalite cage (truncated octahedra, Figure 3) with a diameter of 11.4 Å. The cages are interconnected by eight member oxygen ring as windows with a pore aperture of 4.2 Å. N_2 adsorption at 77 K on zeolite 5A gives a BET surface area of 516 m^2/g and a pore volume of 0.19 cm^3/g (Figure 4). Due to the confined pore aperture of zeolite 5A, it adsorbs exclusively linear alkanes, rendering it the capability of separating alkane isomers by selective molecular exclusion.

Adsorptive separation of alkanes can be done through two mechanisms: kinetically controlled and thermodynamically controlled. Kinetically controlled separation relies on the differences in diffusion rate.[7] Its extreme or ideal scenario is selective molecular exclusion, where a component in the mixture can be either adsorbed or completely excluded by the adsorbent. In contrast, in thermodynamically controlled separation, all components can diffuse into the pores without markedly restriction but they discriminated by the difference adsorption affinity with the adsorbent. Both approaches have their own advantages and limitations. Kinetically controlled separation can usually offer high selectivity while thermodynamically controlled separation can be applied to the separation of adsorbates that do not have evident difference in molecular size or shape.

The separation mechanism by zeolite 5A is desirable, as it can extract branched alkanes which have higher octane number. In addition, the pure n-hexane adsorbed by 5A can be used as chemical feedstock or put back to the isomerization unit. However, zeolite 5A has its own limitations. It adsorbs ~ 8 wt% of n-hexane at 150 °C and 105 torr which is relatively low. This is restricted by its relatively low porosity. Moreover, in order to further

improve the RON of gasoline, alkane isomers need to be separated as a function of branching. For example, dibranched C6 alkanes should be extracted from its linear and monobranched isomers. This, however, cannot be done by zeolite 5A since it excludes any branched alkanes. Thus there is a pressing need to explore novel sorbent materials that can adequately address the limitation of zeolite 5A for the separation of alkane isomers.

2.2 Materials design rationale: topology directed design of Zr-MOFs

MOFs have been investigated extensively for various applications since its emergence in late 1990s owing to its fascinating features that includes high porosity, tunable pore structure and functionality. However, compared to zeolites, MOFs generally bear relatively poor stability which has largely limited their real-world applications in industry.[46,47] Since the first report in 2008, the development of zirconium based MOFs (Zr-MOFs) has largely addressed the stability issue of MOFs.[48-50] Zr-MOFs are generally much more stable than late transition metals such as Zn and Cu which is contributed to two main reasons. First, the high valence metal Zr tend to form stronger bonds with oxygen, making them less sensitive to heating or attacking from water. In addition, Zr-MOFs are exclusively built on large secondary building units (SBUs, Figure 5) such as Zr6 clusters with high connectivity, making the framework robust.

We focus on a specific subfamily of MOFs, that is, Zr-MOFs built on tetratopic carboxylate linkers for the following reasons: 1) Similar to other Zr-MOFs, they show excellent thermal and water stability. 2) They show intriguing structure diversity and their structures are largely dependent on the geometry of the organic ligands. 3) A specific type of structure with ***ftw*** topology built on Zr and planar tetracarboxylates features high porosity with large cavities but small window size which is desirable for molecular separations.[51-54]

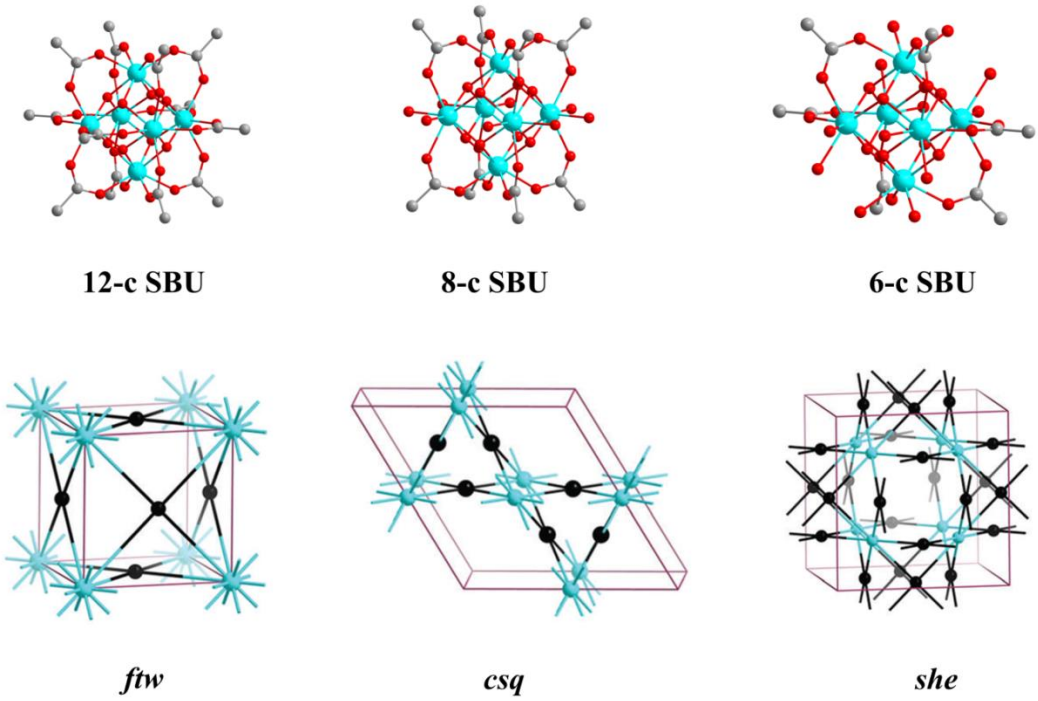

Figure 5. Zr6 SBUs with different connectivity and their representative topologies.

We first performed an overall topology analysis on the reported Zr-MOFs structures built on tetratopic ligands. We extracted from CSD database and recent literature all 41 distinct zirconium based MOFs constructed from Zr6 clusters and tetratopic linkers. Among them, 5 structures are built on tetrahedron shaped ligands whereas the other 36 are all constructed from planar linkers. The connectivity of the Zr6 clusters in these structures is 12, 8, or 6 and the underlying topology can be ***ftw***/***shp***, ***csq***/***sqc***/***scu***, or ***she***, respectively. The most common topology in this subfamily is 4, 12-connected ***ftw*** type structure which represents the most thermodynamically stable network and has the largest porosity and lowest propensity for framework catenation. A detailed analysis of the 17 ***ftw*** structures reveals that a ***ftw*** structure must use a ligand with unitary aspect ratio which was summarized in previous literatures does not hold any more.[54] The four least symmetric ***ftw*** structures have

rectangular ligands and the largest aspect ratio is 1.15. This indicates by proper synthesis ***ftw*** structures can be obtained with rectangular ligands.

We are interested in structures with ***ftw*** topology because of its fascinating structure features that are desirable for molecular separations. However, the reported ***ftw*** structures are exclusively built on large organic ligands (e.g. porphyrin or pyrene based molecules, Figure 14) which results in large pore apertures that are not suitable for such separation applications. The aperture size of a ***ftw*** structure depends on the distance between two adjacent Zr6 SBUs which is determined by the distance between adjacent carboxylate on the organic ligand. Thus in order to obtain ***ftw*** structure with smaller pore size, we design three isophthalate based planar tetratopic linkers and attempt to incorporate them into Zr-MOFs. These three ligands have similar shape but with different aspect ratios which will offer some sight into the relationship between the ligand geometry and the resulting MOF structures.

2.3 Material synthesis and structure characterizations

2.3.1 Ligand synthesis

Synthesis of H_4bptc

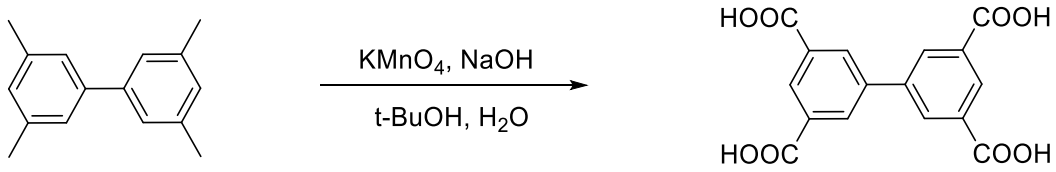

The synthesis of H_4bptc was carried out according to reported procedure with slight modifications[55]. 3,3'5,5'-tetramethylbiphenyl (5.0 g, 0.023 mol), NaOH (2.0 g, 0.05 mol) were mixed in t-BuOH/H_2O (100/100 mL) with stirring at 50 °C. $KMnO_4$ (43.0 g, 0.27 mol) was added in portions over one week. The temperature was subsequently increased

to 70 °C and kept for 2 days. The mixture was filter when hot and the clear filtrate was added into 100 mL 6M HCl. White solid was obtained upon filtration. The crude product was recrystallized from DMF (~100 mL) to give pure H_4bptc with a yield 82%.

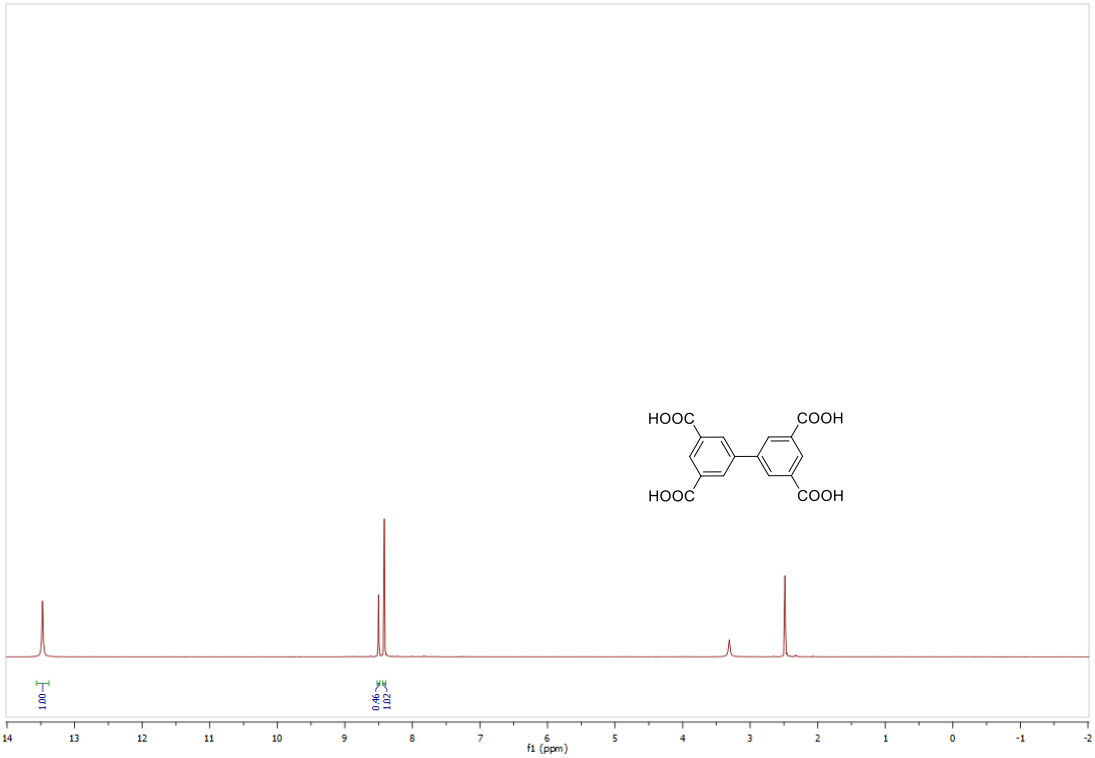

Figure 6. ^{1}HNMR of H_4bptc.

Synthesis of H_4abtc

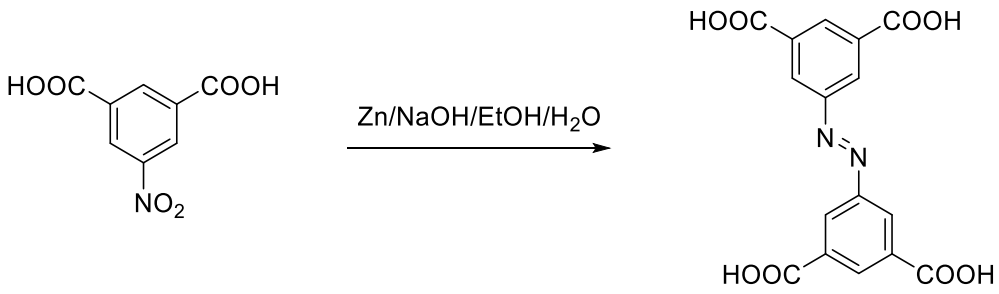

H_4abtc was synthesized according to reported procedure with slight modifications[56]. 5-nitroisophthalic acid (2.1 g, 0.01 mol), NaOH (0.8 g, 0.02 mol), Zinc powder (1.3 g, 0.02 mol) were mixed in ethanol/H_2O (50/20 mL). The mixture was kept under refluxing for 12

hours before cooled to room temperature. Yellow solid was obtained through vacuum filtration which was then dissolved in 80 mL 1M NaOH solution. Upon filtration, the filtrate was acidified with 6 M HCl to get orange solid. The crude product was recrystallized from DMF to give pure H_4abtc as orange solid (1.3 g, yield: 73%).

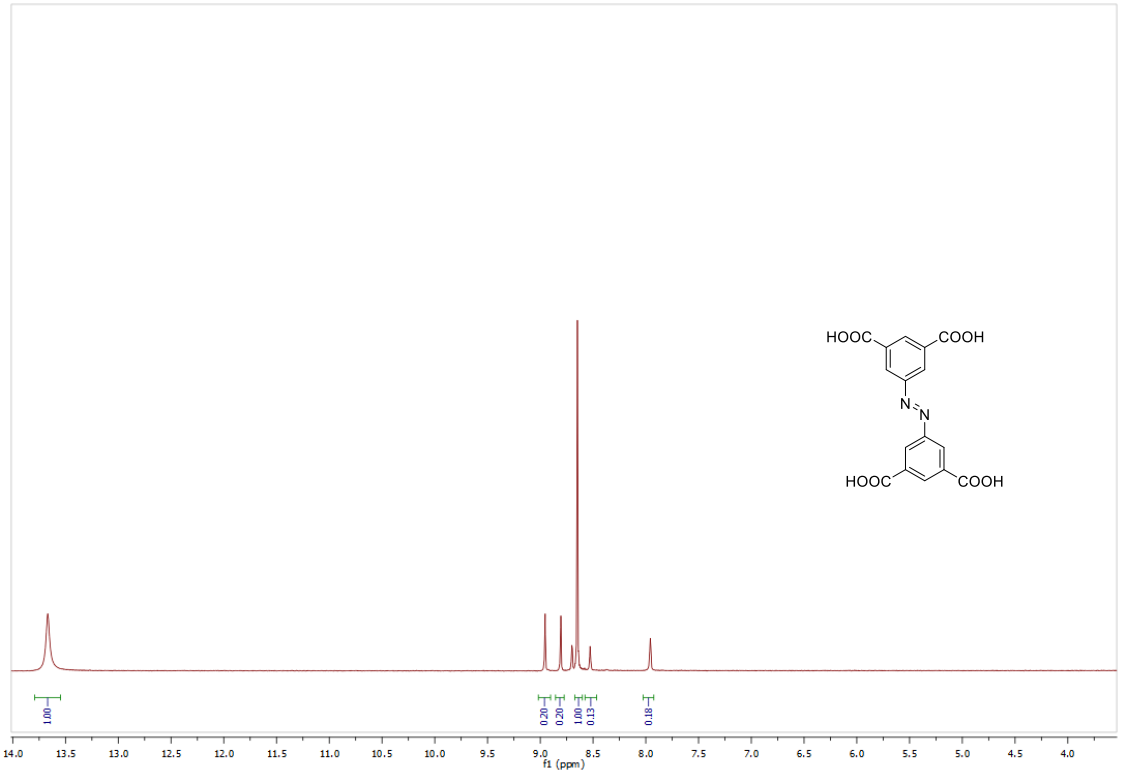

Figure 7. ^{1}H NMR spectrum of H_4abtc.

Synthesis of H_4tptc-$(Me)_2$

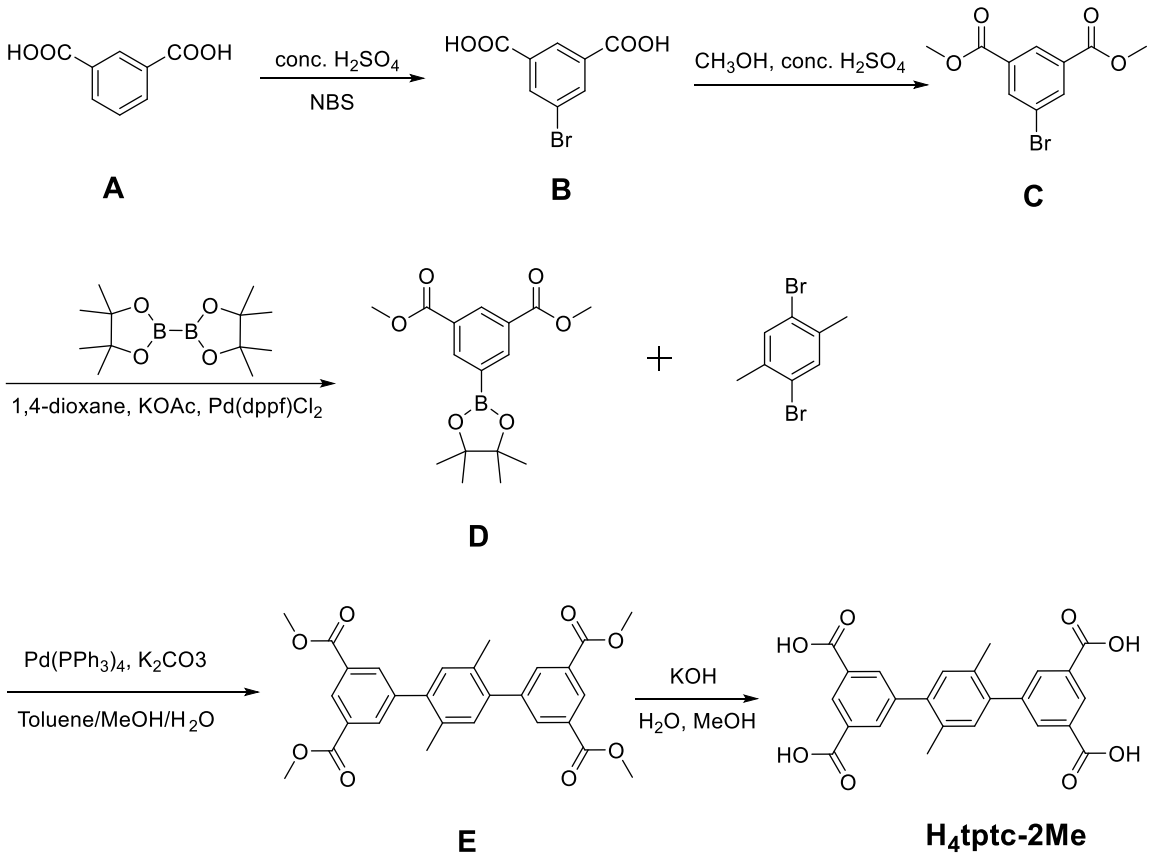

A to **B**: **A** (14.0 g, 0.084 mol) was dissolved in 40 mL conc. H_2SO_4 at 60 °C under stirring. N-Bromosuccinimide (NBS, 16 g, 0.090 mol) was added to the reaction in portions over 1 hour and the mixture was stirred at 60 °C for an additional hour. After the reaction was completed, the mixture was poured into 200 g crushed ice and stirred at room temperature for 1 hour. Light yellow solid was obtained by filtration and washed with DI water (100 mL). The crude product was recrystallized from ethyl acetate to give pure **B** (12 g, 59 % yield).

B to **C**: **B** (8 g, 0.033 mol) was dissolved in 120 mL methanol under stirring and 6 mL conc. H_2SO_4 was subsequently added to the mixture. The reaction was heated to reflux for 24 hours. After cooling down to room temperature the solvent was removed through rotovap. The obtained solid was dispersed in 40 mL DI water and the aqueous phase was

extracted by dichloromethane (40 mL × 3). The combined organic layer was washed with saturated $NaHCO_3$ and brine and dried over $MgSO_4$. Crude product was obtained upon removal of the solvent which was recrystallized from methanol to give pure **C** (8.3 g, 91 % yield).

C to **D**: **C** (3.3 g, 0.012 mol), bis(pinacolato)diboron (3.4 g, 0.013 mol), dried potassium acetate (3.6 g), [1,1'-Bis(diphenylphosphino)ferrocene]palladium(II) dichloride ($Pd(dppf)Cl_2$, 0.2 g, 0.27 mol) were mixed in a 250 mL flask and evacuated for 1 hour before 100 mL dried, degassed 1,4-dioxane was added. The reaction was stirred at 80 °C under nitrogen atmosphere for 24 hours. After the reaction was completed, organic solvent was removed by rotovap and the remained solid was extracted with dichloromethane. The crude product was purified through a silica plug with a eluent of petroleum ether: ethyl acetate= 8: 1 to give pure **D** as a white solid (3.5 g, 90 % yield).

D to **E**: **D** (2.0 g, 6.3 mmol), 2,5-dibromo-p-xylene (0.6 g, 2.3 mmol), tetrakis(triphenylphosphine) palladium(0) (150 mg, 0.15 mmol) and potassium carbonate (760 mg, 5.5 mmol) were mixed in a 100 mL flask and evacuated for 1 hour before 40 mL degassed toluene-methanol-water (v:v:v= 20:10:10) mixed solvent was added. The reaction was heated to reflux for 3 days. The reaction was cooled to room temperature when it was completed and organic solvent was removed by rotary evaporation. 50 mL DI water was added to the residue which was extracted by dichloromethane for 3 times with 50 mL each time. The organic phase was combined and washed with water and brine and dried over anhydrous $MgSO_4$. After removal of organic solvent, the crude product was washed with a mixed solvent of acetone/dichloromethane (v/v = 9/1) several times (10 mL × 5) to give pure compound **E** (0.68 g, 60% yield).

E to **H_4tptc-2Me**: **E** (0.5 g, 1 mmol) was dissolved in a mixture of 30 mL THF and 30 mL 3M KOH aqueous solution. The mixture was heated to reflux for 12 hours. After removal of THF, the remaining clear solution was added dropwise to excess 6M HCl solution. The white precipitate was collected by centrifuge and washed with DI water until it is neutral. The resultant solid was dried at 80 °C under vacuum to give pure H_4-tptc-2Me (0.4 g, 92% yield).

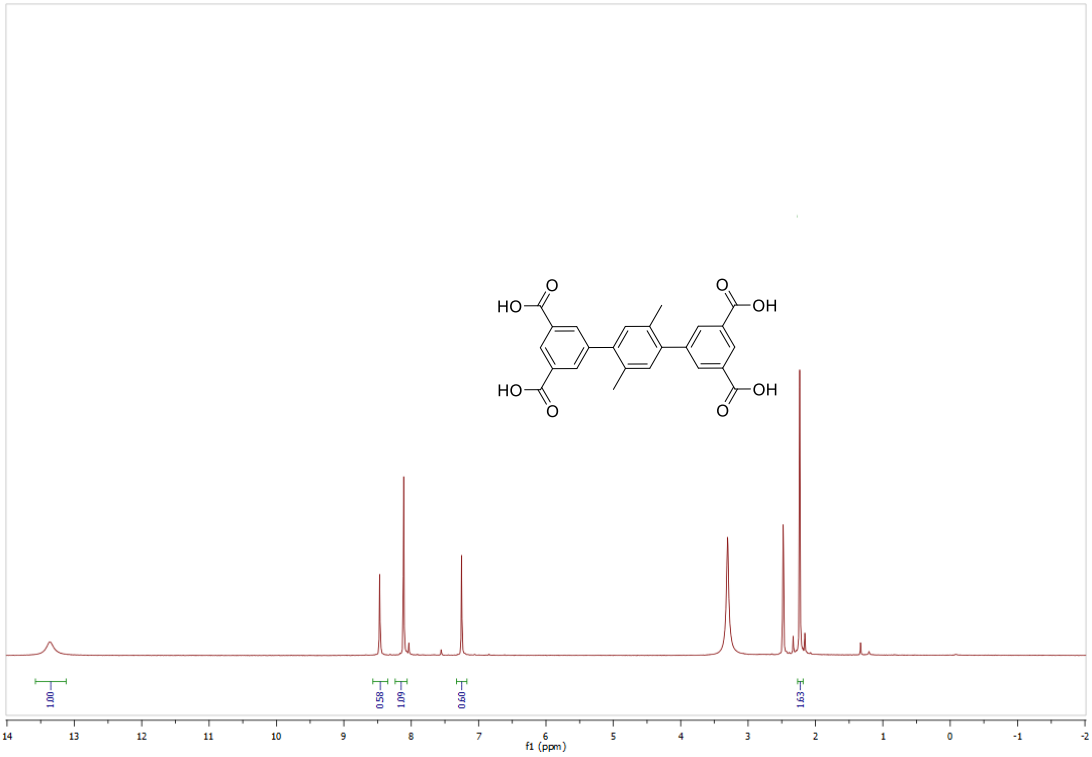

Figure 8. ^{1}H NMR spectrum of H_4bptc-2Me.

2.3.2 MOF synthesis

Synthesis of Compound 1: Zirconium (IV) oxychloride octahydrate ($ZrOCl_2 \cdot 8H_2O$, 32.2 mg, 0.1 mmol) was ultrasonically dissolved in a mixed solvent of N,N-dimethylformamide

(DMF, 5 mL) and formic acid (5 mL) in a 20 mL scintillation vial. H_4bptc (33 mg, 0.1 mmol) was then added to the solution which was sonicated for 5 min before being moved to a preheated oven at 120 °C. The reaction was kept at 120 °C for 3 days and microcrystalline white powder was obtained through centrifuge. The materials were washed with DMF and methanol with a Soxhlet extractor for 2 and 3 days, respectively prior to adsorption study.

Synthesis of Compound **2**: Zirconium (IV) oxychloride octahydrate ($ZrOCl_2 \cdot 8H_2O$, 32.2 mg, 0.1 mmol) was ultrasonically dissolved in a mixed solvent of N,N-dimethylformamide (DMF, 8 mL) and formic acid (6 mL) in a 20 mL scintillation vial. H_4abtc (35.8 mg, 0.1 mmol) was then added to the solution which was sonicated for 5 min before being moved to a preheated oven at 120 °C. The reaction was kept at 120 °C for 3 days and light orange crystals were obtained through centrifuge. The materials were washed with DMF and methanol with a Soxhlet extractor for 2 and 3 days, respectively prior to adsorption study.

Synthesis of Compound **3**: Zirconium (IV) oxychloride octahydrate ($ZrOCl_2 \cdot 8H_2O$, 32.2 mg, 0.1 mmol) was ultrasonically dissolved in a mixed solvent of N,N-dimethylformamide (DMF, 8 mL) and formic acid (4.5 mL) in a 20 mL scintillation vial. H_4tptc-2Me (21.7 mg, 0.05 mmol) was then added to the solution which was sonicated for 5 min before being moved to a preheated oven at 120 °C. The reaction was kept at 120 °C for 3 days and colorless crystals were obtained through centrifuge.

2.3.3 Crystal structures

Crystal structure of compound **1.** Crystal structure of compound 1 was determined by powder refinement since tremendous effort on growing large single crystals didn't succeed. It was revealed that the compound **1** crystalizes in a cubic space group Im-3 (a = 24.3597 (3) Å), through the Rietveld refinement against the Powder X-ray diffraction pattern. The position of Zr-Cluster was firstly solved by direct method (EXPO) using the Powder X-ray diffraction pattern. Then, the location of organic linker was determined using simulated annealing method by TOPAS in the space group of I23. An initial model was successfully built up and the symmetry was further increased into Im-3 later. At last, Rietveld refinement was made based on the model obtained above, to achieve the final structure model of this Zr-MOF material.

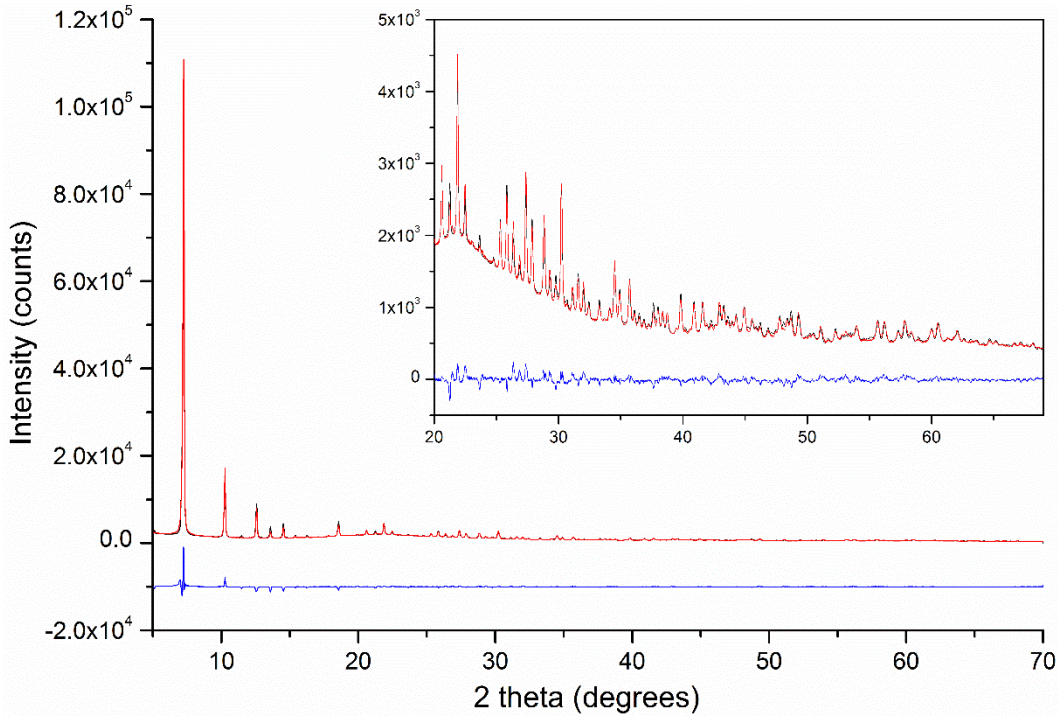

Figure 9. observed (black), calculated (red) and difference (blue) PXRD profiles for the Rietveld refinement of the activated Zr-MOF.

Table 2. Crystal data and structure refinement of compound **1**.

Formula	$Zr_6O_4(OH)_4(bptc)_3$
Wavelength	1.5406 Å Cu-Kα_1
Crystal system	Cubic
Space group	*Im*-3
Unit cell dimensions	24.3597 (3) Å
Volume	14455.0 (5) $Å^3$
Z	8
2Theta range for data refinement	$5° < 2\theta < 70°$
Number of parameters	30
Number of data points	5000
Number of restrains	6 for Zr-O, 10 for O-Zr-O, 4 for C-O, 2 for C-C
Refinement method	Rietveld refinement
$R_p/R_{wp}/R_{exp}$	0.0377/0.0567/0.0273
R_B	0.0381

Compound **1** is built on 12-connected $Zr_6(\mu_3\text{-}O)_4(\mu_3\text{-}OH)_4(COO)_{12}$ SBUs which are linked through 4-connected $bptc^{4-}$ ligands to form a 3D framework. The SBU is composed of six Zr atoms assembled into an octahedron where the eight facets are occupied by $\mu_3\text{-}O^{2-}$ or $\mu_3\text{-}OH^-$ anions. Each Zr atom is coordinated to eight O atoms, four of which belong to four different $bptc^{4-}$ ligands and the remaining four are from $\mu_3\text{-}O^{2-}/OH^-$ groups. Each $bptc^{4-}$ linker is connected to four different SBUs with each carboxylate coordinated by two adjacent Zr atoms in the same SBU in a bi-monodentate fashion. Similar to other reported

Zr-MOFs with **ftw** topology, compound **1** contains cubic cage-like pores with Zr_6 clusters on the vertices and planar $bptc^{4-}$ linkers on the faces. The cages have a dimension of ~12 Å and are interconnected through smaller tetrahedral cages located at the twelve edges of the cubic cages. These tetrahedral cages have a window size of ~ 4.5 Å. It is noteworthy that $bptc^{4-}$ is the smallest member of all tetratopic linkers that lead to **ftw** type of Zr-MOFs. Compound **1** also represents the first Zr-MOF built on isophthalate based ligands. While isophthalate-based organic linkers have been widely used in constructing MOFs with various metals, no zirconium MOFs based on such ligands have been reported before the current work.[57] This is likely because of the short distance between the two carboxylates on the same isophthalate moiety which gives rise to an added difficulty in forming extended structures with large Zr_6 SBUs.

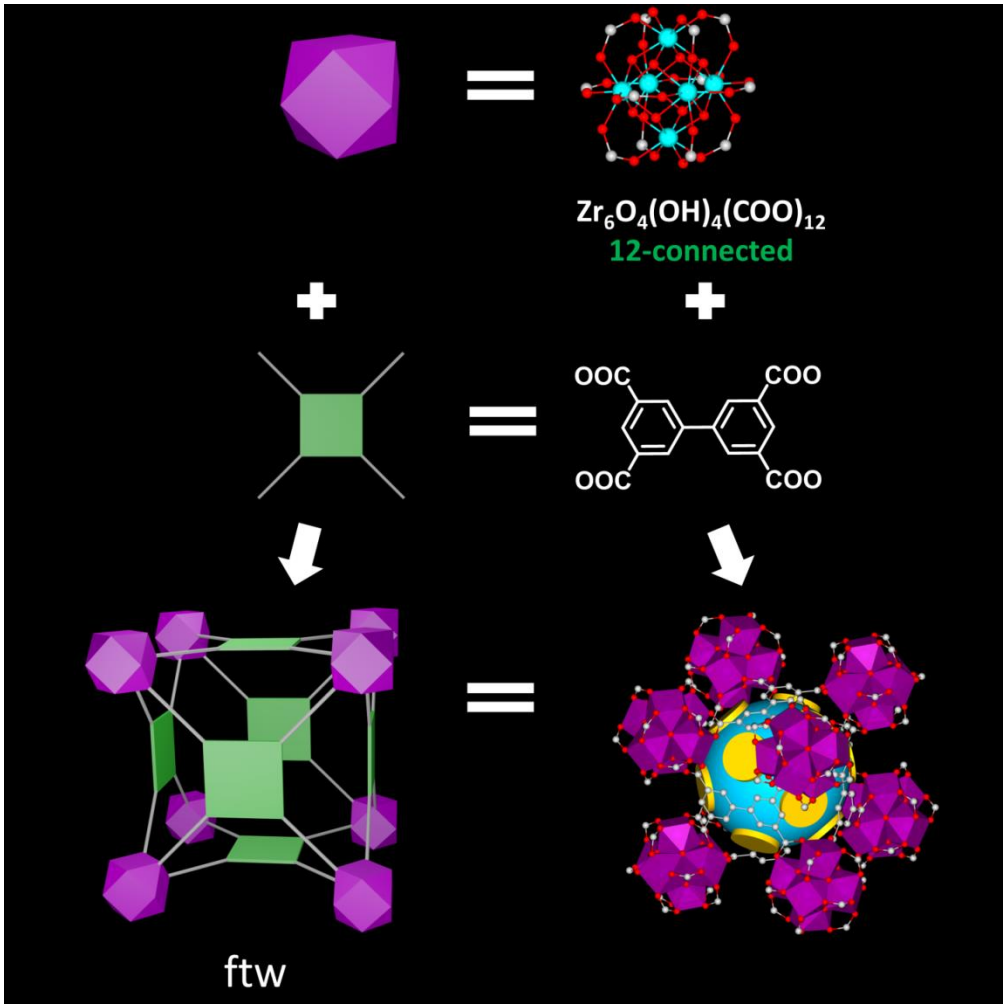

Figure 10. Crystal structure and topology of compound **1**.

Crystal structure of compound **2.** Single crystal X-ray diffraction reveals compound **2** crystallizes in monoclinic crystal system with space group *C2/m* which is different from compound **1**. This indicates by replacing $bptc^{4-}$ with $abtc^{4-}$ didn't give rise to an isoreticular expanded structure. The structure consists of 8-connected $Zr_6(\mu_3\text{-}O)_4(\mu_3\text{-}OH)_4(HCOO)_8$ SBUs that are propagated by 4-connected $abtc^{4-}$ linkers along three dimensions, forming a framework with 4,8-c **scu** topology. The connectivity of the SBU is reduced to 8 from 12 in compound **1** as a result of four carboxylate groups being replaced by terminal H_2O/OH^- groups. In addition to the coordination to four O atoms from capped $\mu_3\text{-}O^{2-}/OH^-$, each Zr

atom at the equatorial position also coordinates to two carboxylate O atoms from two different $abtc^{4-}$ ligands, and another two O atoms from terminal H_2O/OH^- groups. The four remaining coordination sites of each of the two Zr atoms at the apical position are all taken by carboxylate O atoms from four different $abtc^{4-}$ ligands. The rectangular ligand $abtc^{4-}$ is present in both *trans* and *gauche* conformation. Comparing to the overall connectivity of compound **1**, the $abtc^{4-}$ ligands along the crystallographic *a*-axis are missing in compound **2**, leading to the transformation from cage-like pore to 1D channel with a diameter of ~ 7 Å. The preference of **scu** topology over **ftw** for compound **2** is due to the increase in aspect ratio (from 1.45 for bptc to 1.78 for abtc) which results from a change of a nearly square shaped tetratopic ligand to a rectangle shaped ligand.

Table 3. Crystal data and structure refinement for compound **2**.

Empirical formula	C32 H20 N4 O32 Zr6	
Formula weight	1519.84	
Temperature	100(2) K	
Wavelength	0.7749 Å	
Crystal system	Monoclinic	
Space group	C2/m	
Unit cell dimensions	a = 25.4692(11) Å	a= 90°.
	b = 36.3589(15) Å	b= 122.260(2)°.
	c = 21.5275(9) Å	g = 90°.
Volume	16857.8(13) $Å^3$	
Z	8	

Density (calculated)	1.198 Mg/m^3
Absorption coefficient	0.965 mm^{-1}
F(000)	5888
Crystal size	0.130 x 0.020 x 0.020 mm^3
Theta range for data collection	2.397 to 27.868°.
Index ranges	-30<=h<=25, 0<=k<=43, 0<=l<=25
Reflections collected	94479
Independent reflections	22502 [R(int) = 0.1156]
Completeness to theta = 27.706°	98.6 %
Absorption correction	Semi-empirical from equivalents
Max. and min. transmission	0.981 and 0.612
Refinement method	Full-matrix least-squares on F^2
Data / restraints / parameters	22502 / 468 / 678
Goodness-of-fit on F^2	1.052
Final R indices [I>2sigma(I)]	R1 = 0.0877, wR2 = 0.2360
R indices (all data)	R1 = 0.1342, wR2 = 0.2802
Extinction coefficient	n/a
Largest diff. peak and hole	3.035 and -1.726 $e.Å^{-3}$

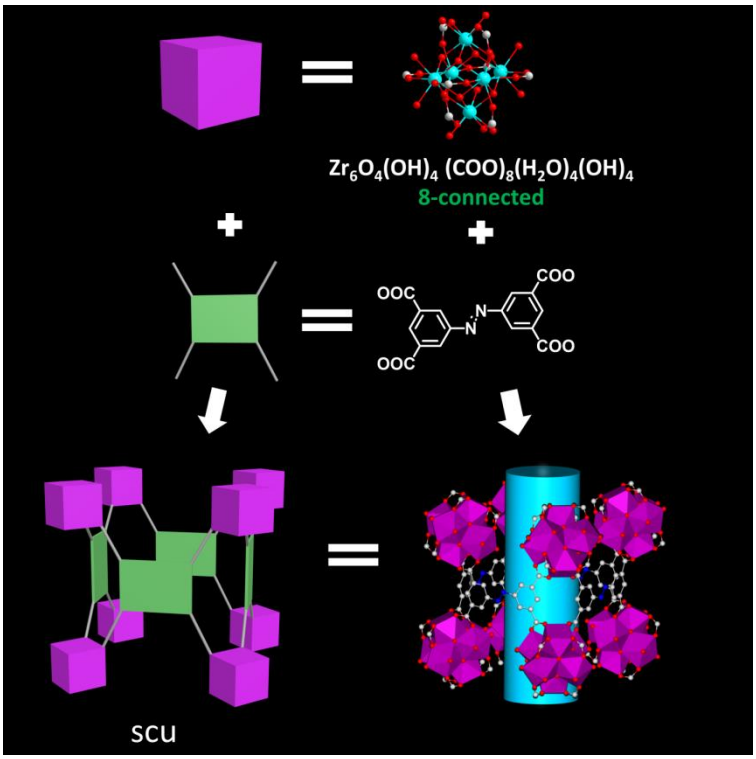

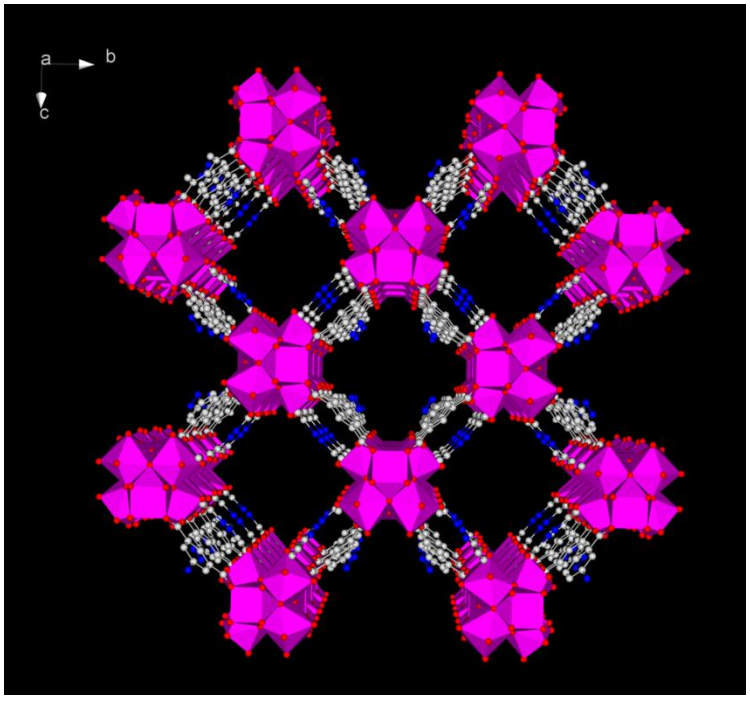

Figure 11. Crystal structure and topology of compound **2**.

Crystal structure of compound **3**. Further increase in the aspect ratio of the organic ligand tptc-$(Me)_2$ (2.28, where two isophthalate groups are separated apart by a phenyl ring) led to a totally different connectivity in compound **3**. Single crystal X-ray diffraction analysis shows that compound **3** crystallizes in orthorhombic crystal system (space group *Imma*). In this structure, the formula of the SBU changes to $Zr_6(\mu_3\text{-}O)_4(\mu_3\text{-}OH)_4(COO)_4$, where the Zr_6 octahedral core remains but its connectivity further reduces to 4 as a result of replacing four carboxylates in compound **2** by four terminal formate groups. Each of the four equatorial Zr atoms coordinates to eight O atoms where four are from bridging $\mu_3\text{-}O^{2-}/OH^-$, two from terminal H_2O/OH^-, one from terminal formate and one from a carboxylate of a tptc-$(Me)_2^{4-}$ linker. The two apical Zr atoms coordinate to four bridging $\mu_3\text{-}O^{2-}/OH^-$, two formate and two carboxylates from two distinct tptc-$(Me)_2^{4-}$. The terminal formate groups adopt a bi-monodentate coordination mode, similar to carboxylates from tptc-$(Me)_2^{4-}$ linkers. The connection mode of the four-connected SBU in compound **3** resembles that of the paddle-wheel dinuclear $M_2(HCOO)_4$ (M = Zn, Cu, etc) SBU commonly observed for M^{2+} (e.g. Cu^{2+} and Zn^{2+}) based MOFs.[58] The resulting 3D structure adopts a rarely reported 4-c **lvt** topology.[59]

Table 4. Crystal data and structure refinement for compound **3**.

Empirical formula	C7 H8.50 N0 O8 Zr1.50
Formula weight	357.47
Temperature	100(2) K
Wavelength	0.7749 Å
Crystal system	Orthorhombic
Space group	Imma

Unit cell dimensions	a = 25.2379(14) Å	a= 90°.
	b = 27.7529(16) Å	b= 90°.
	c = 15.2344(10) Å	g = 90°.
Volume	10670.6(11) $Å^3$	
Z	16	
Density (calculated)	0.890 Mg/m^3	
Absorption coefficient	0.757 mm^{-1}	
F(000)	2792	
Crystal size	0.200 x 0.070 x 0.040 mm^3	
Theta range for data collection	2.337 to 22.990°.	
Index ranges	-25<=h<=25, -27<=k<=27, -15<=l<=15	
Reflections collected	22021	
Independent reflections	2981 [R(int) = 0.0642]	
Completeness to theta = 22.990°	98.3 %	
Refinement method	Full-matrix least-squares on F^2	
Data / restraints / parameters	2981 / 128 / 172	
Goodness-of-fit on F^2	3.092	
Final R indices [I>2sigma(I)]	R1 = 0.1483, wR2 = 0.3885	
R indices (all data)	R1 = 0.1908, wR2 = 0.4372	
Extinction coefficient	n/a	
Largest diff. peak and hole	4.446 and -1.252 e.$Å^{-3}$	

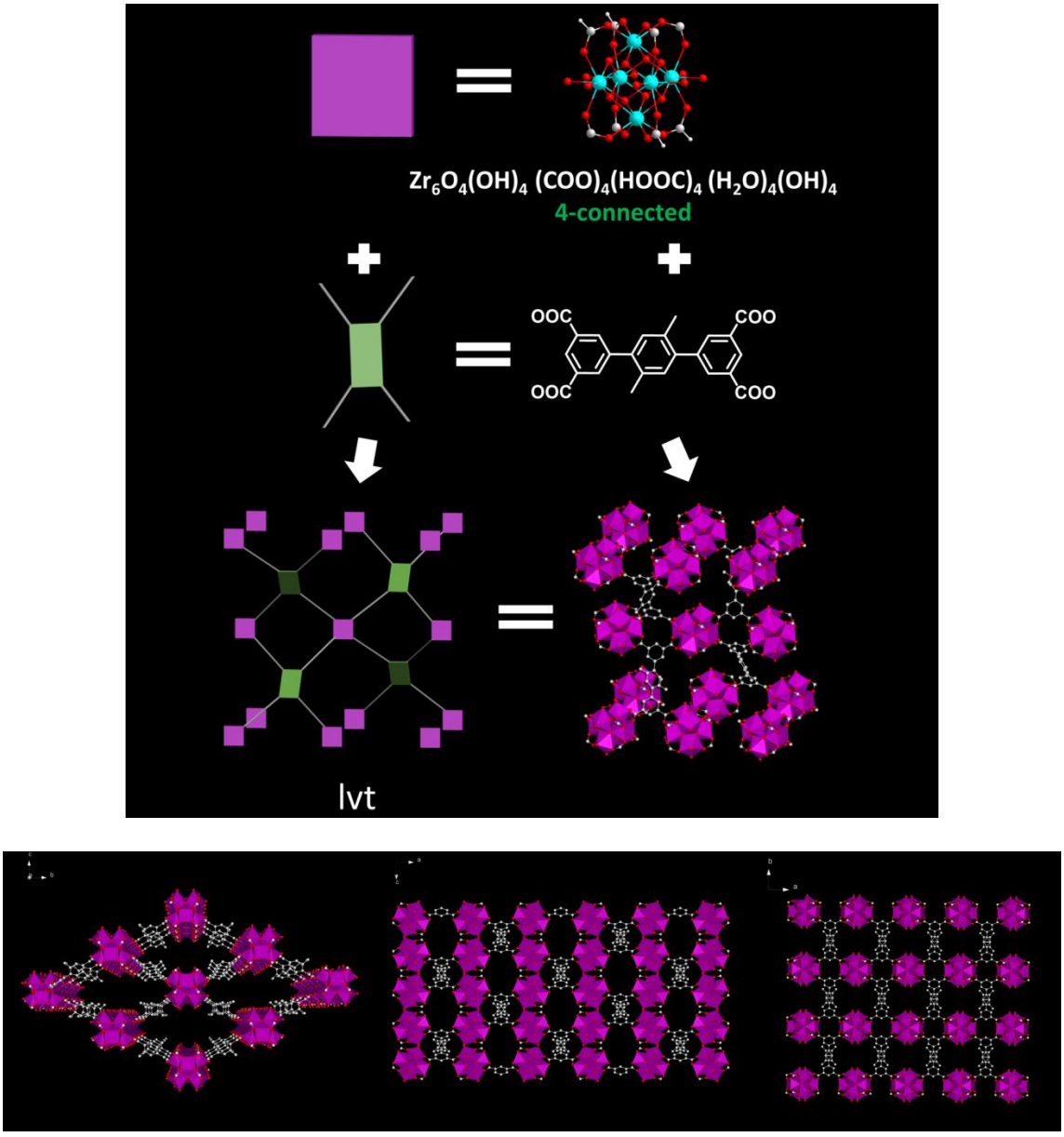

Figure 12. Crystal structure and topology of compound **3**.

2.4 Topology analysis of Zr-MOFs

Starting from the structures we obtained in this work, we have carried out a detailed analysis on reported structures built on Zr6 cluster so far using ToposPro approach. It should be noted that the each underlying net for giving connectivity of the ligand and

cluster has the minimal possible transitivity. Thus, 4,12-c **ftw**/**shp**, 4,8-c **csq**/**sqc**/**scu**, 4,6-c **she** contain two distinct nodes and only one type of edge (transitivity 21) and 4-c **lvt** is unimodal edge-transitive net (transitivity 11). More relations become apparent with net-subnet approach. The less coordinated nets 4,8-c **scu**, 4,6-c **she**, and 4-c **lvt** can be obtained from **ftw** net with highest coordination 4,12-c by removing 4-c nodes and hence reducing the ligand/cluster ratio. The relations together with minimal transitivity principle give the ground for speculations to predict yet unrealized but probable topological types of new Zr-MOFs (Figure 13), which are subnets of ftw net with minimal transitivity: 4,6-c **soc** (transitivity 21), 4,6-c **stp** (transitivity 21), and 4-c **sql** (transitivity 11).

Table 5. Topology summary of reported MOFs on polytopic ligands (transitivity given in red in square brackets, number of reported structures given in parentheses)

	Polytopic ligand (56)				
CN of Zr_6O_8	4 (rectangular, square)	4 (tetrahedral)	3	2 and 3	3 and 4
12	[21] **ftw** (18 + *this work*) [21] **shp** (TUTWUC)	**ith** [21] (BOHWOM)	**llj** [22] (OWILAJ)		
10					3,4,10-new OQIKUW
8	all[21] **csq** (6), **sqc** (3), **scu** (QAGBUY, *this work*)	**flu** [21] (4)	**the** [21] (3)	**tfz-d** [22] (OQIKOQ)	
6	**she** [21] (7)		**spn** [21] (3) 2D [21] **kgd** (3)		
4 square	**lvt** [11] *(this work)*				

Table 6. Topology summary of reported MOFs on ditopic ligands (transitivity given in red in square brackets, number of reported structures given in parentheses)

CN of Zr_6O_8	Ditopic ligand (145)
12	**fcu** [11] (95 single + 7 2fold), **bcu-x**-12-P42/mmc [13] (4)
11	**ela** [13] (3)
10	**bct** [12] (11), **fcu**-10-P42/mmc [12] (2)
8	**bcu** [11] (14), **reo** [11] (4 bent ligand), **hex** [12](1), **bon** [24] (1)
4	2D **sql** [11] (7)

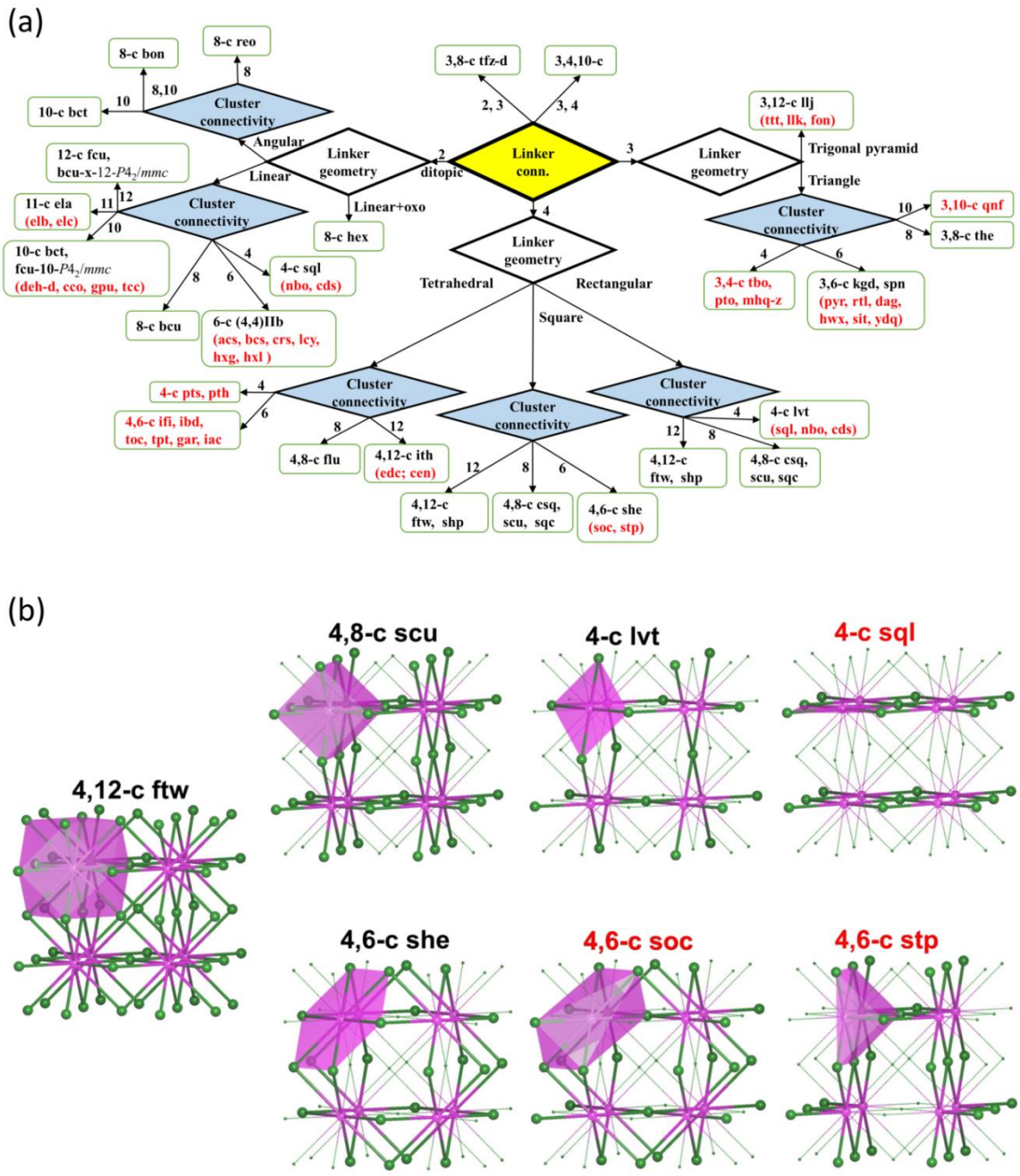

Figure 13. Topology analysis on Zr-MOFs. (a) Topologies of Zr-MOFs built on Zr_6 clusters with ditopic (145) and polytopic (56) linkers. In red are the minimum transitivity ones not yet observed. (b) **ftw** net and its subnets with minimum transitivity (magenta and green balls represent the nodes of Zr6 clusters and linkers, respectively). In red are those not yet realized.

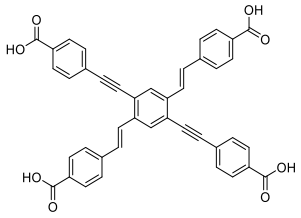

H_4XF

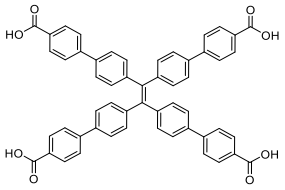

H_4ETTC

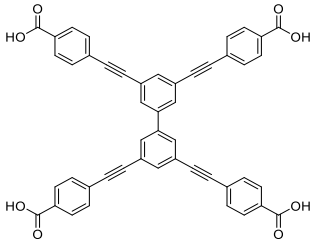

H_4BTBA

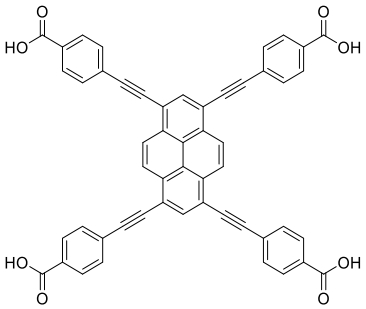

H_4PTBA

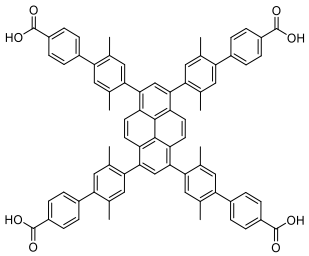

$H_4Py\text{-}XP$

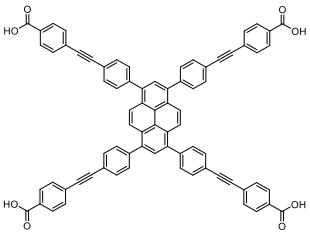

$H_4Py\text{-}PTP$

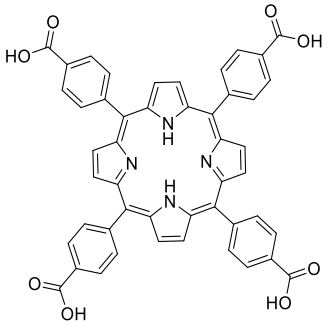

H_4TCPP

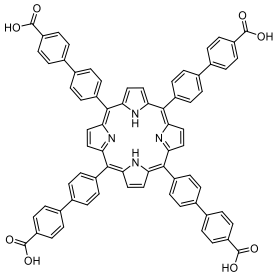

$H_4Por\text{-}PP$

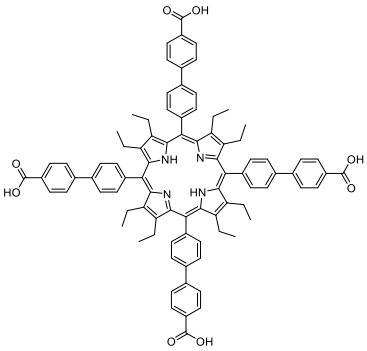

$H_4TCP\text{-}1$

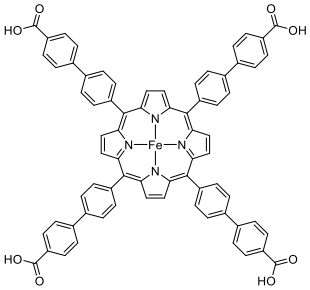

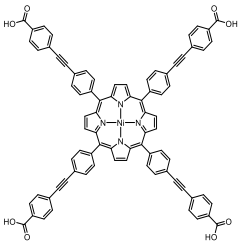

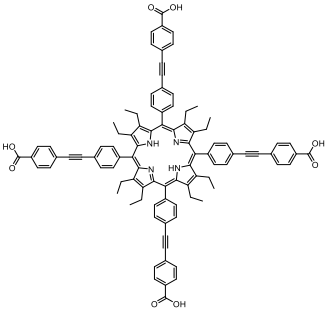

H_4Por-PP-Fe H_4Por-PTP H_4TCP-2

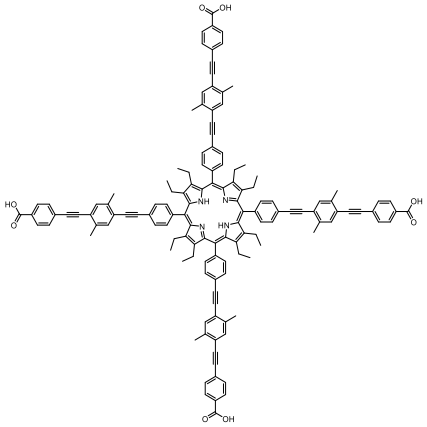

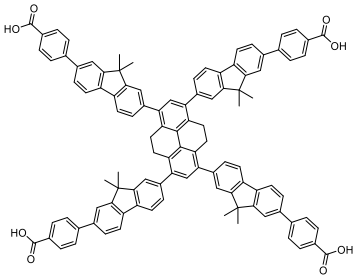

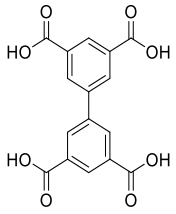

H_4TCP-3 H_4Py-FP H_4bptc

Figure 14. Organic linkers used to construct ftw Zr-MOFs.

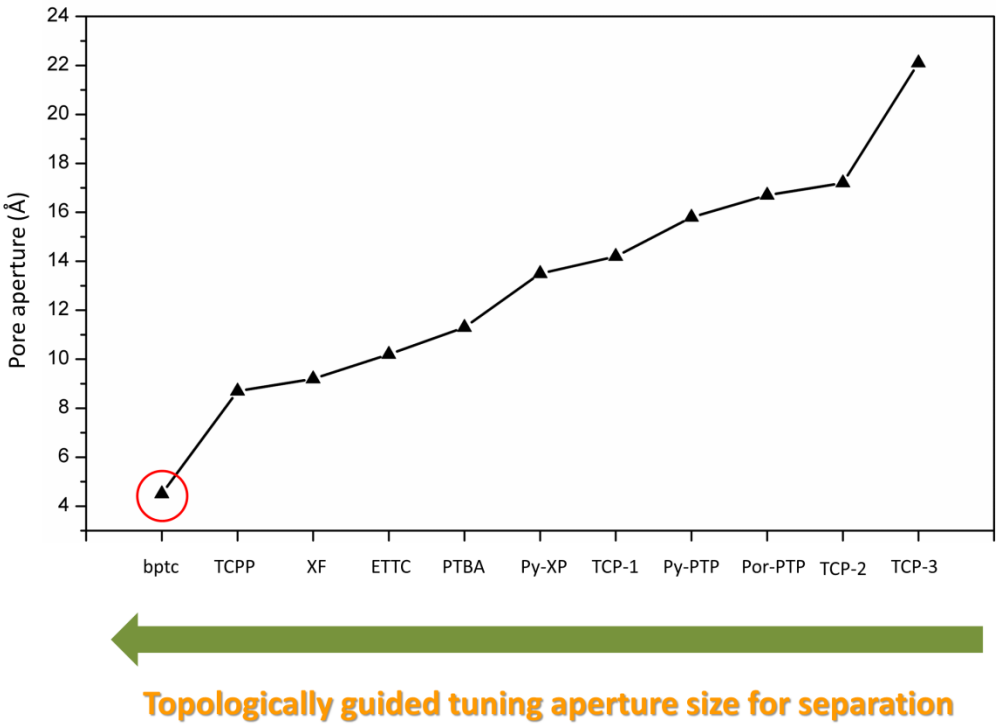

Figure 15. Pore aperture of ftw Zr-MOFs built on different linkers.

2.5 Porosity and stability

Permanent porosity of all three compounds have been confirmed and characterized by nitrogen adsorption measurements at 77 K. Their porosity results are shown in Figure 16-18 and Table 7. The BET surface area and pore volumes of compound **1** and **2** are significantly higher than that of zeolite 5A.

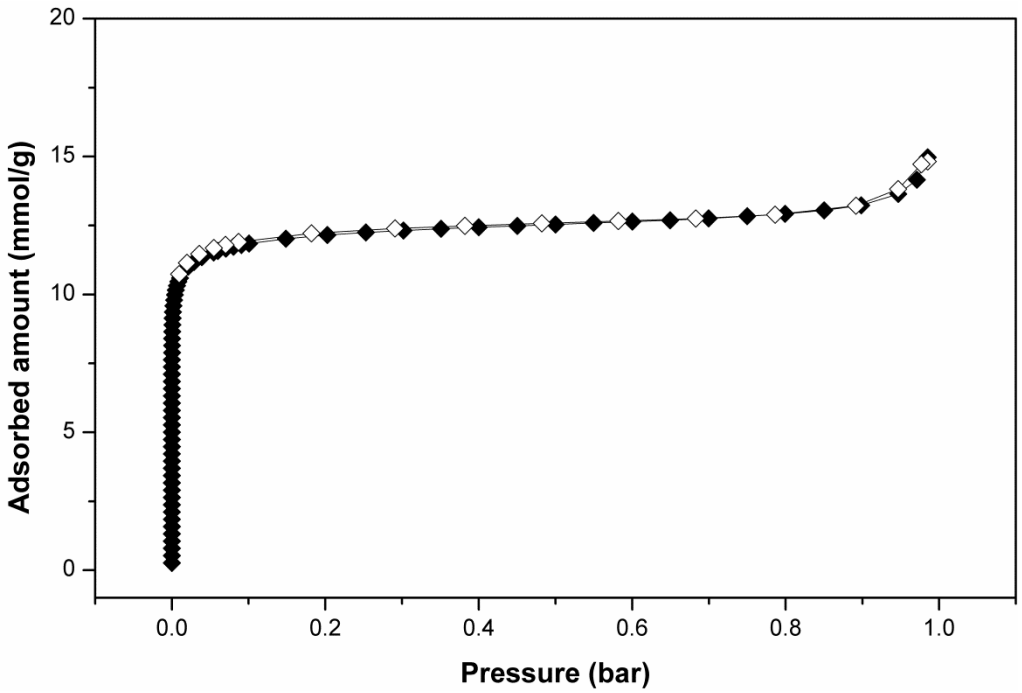

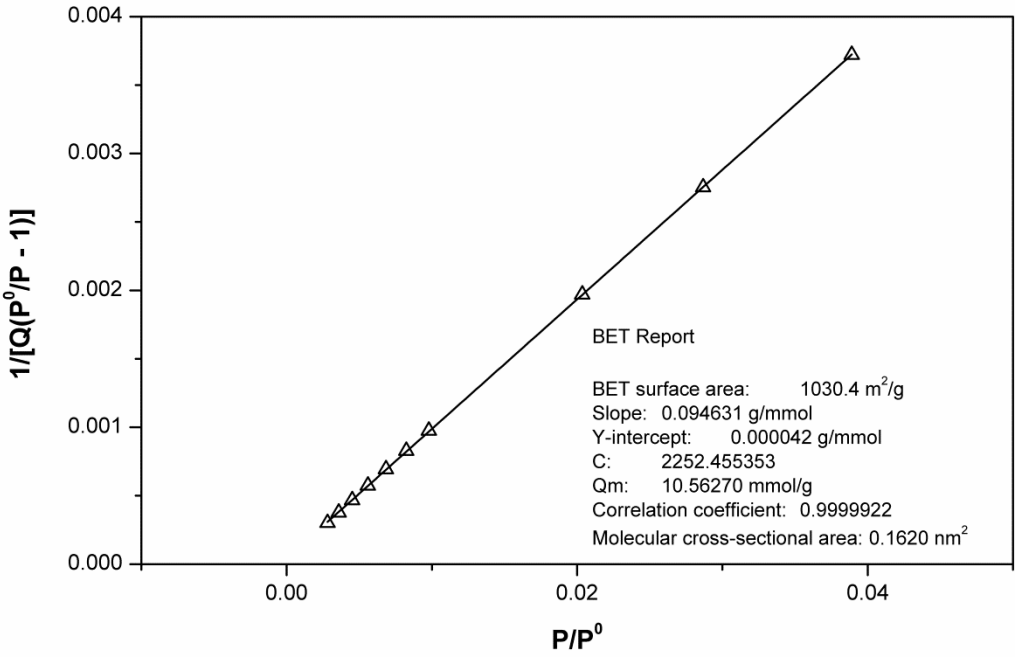

Figure 16. N2 adsorption isotherm at 77 K and BET plot for compound **1.**

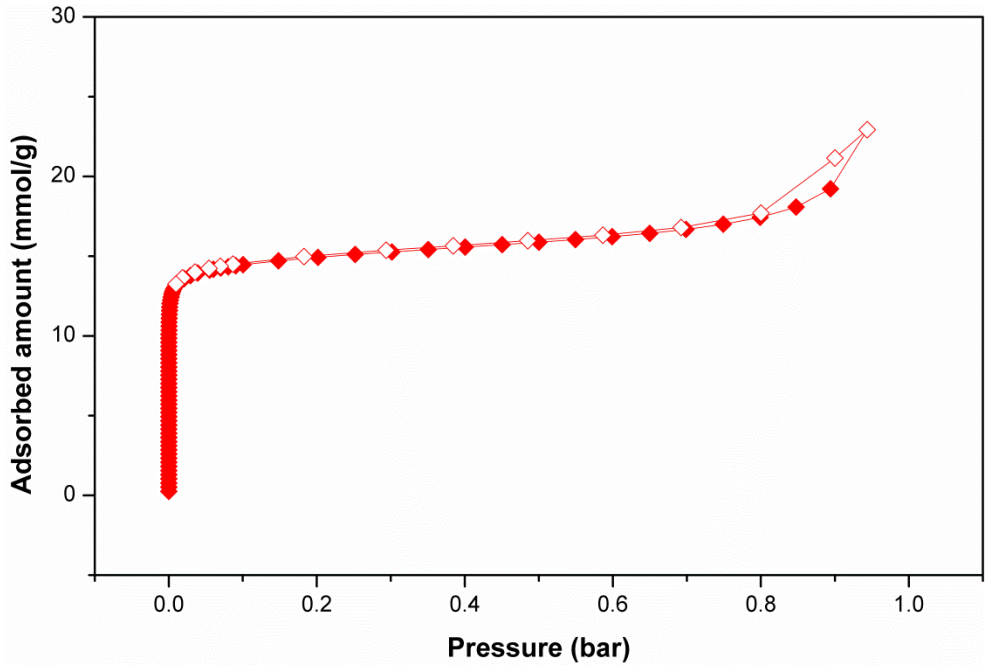

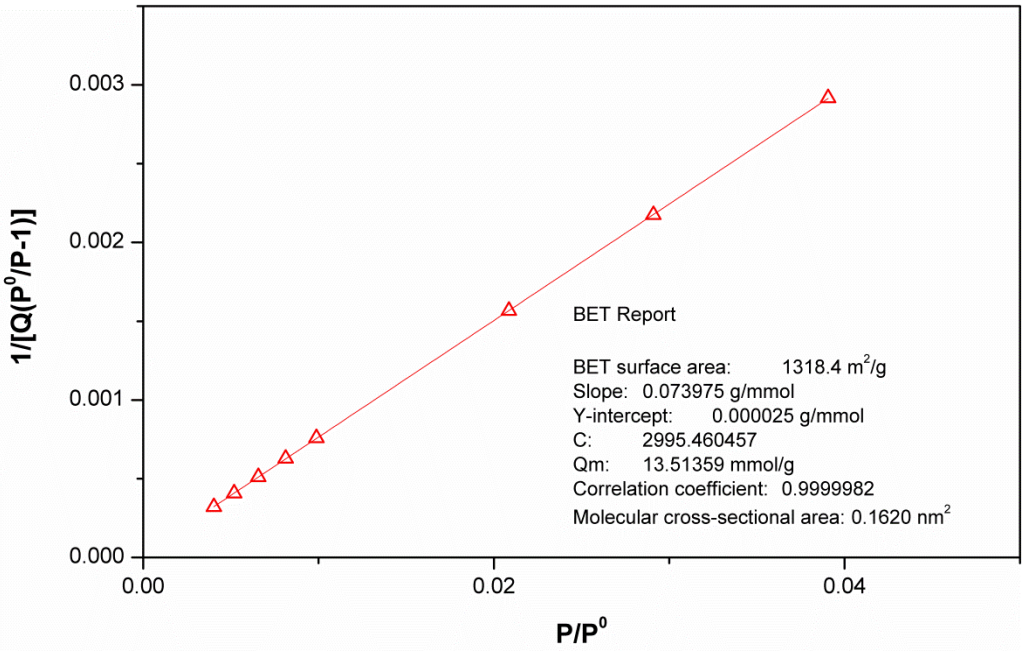

Figure 17. N_2 adsorption isotherm at 77 K and BET plot for compound **2.**

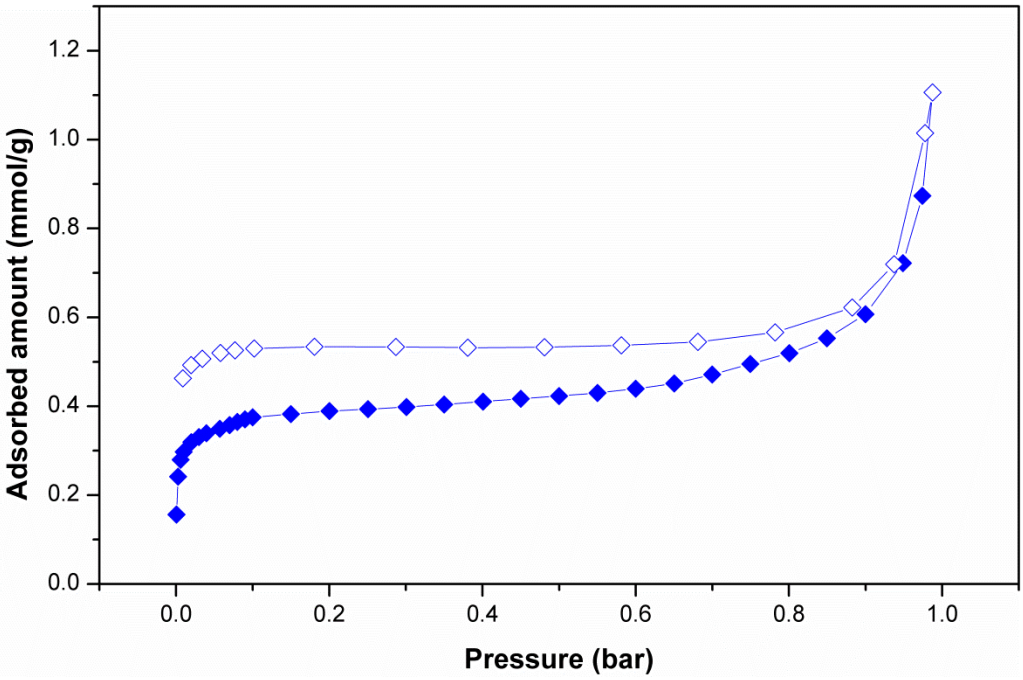

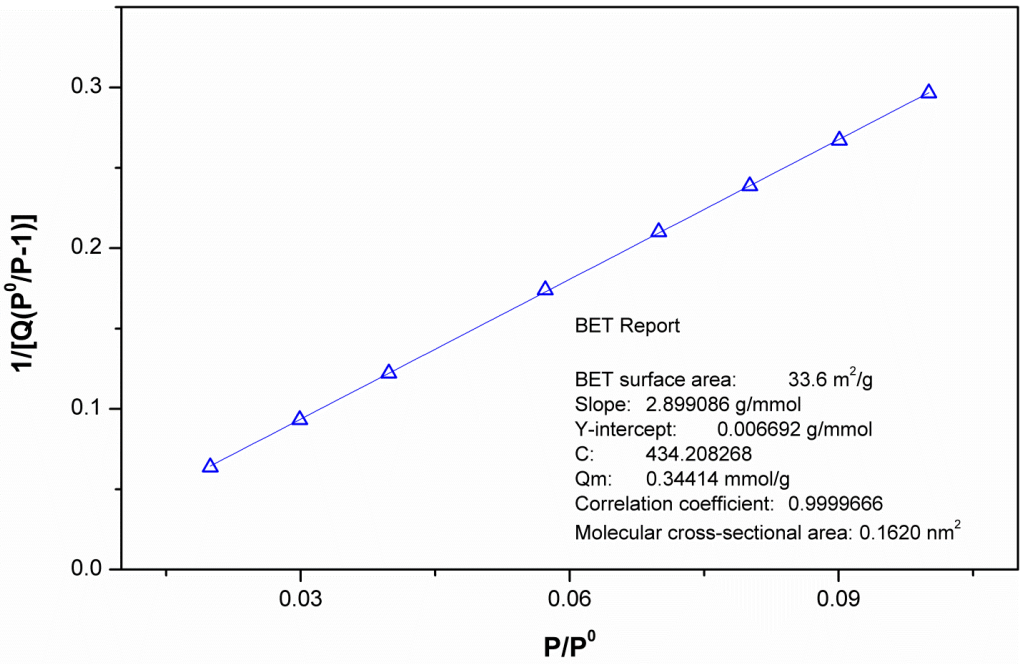

Figure 18. N_2 adsorption isotherm at 77 K and BET plot for compound **3**.

Table 7. Porosity summary of materials.

	BET surface area (m^2/g)	Pore volume (cm^3/g)
Compound 1	1030.4	0.38
Compound 2	1318.4	0.45
Compound 3	33.6	0.03
Zeolite 5A	516.2	0.19

Thermal stability of all three compounds has been characterized by thermogravimetric analysis (TGA). As shown in Figure 19-21.

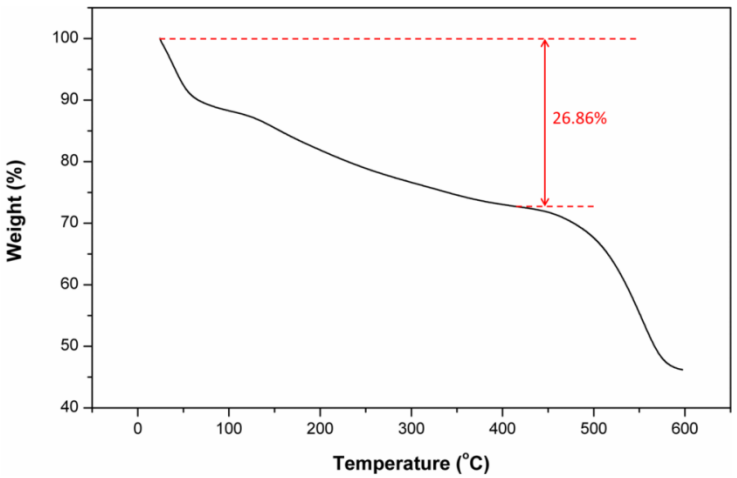

Figure 19. TGA curve of compound **1**.

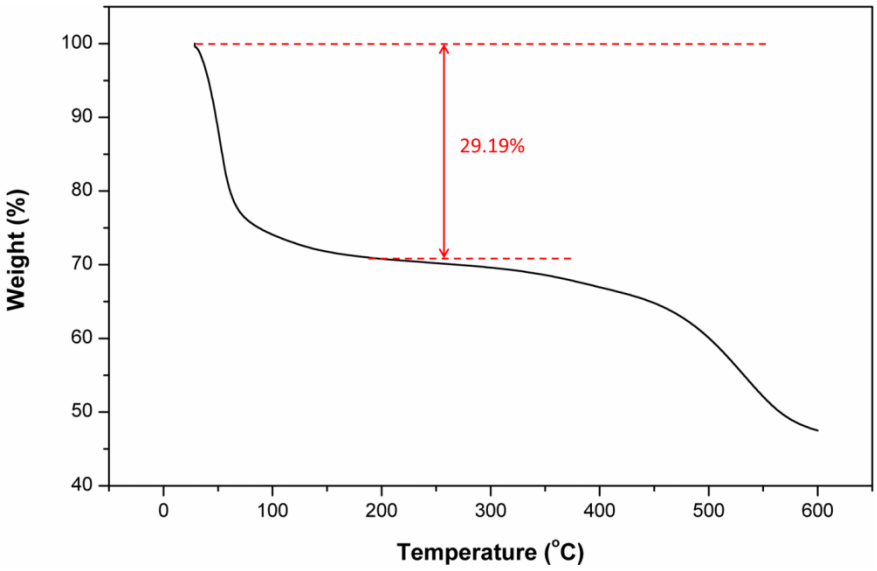

Figure 20. TGA curve of compound **2**.

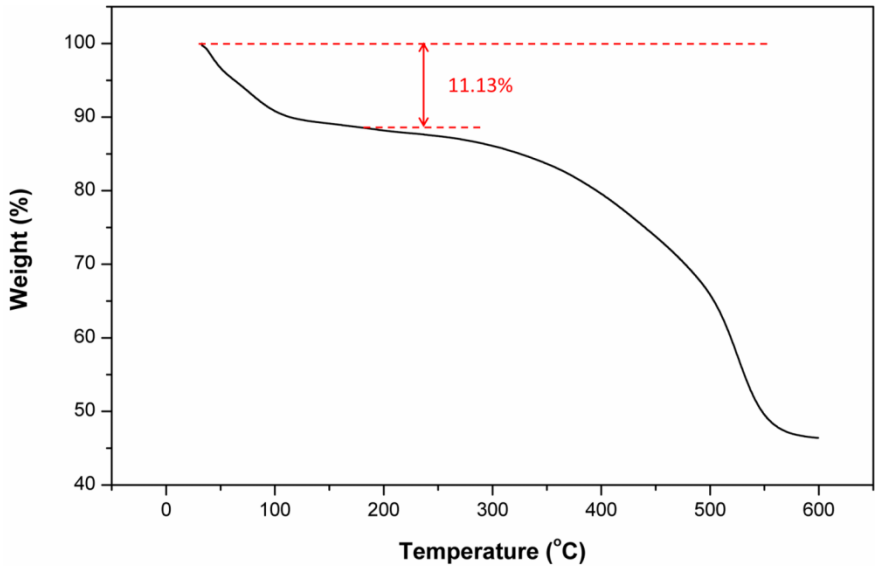

Figure 21. TGA curve of compound **3**.

We also examined the stability of compounds **1** and **2** towards various thermal and water treatments. As shown in Figure 22-27, compound **1** represents a porous MOF with exceptional thermal/water stability. Remarkably, it maintains its crystallinity after being heated at 180 °C in open air for 1 month. It is also stable in aqueous solution with wide pH range or in boiling water. After water treatment for 24 hours its porosity was perfectly retained. Compound **2** also shows very high stability, even though it may not be as robust as compound **1**, as evidenced by the slight decrease in porosity after water treatment. In contrast, compound **3** exhibits very poor stability as it does not show obvious porosity after activation and the structure collapses. Based on the above analysis on their structures and topology, it is clear that the distinct difference in their framework stability correlates to the connectivity of their SBUs. SBUs with higher connectivity will lead to more robust frameworks. This suggests the relatively high stability of Zr-MOFs is not solely originated

from strong Zr-O bonds. Other structural factors, including the geometry and connectivity of both SBU and ligand, all contribute to the overall robustness of the compounds. Additionally, ligand expansion usually results in reticular structures with reduced stability as seen in the case of the UiO-66/67/68 series.[50]

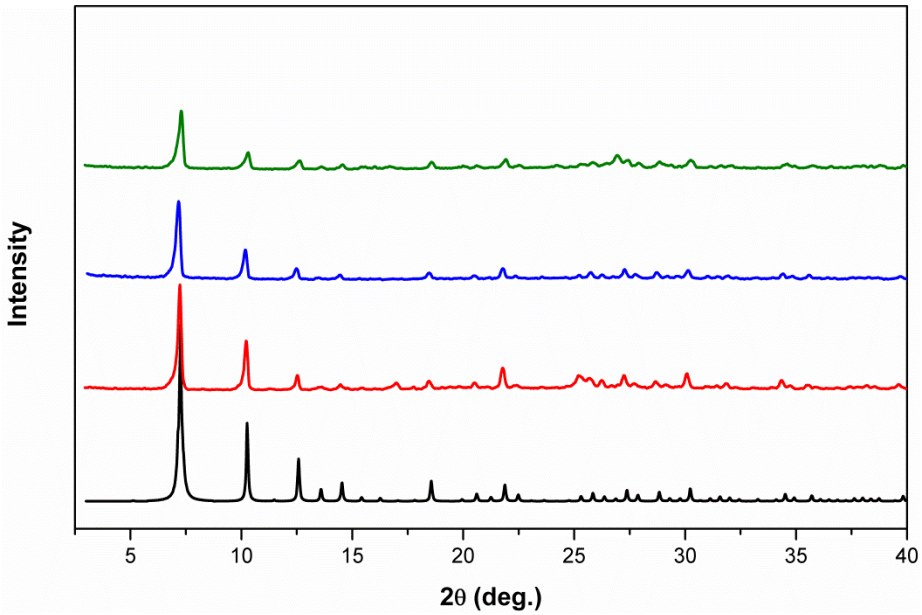

Figure 22. PXRD pattern of compound **1**. From bottom to top: simulated (black), as synthesized (red), activated (blue), after adsorption study (green).

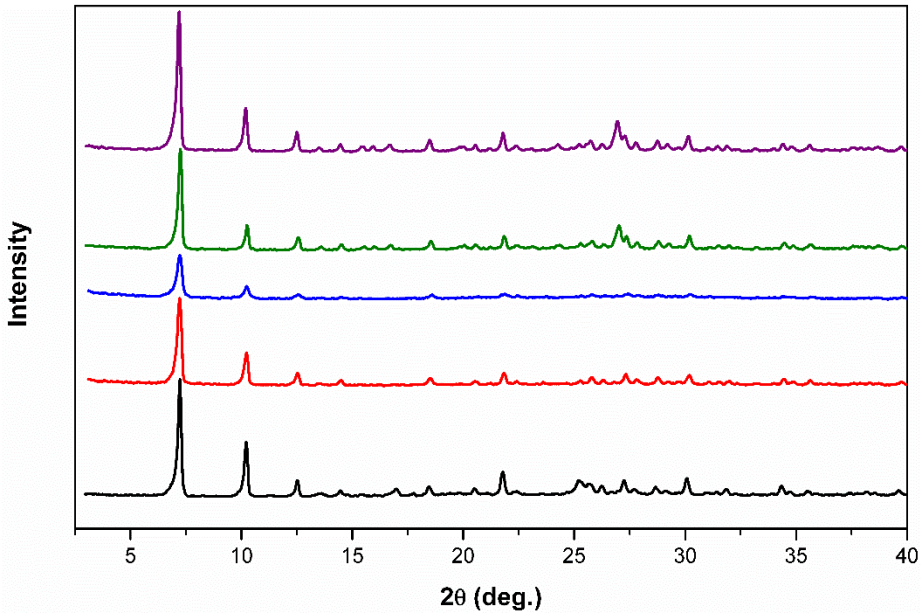

Figure 23. PXRD pattern of compound **1**. From bottom to top: as synthesized (black), 300 °C isothermal for 2 hours in nitrogen (red), 400 °C isothermal for 2 hours in nitrogen (blue), 180 °C in open air for 1 week (green), 180 °C in open air for 1 month (purple).

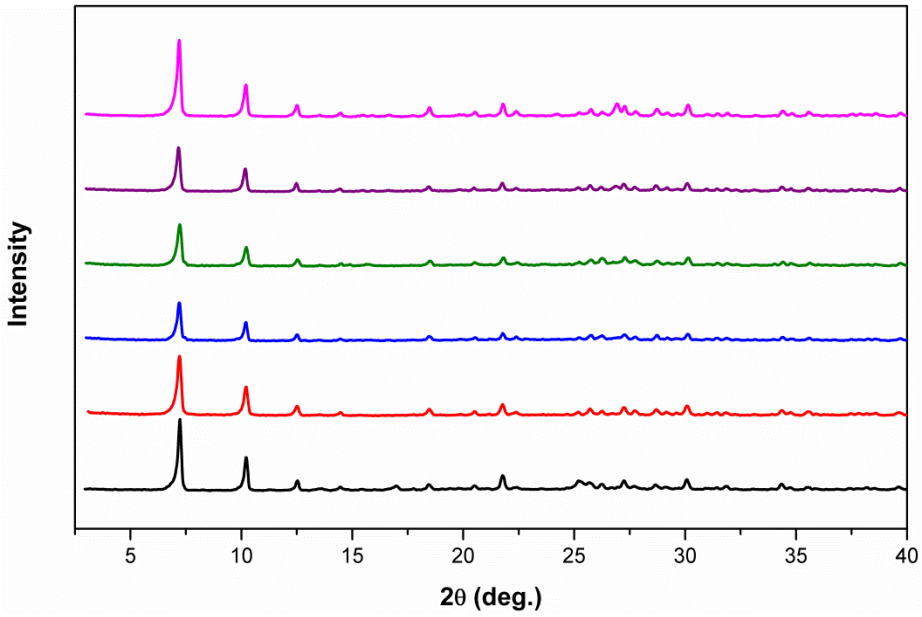

Figure 24. PXRD pattern of compound **1**. From bottom to top: as synthesized (black), immersed in water for 1 week (red), immersed in pH = 2 aqueous HCl solution for 1 week (blue), immersed in pH = 12 NaOH aqueous solution for 1 week (green), immersed in 100 °C water (in teflon bomb) for 1 week (purple), immersed in hexane isomers solution (n-hexane: 3-methylpentane: 2,2-dimethylbutane= 1:1:1) for 1 month (magenta).

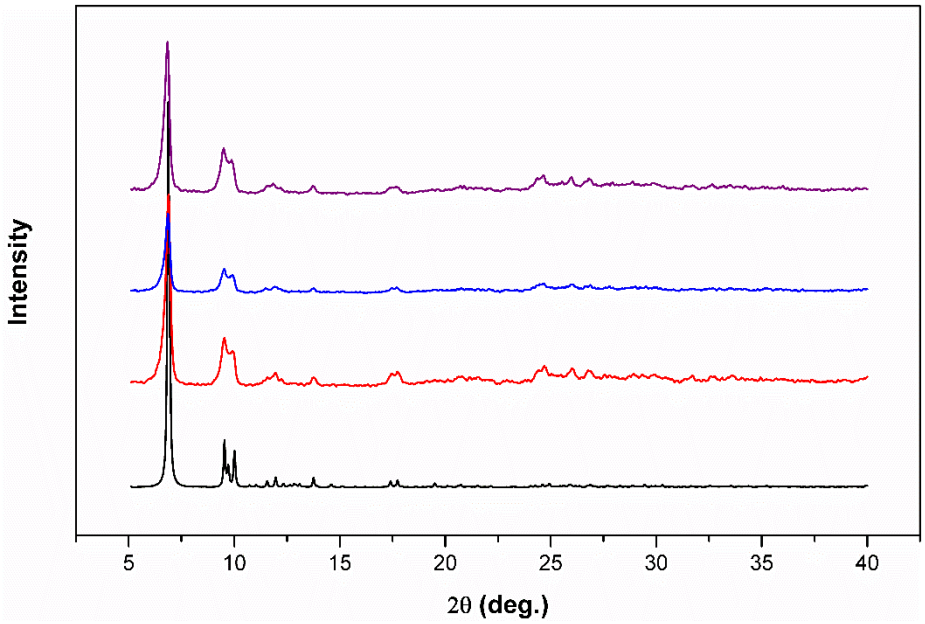

Figure 25. PXRD pattern of compound **2**. From bottom to top: simulated (black), as synthesized (red), after being immersed in H_2O at 80 °C for 3 days (blue), after being heated at 180 °C in open air for 3 days.

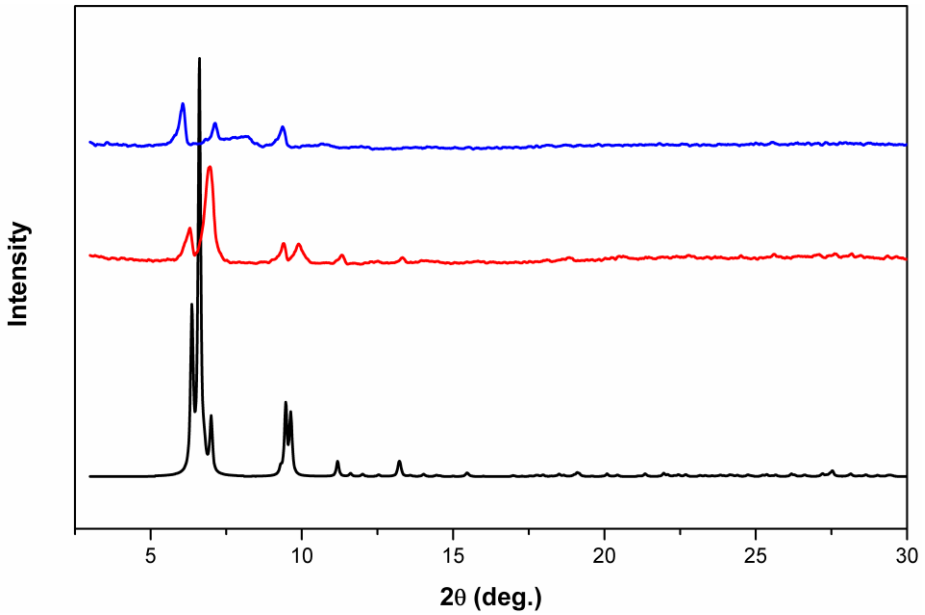

Figure 26. PXRD pattern of compound **3**. From bottom to top: simulated (black), as synthesized (red), activated (blue).

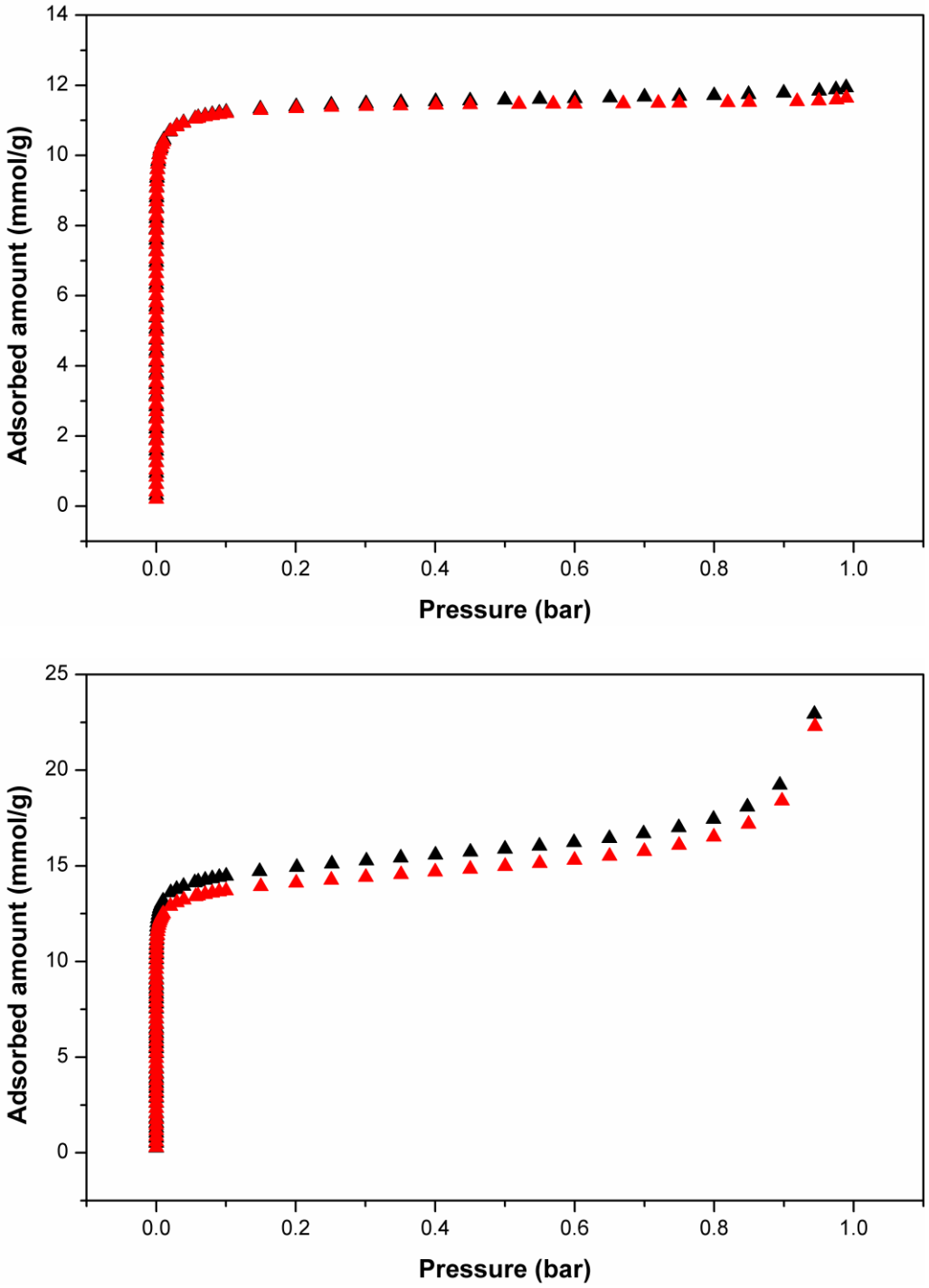

Figure 27. N_2 adsorption isotherm at 77 K before (black) and after (red) water treatment for compound **1** (top) and compound **2** (bottom). (Water treatment: ~100 mg of sample immersed in ~20 mL of water which is heated at 80 °C for 24 hours).

2.6 C6 alkane isomers adsorption and separation

C6 isomers are selected to test the separation performance of compound **1** based on the consideration of its pore structure. Single component equilibrium isotherms of n-hexane were collected on compound **1** at various temperatures (Figure 28-29). At 150 °C, a temperature chosen based on the industrial operation temperature range (100 to 200 °C), compound **1** takes up 130 mg/g n-hexane under a partial pressure of 110 torr, which is ~ 70 % higher than that of the benchmark material zeolite 5A with an uptake of 77 mg/g under the same condition (Figure 31c). To the best of our knowledge, this uptake capacity represents the highest value of any porous material under similar conditions. The ideal pore structure in compound **1** may account for its high n-hexane uptake at high temperature: the large cages guarantee the void space needed to accommodate a large amount of adsorbates while the suited pore aperture serves as a gate to control the diffusion of molecules into the cages. The strength of adsorbent-adsorbate was evaluated by isosteric heat of adsorption (Q_{st}) calculated using adsorption isotherms at high temperatures (180, 200, 220 and 240 °C, Figure 29). A value of 48 kJ/mol was obtained for n-hexane (Figure 30). It is lower than that of zeolite 5A (59 kJ/mol)[45] but significantly higher than that of ZIF-8 (33 kJ/mol).[60] Notably, adsorption kinetics of n-hexane on compound **1** is comparable to that on zeolite 5A at 150 °C and no diffusion restriction was observed (Figure 2.30c). In contrast, compound **1** shows negligible adsorption of 3-methylpentane and essentially no uptake of 2,3-dimethylbutane (Figure 31-33). This is not surprising considering its small window size. The tiny amount of 3-methylpentane taken up by compound **1** may presumably be attributed to the surface adsorption or adsorption at defect sites. This is further confirmed by breakthrough experiments and computational modeling which will be discussed later.

The selective adsorption of n-hexane over the branched isomers by compound **1** follows a similar molecular exclusion mechanism as in the case of zeolite 5A, but with a much higher uptake capacity than the latter. Compound **1** also exhibits excellent recyclability without losing any uptake capacity after ten adsorption-desorption cycles (Figure 33). Additionally, we have reproduced the best performing MOFs reported so far and evaluated and compared their adsorption capacity and selectivity for the separation of C6 alkane isomers. Clearly, only compound **1** demonstrates a performance level comparable with zeolite 5A (Figure 42).

While compound **1** represents a promising alternative to zeolite 5A, compound **2**, on the other hand, appears to be an attractive supplement rather than a substitute. As shown in Figure 34-38, all three hexane isomers can be accommodated into the channel of this compound owing to its larger pore size, and it shows no diffusional limitations for linear or monobranched isomers at any temperature investigated with only slight restrictions for dibranched isomer at low temperature (Figure 40). The adsorption capacity of n-hexane on compound **2** is ~110 mg/g at 150 °C and 110 torr, which is slightly lower than that of compound **1** but higher than that of zeolite 5A and most of the reported materials. Though the channels in compound **2** are large enough to adsorb all three isomers, it exhibits different contact strength toward each individual isomer. As illustrated by the Q_{st} calculations (Figure 39), n-hexane is the most preferentially adsorbed species while the adsorption affinity for the dibranched isomer is the weakest. This can be explained by the degree of contact between the adsorbate and the channel surface: the linear hexane molecules can maximize its van der Waals interaction with the pore surface while the

dibranched isomer is poorest as it is not flexible enough for sufficient contact with the channel.

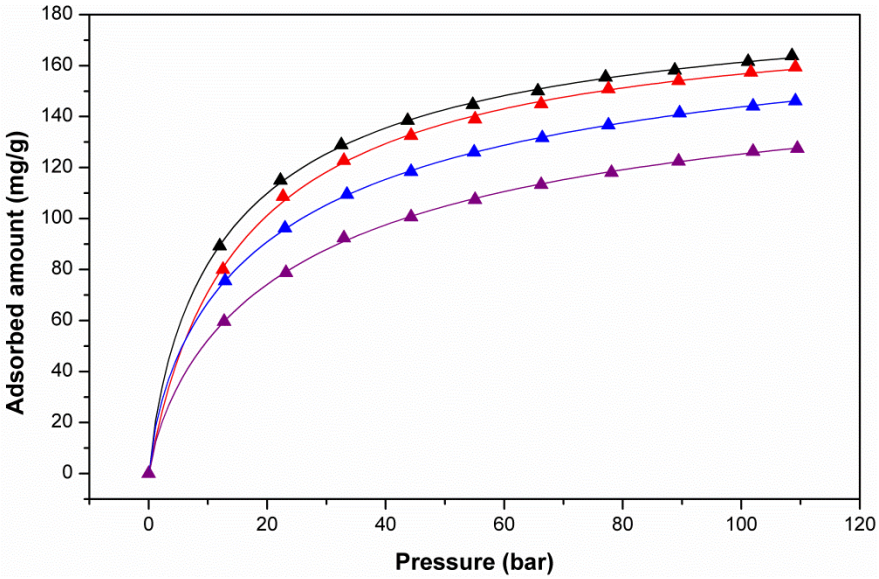

Figure 28. n-hexane adsorption isotherms on compound **1** at 30 °C (black), 90 °C (red), 120 °C (blue) and 150 °C (purple).

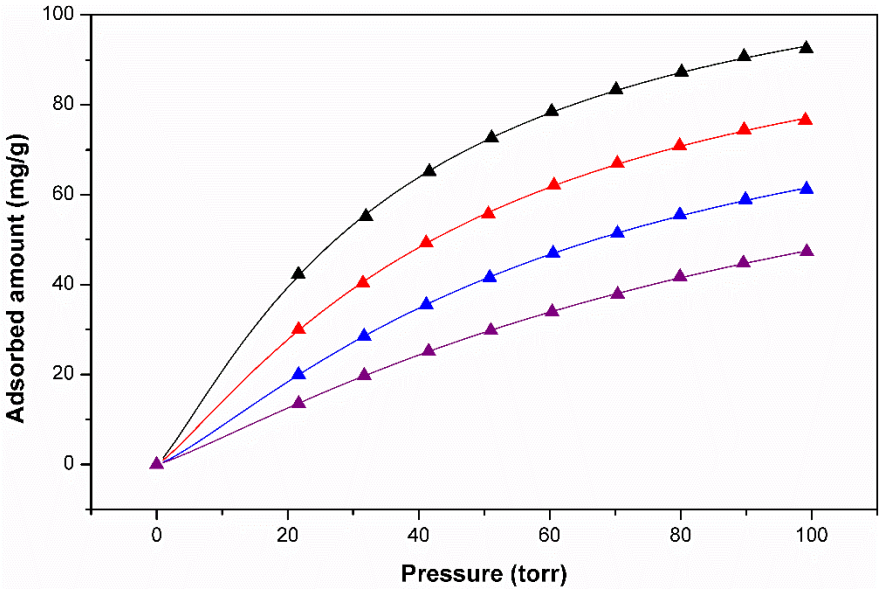

Figure 29. n-hexane adsorption isotherms on compound **1** at 180 °C (black), 200 °C (red), 220 °C (blue), and 240 °C (purple).

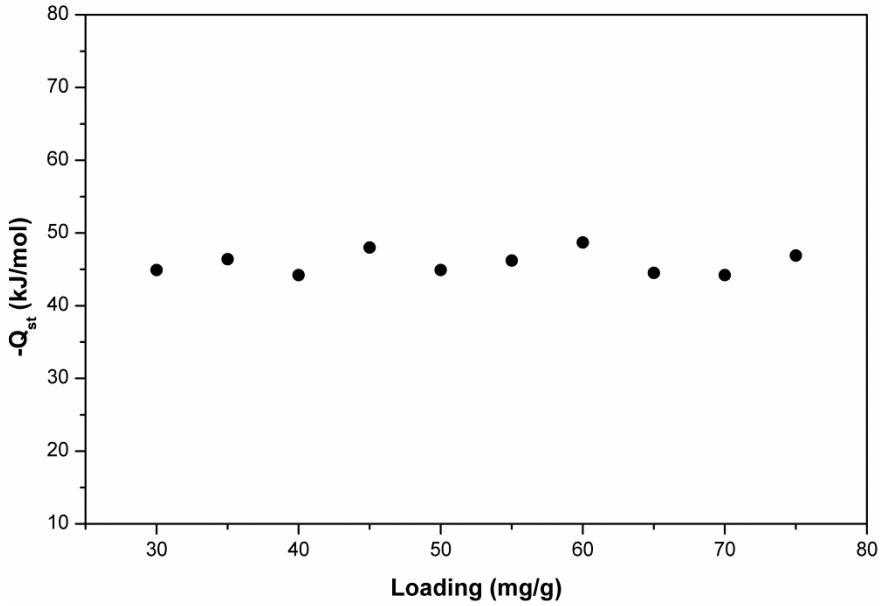

Figure 30. Isosteric heat of adsorption (Q_{st}) for n-hexane adsorption on compound **1**.

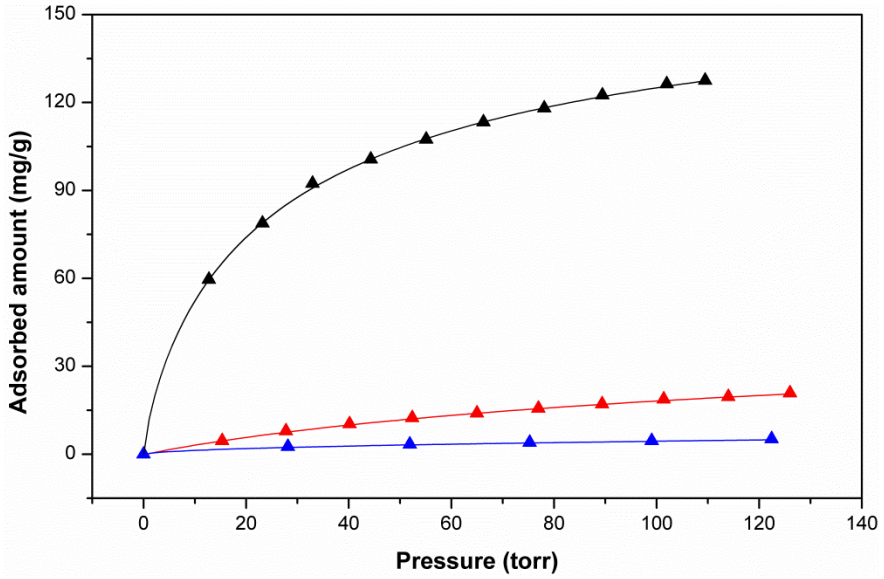

Figure 31. adsorption isotherms of n-hexane (black), 3-methylpentane (red) and 2,3-dimethylbutane (blue) on compound **1** at 150 °C.

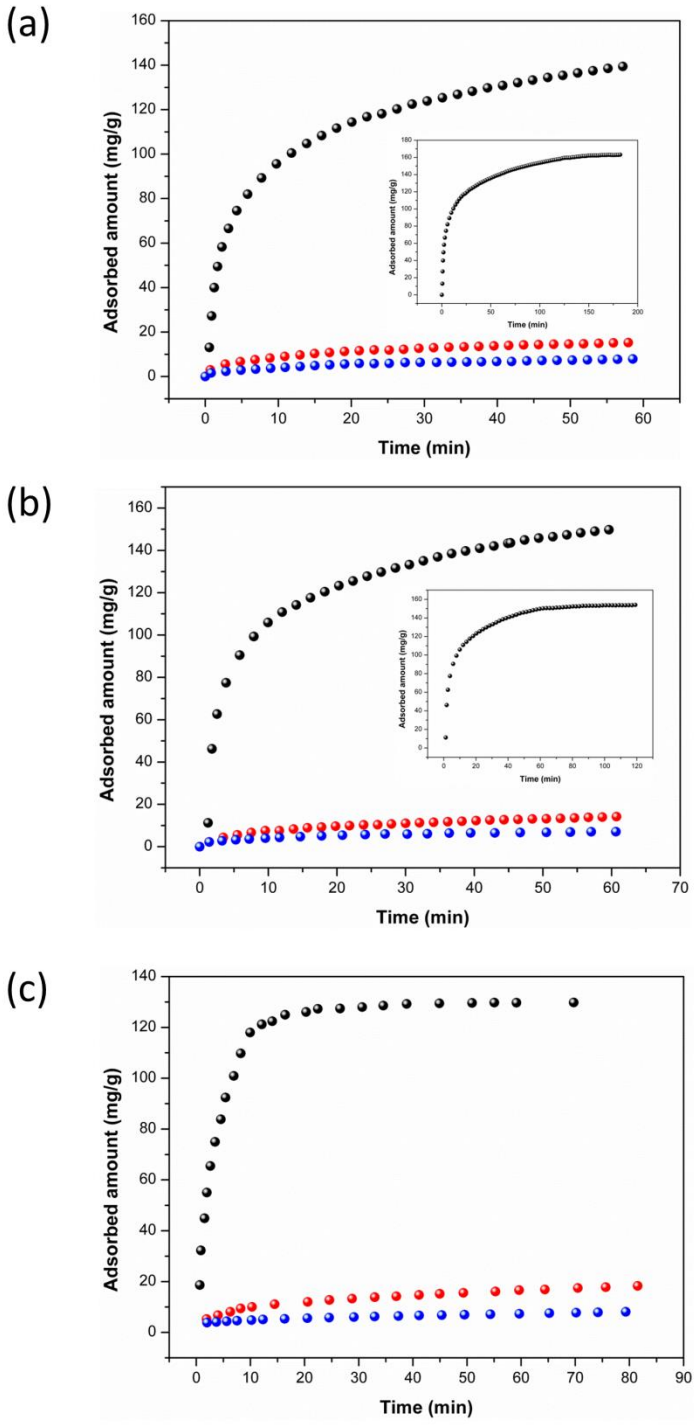

Figure 32. Adsorption of n-hexane (black), 3-methylpentane (red) and 2,3-dimethylbutane (blue) on compound **1** at (a) 30 °C, (b) 90 °C, and (c) 150°C.

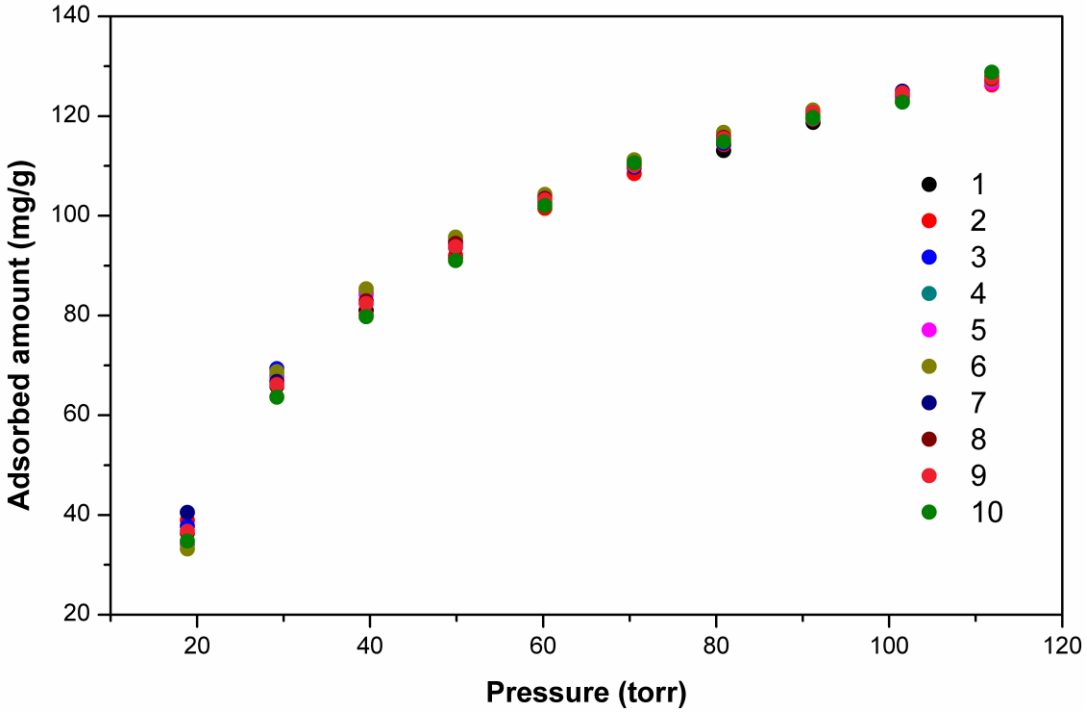

Figure 33. Ten cycles of n-hexane adsorption isotherms on compound **1** at 150 °C (desorption condition: 150 °C for 30 min under nitrogen).

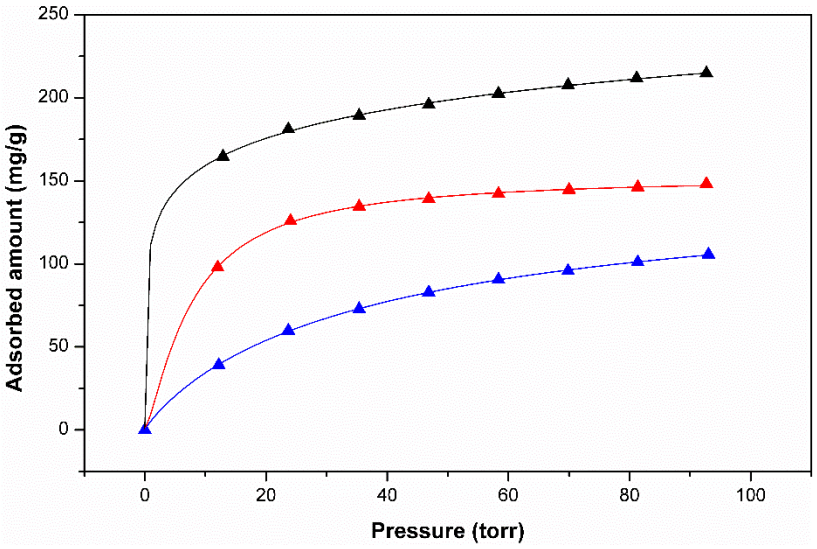

Figure 34. n-hexane adsorption isotherms on compound 2 at 30 °C (black), 90 °C (red) and 150 °C (blue).

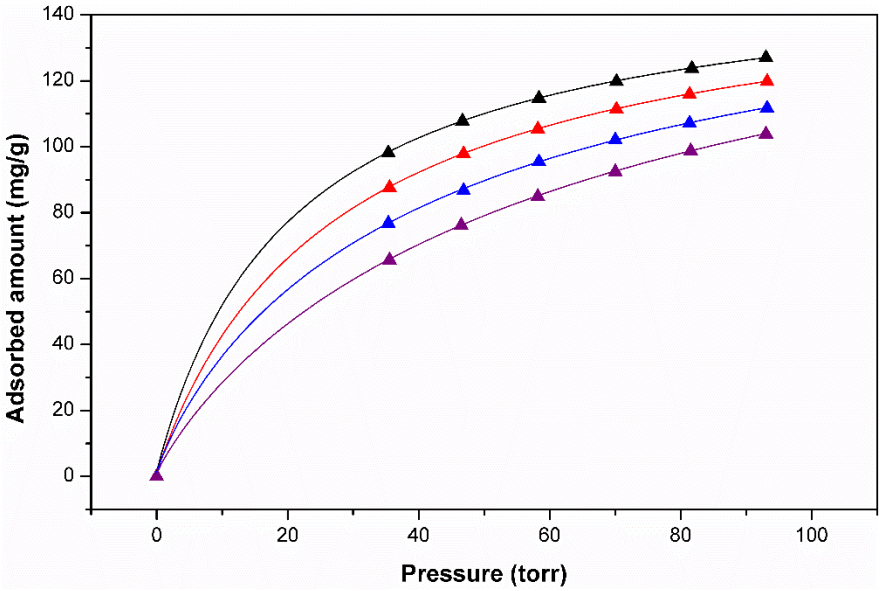

Figure 35. n-hexane adsorption isotherms on compound **2** at 120 °C (black), 130 °C (red) 140 °C (blue) and 150 °C (purple).

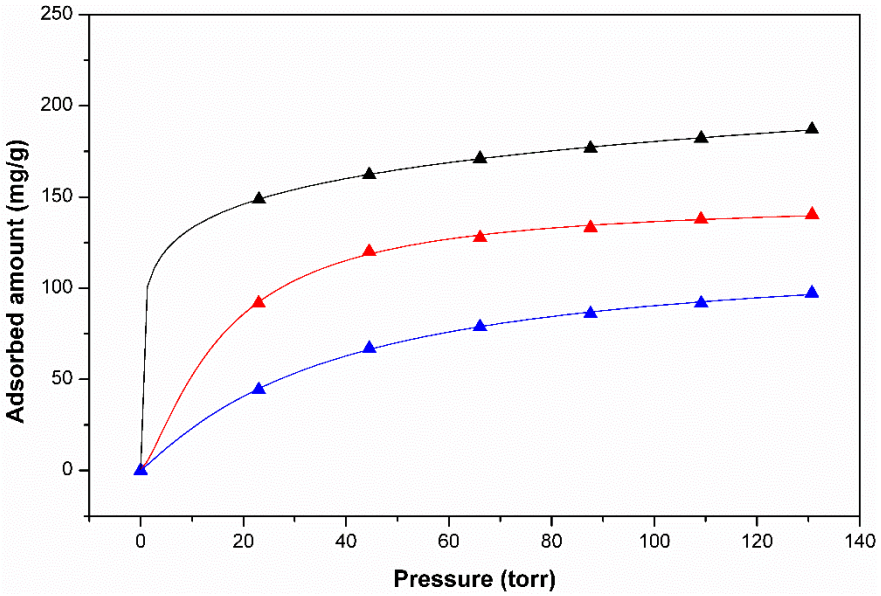

Figure 36. 3-methylpentane adsorption isotherms on compound **2** at 30 °C (black), 90 °C (red) and 150 °C (blue).

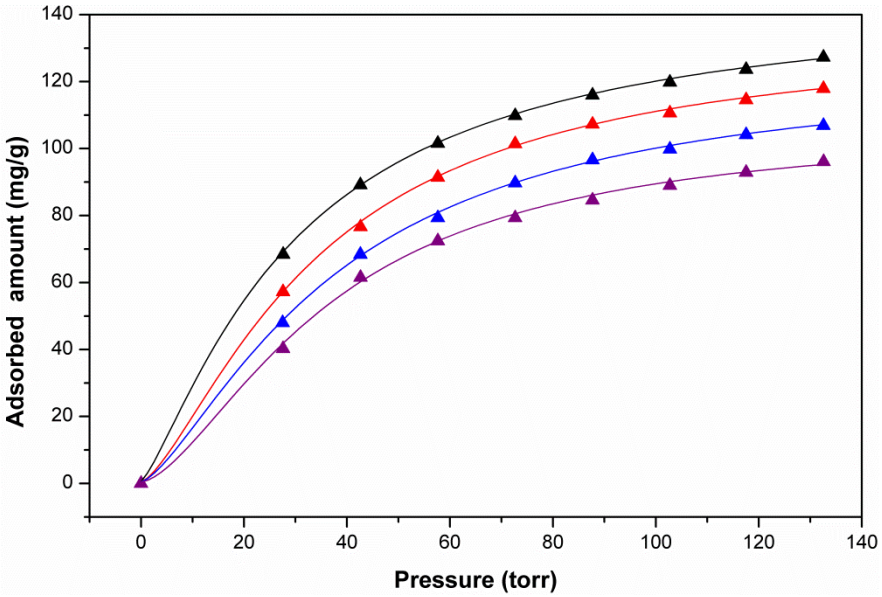

Figure 37. 3-methylpentane adsorption isotherms on compound **2** at 120 °C (black), 130 °C (red) 140 °C (blue) and 150 °C (purple).

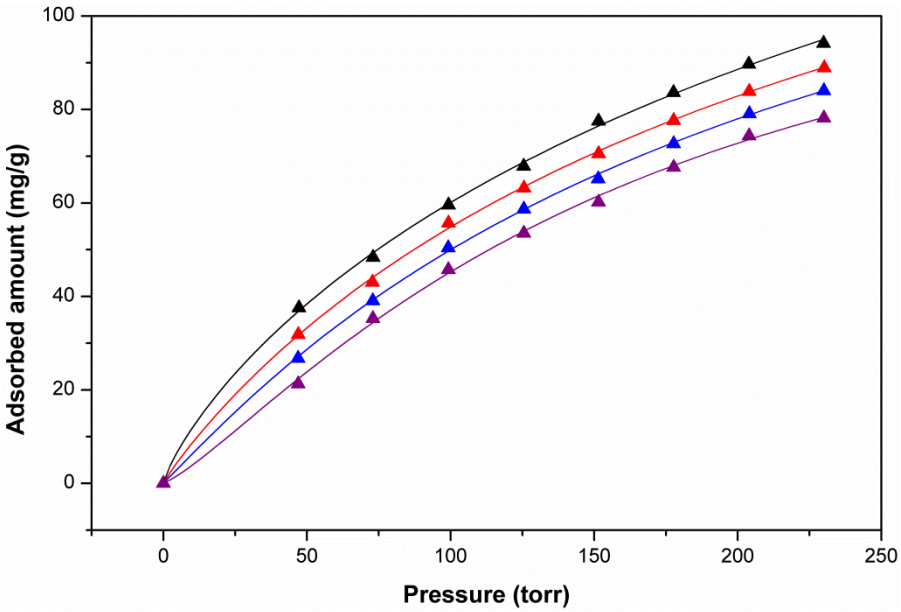

Figure 38. 2,3-dimethylbutane adsorption isotherms on compound **2** at 120 °C (black), 130 °C (red) 140 °C (blue) and 150 °C (purple).

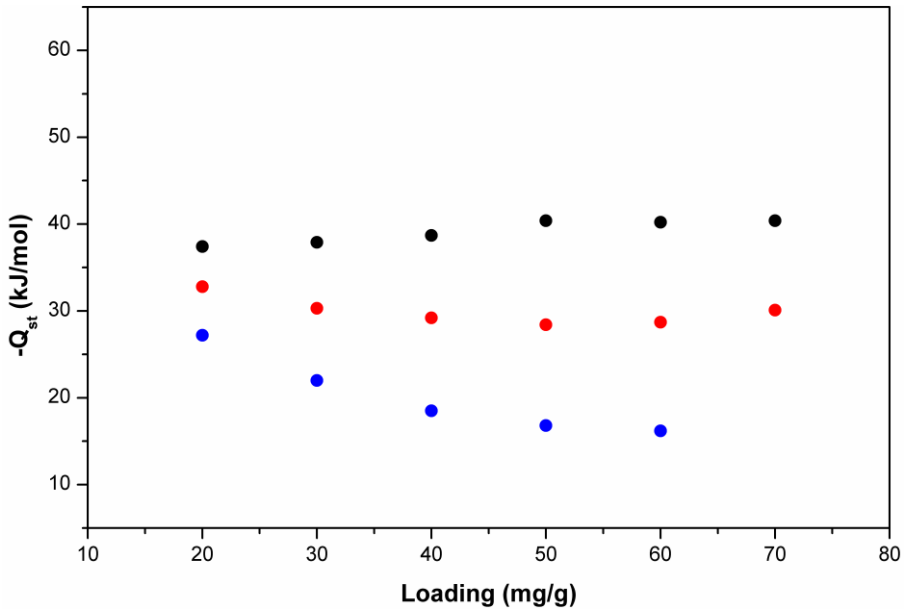

Figure 39. Isosteric heat of adsorption (Q_{st}) for n-hexane (black), 3-methylpentane (red) and 2,3-dimethylbutane (blue) adsorption on compound **2**.

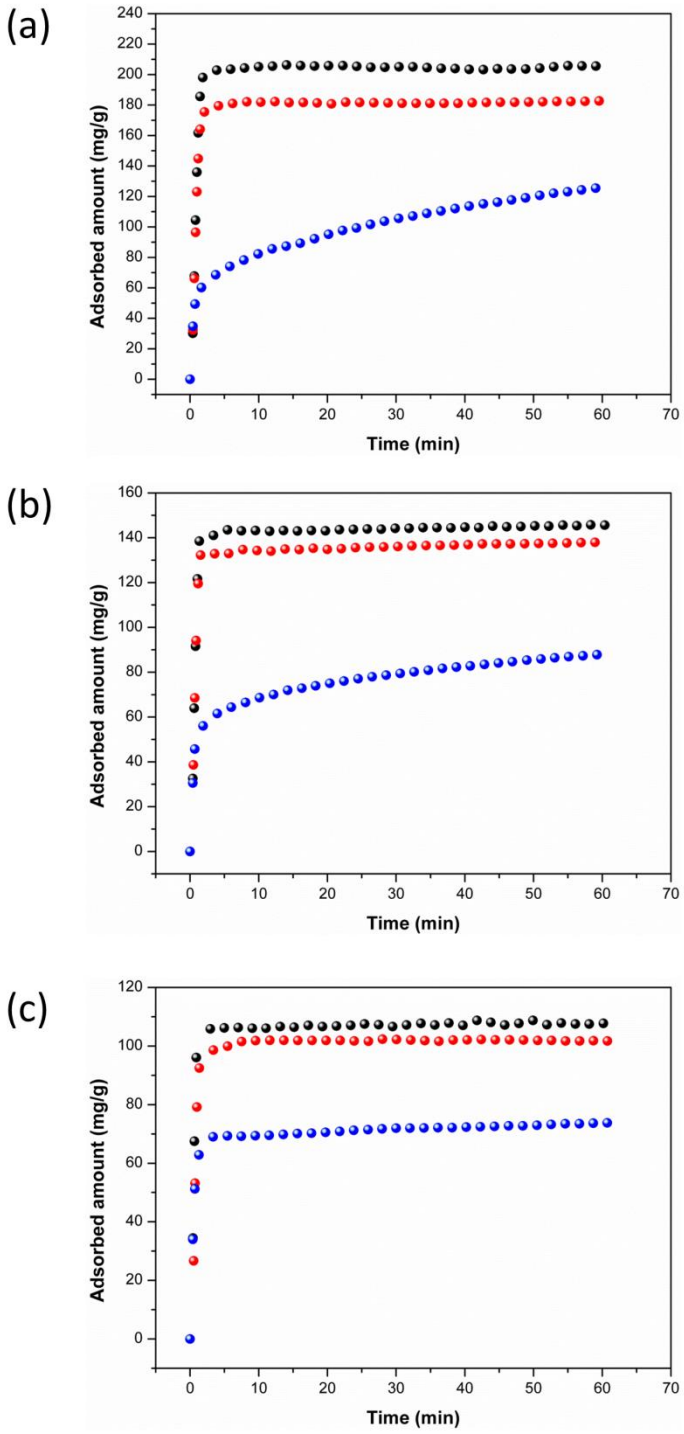

Figure 40. Adsorption of n-hexane (black), 3-methylpentane (red) and 2,3-dimethylbutane (blue) on compound **2** at (a) 30 °C, (b) 90 °C, and (c) 150°C.

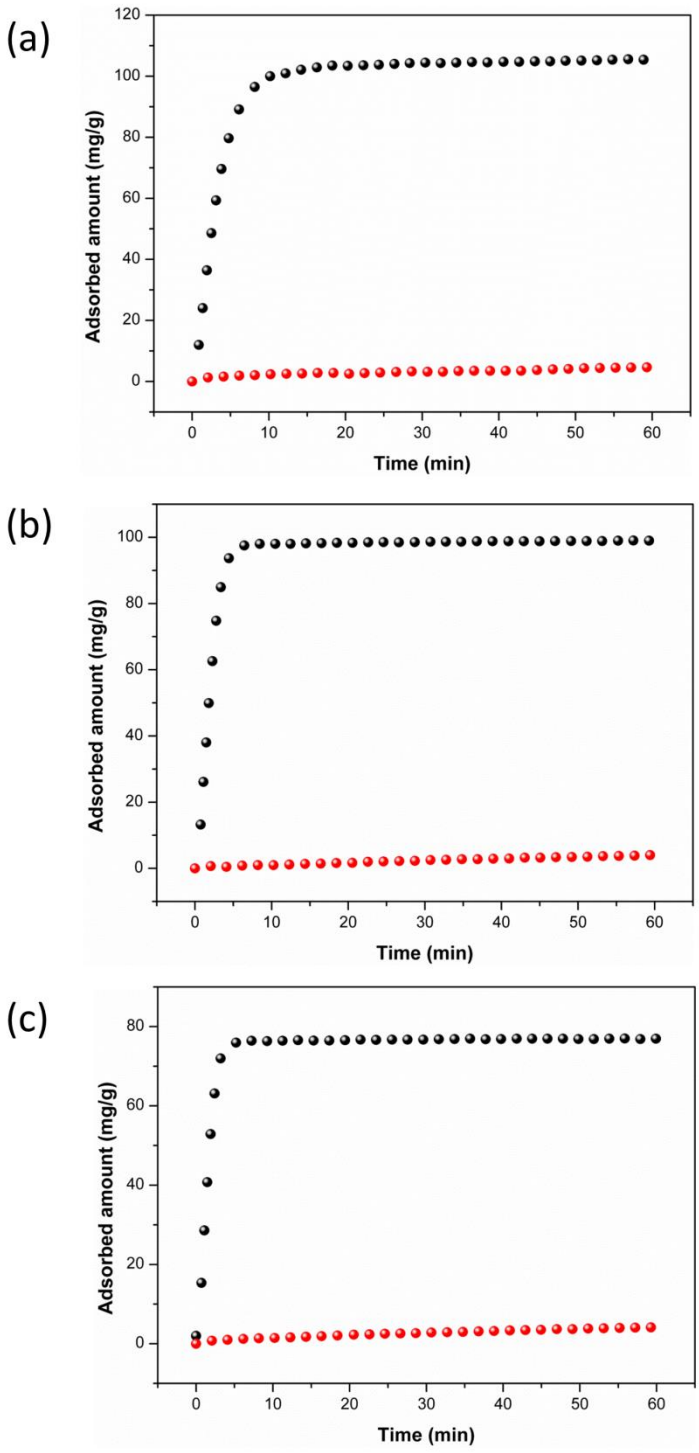

Figure 41. Adsorption of n-hexane (black) and 3-methylpentane (red) on zeolite 5A at (a) 30 °C, (b) 90 °C, and (c) 150°C.

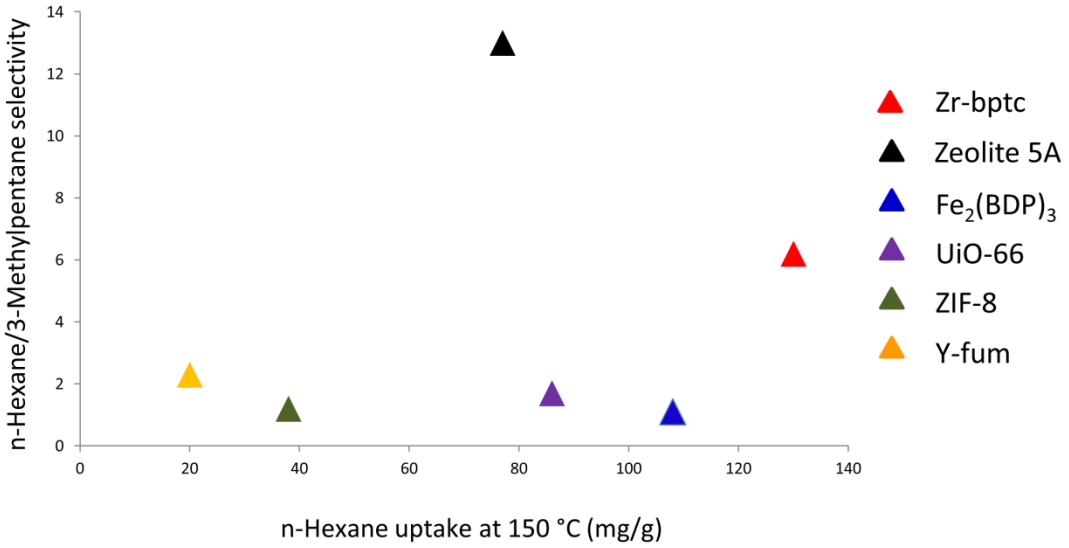

Figure 42. N-hexane uptake and n-hexane/3-methylpentane uptake ratio for various materials at 150 °C (150 °C and 100 torr). Selectivity was estimated as the ratio of uptake. Data for $Fe_2(BDP)_3$ were taken from Science 340, 960-964. Data for all other materials were collected in this work.

To mimic real-world conditions, it is important to carry out adsorption experiments with mixed adsorbates. To evaluate the capability of the title compounds for separating C6 alkane isomers under such conditions, we conducted column breakthrough experiments on both compounds **1** and **2** with an equimolar mixture of all three isomers at 150 °C. Measurements under identical experimental conditions were also performed on zeolite 5A for comparison. The results are shown in Figure 43-45. Both compound **1** and zeolite 5A adsorb n-hexane exclusively. While branched C6 alkanes elute immediately, linear isomer shows a delayed retention. The real-time RON curves of the eluted product are also plotted in the figure. Before the breakthrough of n-hexane, the RON values are higher than 90 for

both adsorbent materials, meeting the industrial standard for refined hexane blends (RON = 83). Under the same experimental conditions, n-hexane breaks at the 59th minute on zeolite 5A and at the 118th minute on compound **1**, meaning the dynamic adsorption capacity (before breakthrough) of the latter is twice of that of the former. This is a significant improvement considering the fact that compound **1** retains the merit of complete exclusion of the branched isomers.

As stated above, branched alkanes (both monobranched and dibranched) break immediately from the column of zeolite 5A or compound **1**, suggesting neither of these two materials is able to separate isomers of different degrees of branching. In contrast, compound **2** shows clean separation of monobranched and dibranched hexane isomers. As shown in Figure 45, breakthrough results for compound **2** indicate that the dibranched isomer elutes first from the column. 3-methylpentane elutes at a much later time which is followed by n-hexane. The breakthrough times are 112, 151, and 166 minutes for the dibranched, monobranched, and linear isomer, respectively. The steepness of the breakthrough events for all three isomers suggests that there are no diffusion restrictions and the separation is thermodynamically controlled. This is consistent with the single component adsorption results where compound **2** shows equilibrium adsorption toward all isomers at 150 °C but with different uptake amount and adsorption affinity. Notably, at the beginning of the breakthrough experiment, the eluted product has a RON higher than 100, well above the value for the state-of-the-art benchmark material zeolite 5A. This can be attributed to the material's ability to separate monobranched and dibranched alkane isomers, making it possible to obtain pure dibranched isomer with the highest RON value. This development is significant for the petroleum refinement industry as it offers a method

to further improve the quality of commercial gasoline. Breakthrough measurements at 30 °C show that the separation ability is retained in all three compounds with higher uptake capacity and more diffusion restrictions.

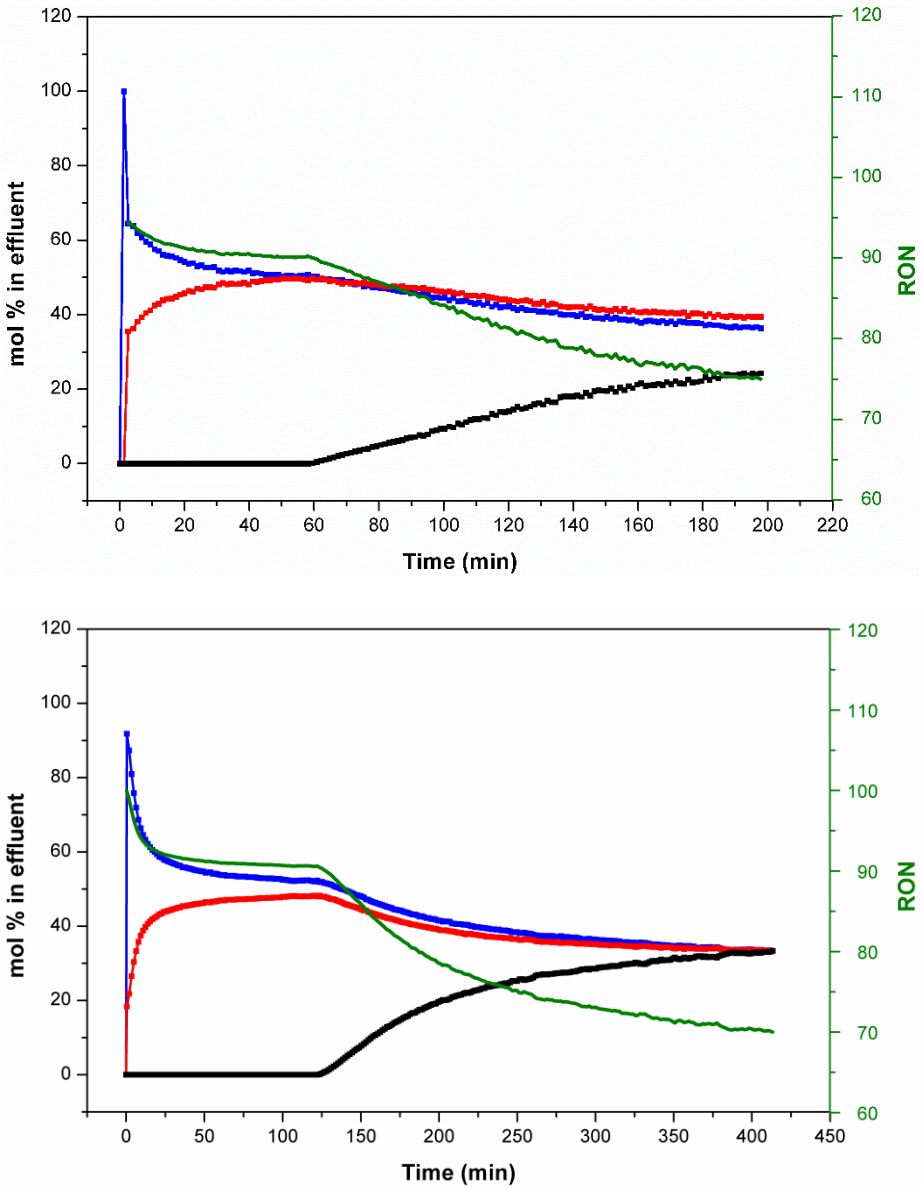

Figure 43. Separation of n-hexane (black), 3-methylpentane (red) and 2,3-dimethylbutane (blue) running through a packed bed of zeolite 5A at 150 °C (top) and 30 °C (bottom). Green curve indicates the RON of the eluted mixture.

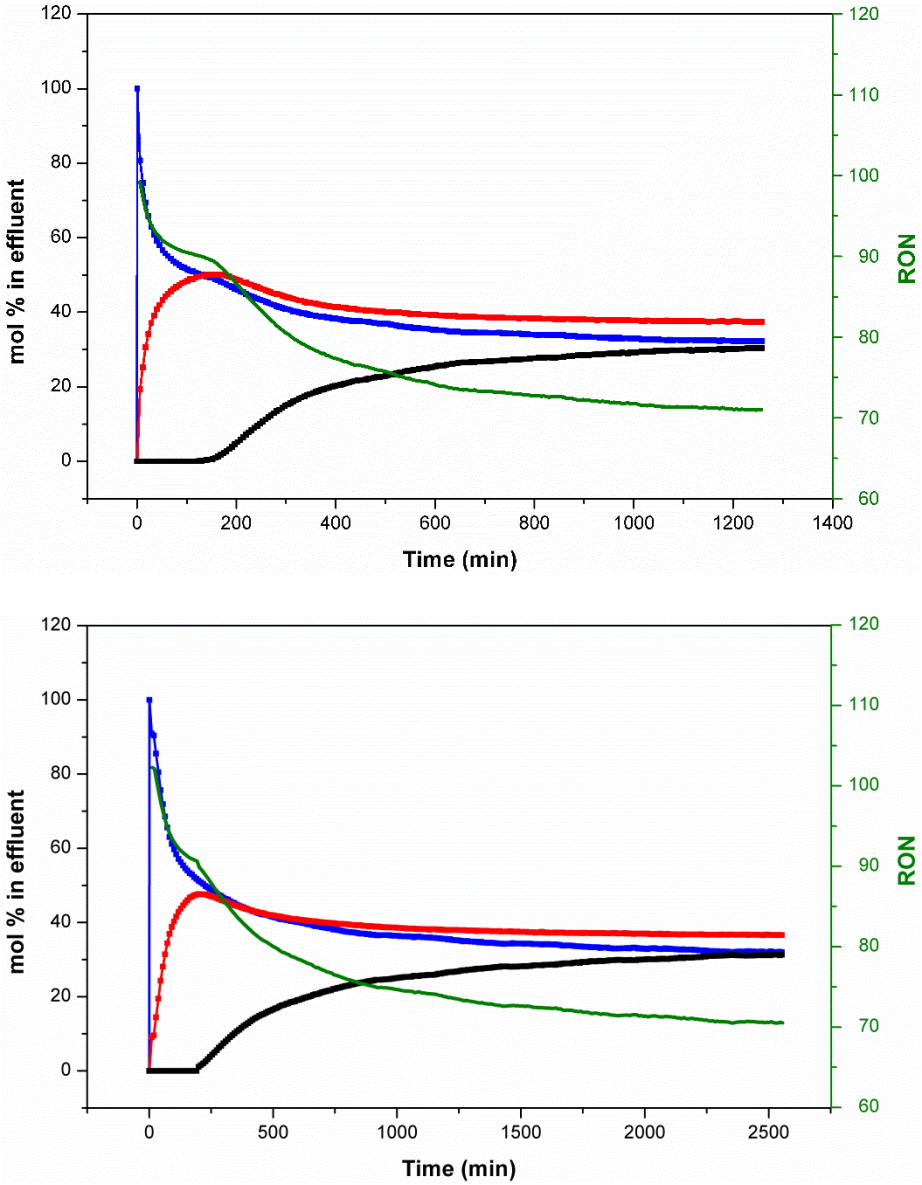

Figure 44. Separation of n-hexane (black), 3-methylpentane (red) and 2,3-dimethylbutane (blue) running through a packed bed of compound **1** at 150 °C (top) and 30 °C (bottom). Green curve indicates the RON of the eluted mixture.

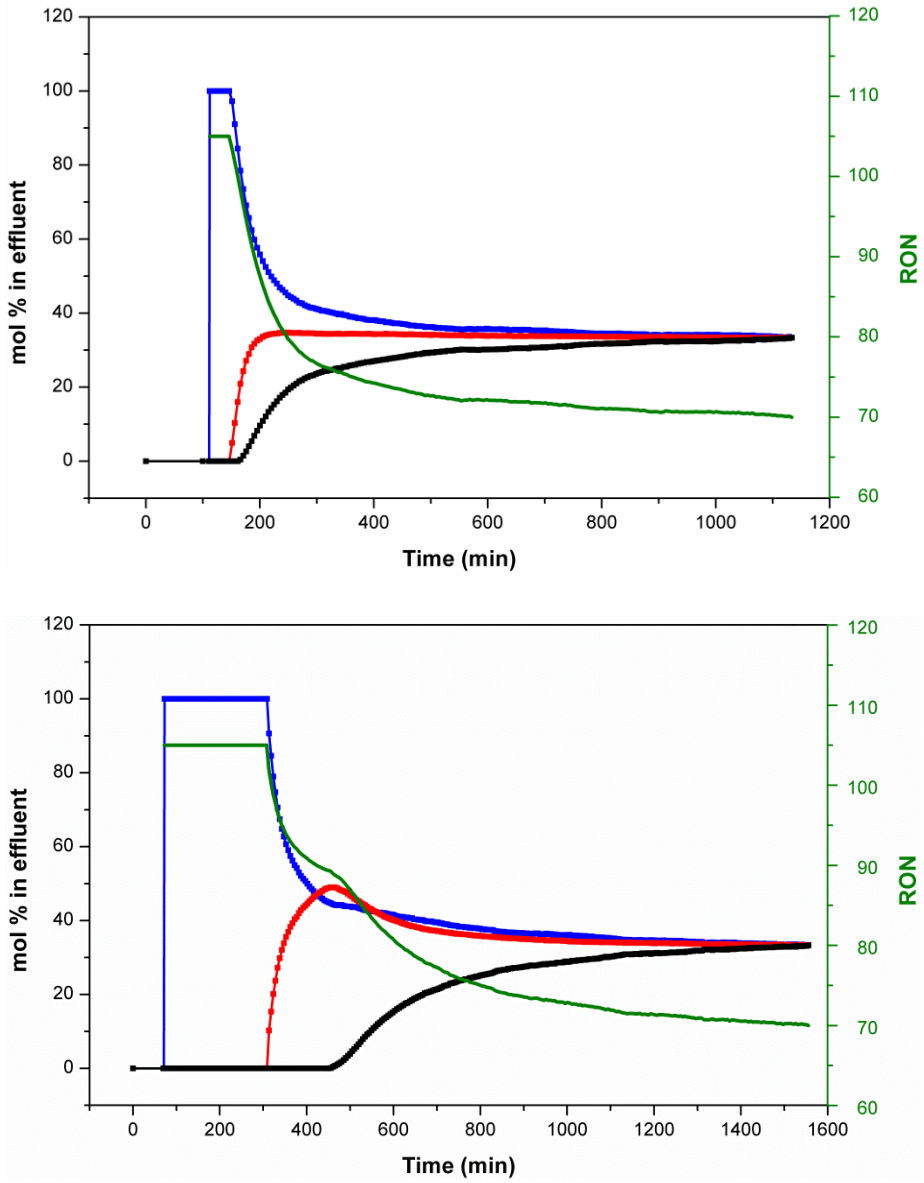

Figure 45. Separation of n-hexane (black), 3-methylpentane (red) and 2,3-dimethylbutane (blue) running through a packed bed of compound **2** at 150 °C (top) and 30 °C (bottom). Green curve indicates the RON of the eluted mixture.

2.7 Discussion and conclusion

Efficient separation of hydrocarbons via selective adsorption by porous solids requires precise control of their pore structure. On the basis of reticular chemistry, metal-organic frameworks having specific structure types can be synthesized by judicious selection of

inorganic clusters and organic linkers. This designing strategy, combined with the general high stability of Zr-MOFs, offers an unprecedented opportunity to develop high performance adsorbent materials with desirable structure types and optimal pore shape/size for targeted separation processes. In this study, we analyze the framework stability of various structure topologies and the influence of ligand geometry (aspect ratio) on the SBU connectivity and resulting structure types. Guided by such analysis, we have achieved a new ***ftw*** structure with cage-like pores. Compound **1** possesses exceptionally high framework stability and optimized pore aperture. It selectively adsorbs n-hexane but excludes its branched isomers, with an adsorption capacity that outperforms the commercial benchmark material, zeolite 5A.. Column breakthrough experiments on a mixture of three C6 isomers show that compound **1** adsorbs linear alkane exclusively, in a similar manner to zeolite 5A but with much higher uptake capacity. Use of ligand with higher aspect ratio yields a ***scu*** structure with channel-like pores. This material (compound **2**) is capable of separating mono- and di-branched alkane isomers with a very high RON value (> 100). Such a separation is not achievable by the benchmark adsorbent zeolite 5A and may offer a supplementary technology for the petroleum refinement industry in further improving the octane rating of commercial gasoline products.

3. Screening and synthesis of microporous MOFs for noble gases separation

3.1 Background: noble gases separation

Noble gases, with the exception of argon which makes up close to 1% of air, are all present in very low abundance especially krypton (Kr) and xenon (Xe) which occurs naturally in the atmosphere at 1.1 parts per million by volume (ppmv) and 0.09 ppmv, respectively. Noble gases are valuable commodities and are extensively needed for various industrial applications. For example, Xe finds its uses in illumination, optics, medical science, etc.[61-63] It has been recognized that Xe outperforms laughing gas (nitrous oxide) which is currently used as anesthetics in various aspects. However, the extremely high price (> 10000 USD per m^3) has been an obstacle to its wide use, which should be attributed to its trace concentration in air and the difficulty of its extraction and purification. Xe typically exists in a Xe/Kr stream as a byproduct during air separation processes where further cryogenic distillation will afford pure components of the two gases. However, this purification process is highly energy and capital intensive.

Adsorptive separation by porous solids has proven a promising alternative to heat-driven distillations which offers higher energy efficiency and emits less carbon dioxide. Over the past years, various sorbent materials have been evaluated for the adsorption and separation of Xe from its analogues.[64] For example, tris(*o*-phenylenedioxy)cyclotriphosphazene (TPP),[65] a zeolite-like material having a pore diameter of ~ 4.5 Å, can adsorb 1.7 mmol/g of Xe at 298 K and 1 bar. Thallapally et al. reported that NiDOBDC, a microporous MOF with high density of open metal sites, shows a Xe uptake of 4.2 mmol/g at 298 K and 1 bar.[66] Although the reported materials are shown to have potential for Xe capture and

purification, they have yet exhibited high adsorption selectivity. Snurr et al. analyzed over 137000 hypothetical MOFs by high-throughput computational method and drew the conclusion that MOFs with tube-like, uniform pores that are just large enough to fit a single Xe atom are ideal for Xe/Kr separation.[67]

3.2 materials screening

With the above-mentioned hypothesis in mind, we examined a number of microporous MOFs and finally we focused our effort on $Co_3(HCOO)_6$ (CoFA) for the following reasons. 1) CoFA is a simple framework composed of Co^{2+} cations and formate, with facile, scalable synthesis. 2) CoFa possesses high thermal and air/moisture stability. 3) CoFA features one-dimensional (1D) channels with diameter of ~ 5Å, slightly larger than the kinetic diameter of a Xe atom (4.1 Å).[68] Before experimentally evaluation, we performed adsorption simulations on CoFa crystal structure with Materials Studio software (Accelrys Inc.). In this modeling system, the GCMC method and Burchard Universal Force Field are employed. Typically, the modeling is performed on a unit of ~ 40 × 40 × 40 Å of the framework structure which contains several unit cells. To gain insight into the shape of the channels, we first conducted adsorption of helium (He) at 1 K and 1 bar. As shown in Figure 47, the packing of He atoms depicts a 1D zig-zag channel with repeating segments but with uniform pore width. We then further performed Xe and Kr adsorptions at room temperature and 1 bar with results plotted out in Figure 47b and 47c. Each unit cell takes up four Xe atoms with one Xe “frozen” in each zig or zag segment. In contrast, Kr atoms are randomly located along the channel and the uptake amount is much lower than that of Xe. These simulation results indicate the framework preferentially adsorbs Xe over Kr.

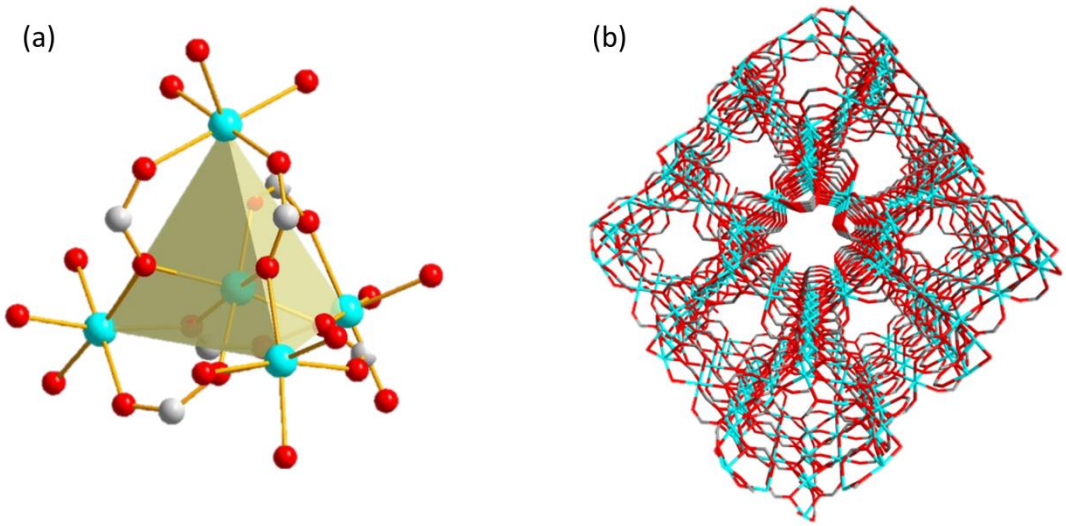

Figure 46. Crystal structure of CoFA. (a) Co_5 building unit. (b) perspective view of the framework along b axis.

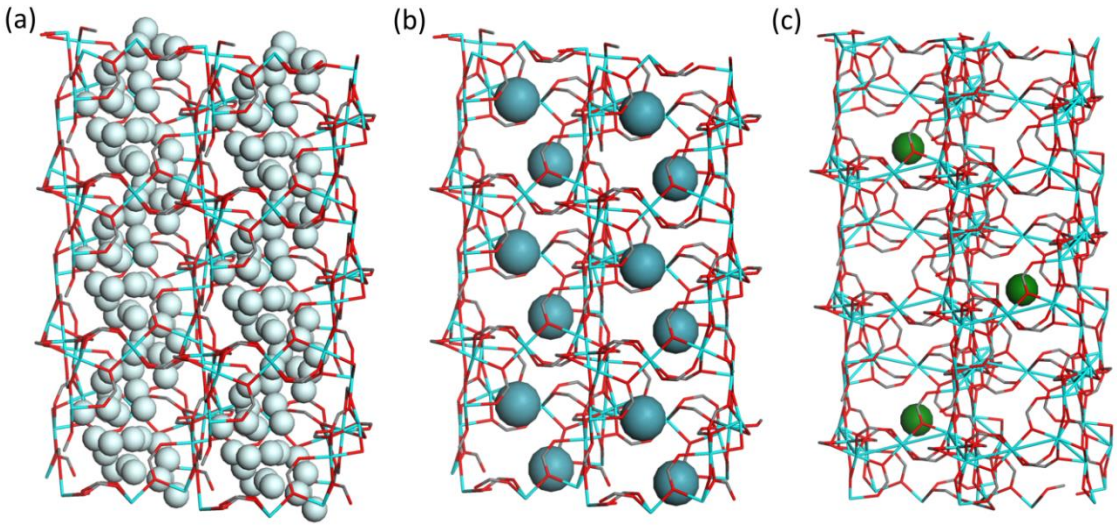

Figure 47. Adsorption simulations on CoFA. (a) He simulation at 1 K and 1 bar. (b) Xe (c) Kr simulation at 298 K and 1 bar.

3.3 material synthesis, characterization, and single component gas adsorption

To experimentally confirm our simulation results, we reproduced CoFA sample and studied its performance for noble gas adsorption and separation. The sample synthesis was performed following literature with slight modifications: A mixture of Cobalt (II) nitrate

hexahydrate (1.309g, 4.4 mmol) and formic acid (1mL, 25.7mmol) in DMF (10 mL) in a glass vial was heated at 100 °C for 24 hours and then cooled to room temperature. The resultant pink powder was filtered, rinsed with DMF (10 mL) and dried under air. The phase purity was confirmed by powder X-ray diffraction (PXRD) analysis (Figure 48 a). Thermogravimetric analysis (TGA) indicates the material is stable up to 250 °C (Figure 48b)

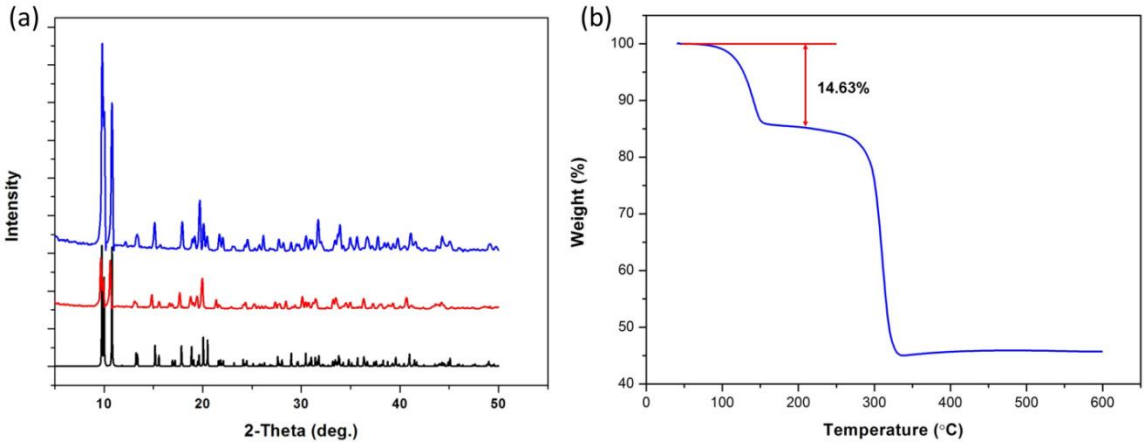

Figure 48. (a) PXRD patterns of CoFA. From bottom to top: simulated (black), as synthesized (red), and after adsorption study (blue). (b) TGA curve of CoFA.

Single component gas adsorption-desorption isotherms of Xe, Kr, and Ar were collected on CoFA at different temperatures (278, 288, and 298 K) with Autosorb (Quantachrome Instruments) volumetric adsorption analyzer. The as synthesized CoFA sample was activated by direct heating at 150 °C overnight under dynamic vacuum to remove initial solvent residing inside the MOF channels. As shown in Figure 49a, Xe sorption on CoFA is fully reversible and the isotherms exhibit a typical type I adsorption profile. At 1 bar, the uptake of Xe reach the same amount (~ 2 mmol/g, corresponding to one atom per segment or four atoms per unit cell) at three different temperatures (278, 288, and 298 K),

which agrees well with the adsorption simulation results and represents a strong evidence of commensurate adsorption. To the best of our knowledge, this is the first example of commensurate adsorption of atoms (atomic adsorbates) in a MOF material.

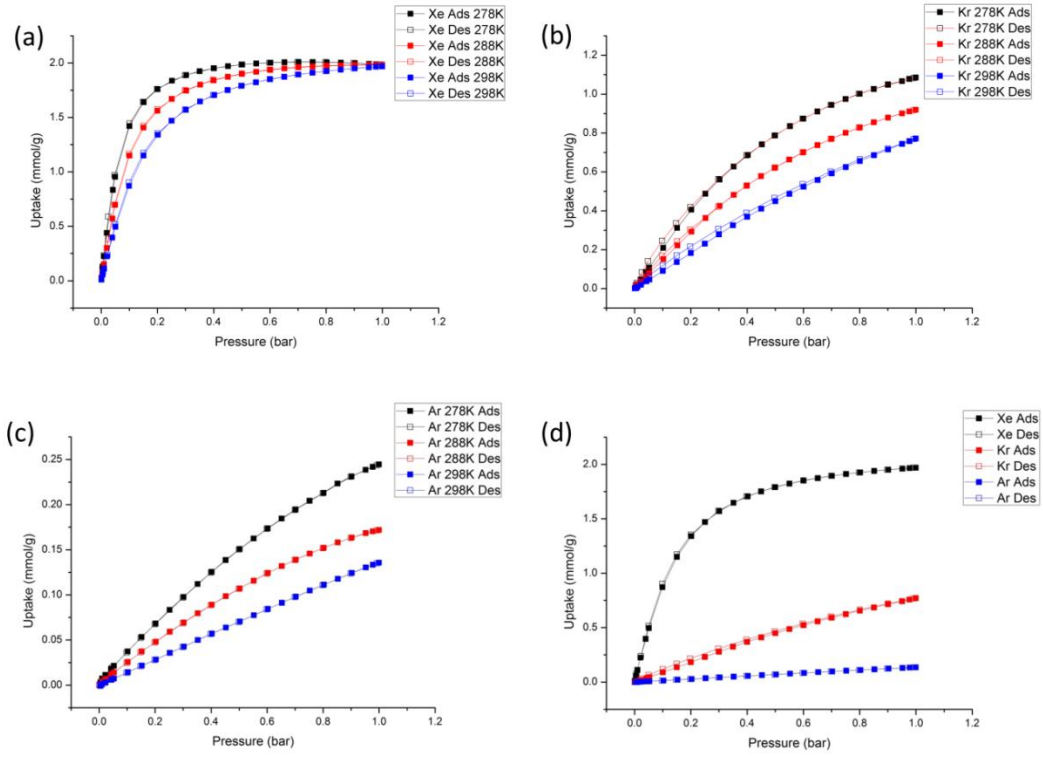

Figure 49. Single component adsorption-desorption isotherms of (a) Xe, (b) Kr, and (c) Ar at 278, 288, and 298 K. (d) comparison of Xe, Kr, and Ar sorption isotherm at 298 K.

In contrast, Kr and Ar show very different sorption behavior compared to Xe, with their sorption isotherms almost linear over the entire pressure range (Figure 49b/c). In both cases, the adsorbed amount is very different at different temperatures, suggesting the adsorption is incommensurate. Noticeably, the uptake amount of Kr and Ar are much less than that of Xe (Figure 49d).

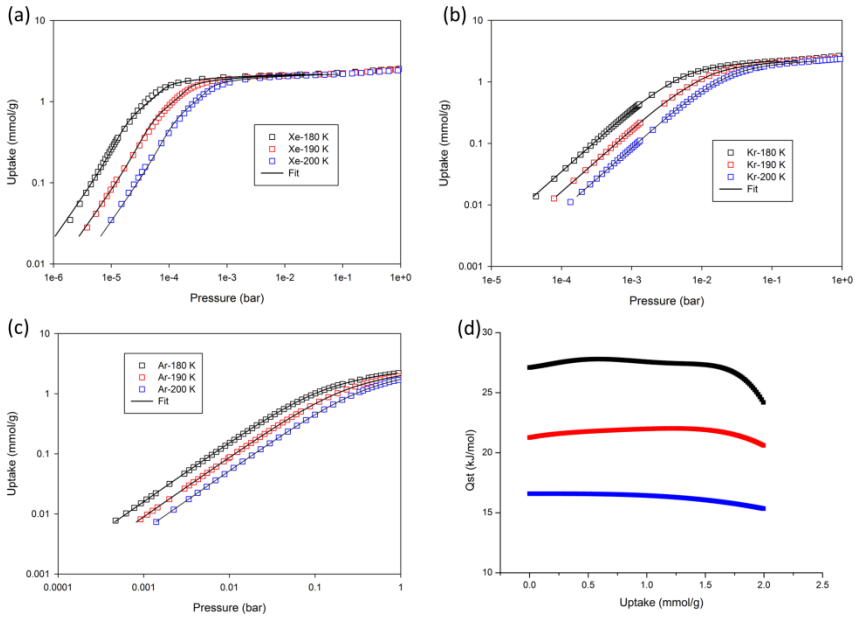

Figure 50. Single component adsorption isotherms of (a) Xe, (b) Kr, and (c) Ar at 180, 190, and 200 K. (d) Isosteric heat of adsorption for Xe (black), Kr (red) and Ar (blue).

Adsorption isotherms of Xe, Kr, and Ar were also collected at cryogenic temperatures (180, 190, and 200 K, Figure 50). As shown in Figure 50a, the commensurate adsorption of Xe is manifested ever more strongly at low temperatures. Clearly, each zig of zag segment of the channel in CoFA hosts one Xe atom, independent of temperature. We calculated the isosteric heat of adsorption (Q_{st}), which reflects adsorbent-adsorbate interaction energy, for all three gases to understand their distinct adsorption behaviors. As expected, the Q_{st} values follow the order of Xe > Kr > Ar. This is not surprising as the polarizability of the gases and, consequently, the Lennard-Jones force, both decrease in the same order. It is noteworthy that the Q_{st} maintains constant as a function of gas loading in all three cases, suggesting the energetically homogeneous character of the pore surface of CoFA. The uptake and selectivity for Xe/Kr separation performance on selected materials are summarized in Table 8.

Table 8. Xenon uptake and xenon/krypton selectivity at room temperature and 1 bar on selected adsorbent materials.

Material	BET surface area (m^2/g)	Xe uptake (mmol/g)	Q_{st} (Kj/mol)	Xe/Kr selectivity
MOF-5	3400	1.98 (298K)	15	-
MOF-74-Ni	950	4.2 (298K)	22	5~6[b] (298K)
MIL-53-Al	1300	~3.0 (298K)	-	-
Cu(HFIPBB)	58	~0.8 (298K)	~15	~2[d] (298K)
MFU-4l	3500	~ 1.8 (300K)	20	4.7[g] (310K)
HKUST-1	1710	~ 3.3 (300K)	26.9	8.4[g] (310K)
MOF-505	1030	~ 2.2 (300K)	-	~8[e] (298K)
$Co_3(HCOO)_6$[a]	300	~ 2 (298K)	28	~12[c]/6[f] (298K)

[a] This work, [b] The ratio of uptake or [g] Henry's constant based on single component isotherm, [c] from IAST calculation (Xe/Kr: 10/90), [d] from breakthrough experiment (Xe/Kr: 50/50), [e] from breakthrough experiment (Xe/Kr:20/80), [f] from breakthrough experiment (Xe/Kr:20/80).

3.4 IAST selectivity and breakthrough measurement

The observed differences in both uptake amount and adsorption affinity for Xe, Kr, and Ar suggest that CoFA has the potential for the separation of these gases. To assess its capability of selective adsorption under mixed gases conditions, we performed selectivity calculation with ideal adsorbed solution theory (IAST) and multicomponent column

breakthrough measurements. IAST is a thermodynamic method capable of predicting multicomponent adsorption equilibrium from the isotherms of single component gases.[69-73] It has been proven to be an effective method for various adsorbent materials.[74-76] Based on dual-site Langmuir–Freundlich fitting, the selectivity S for a binary mixture (Gas 1and Gas 2), is given the following equation, where X_i and Y_i denote the molar fractions of component i in the adsorbed and gas phases, respectively (i = Gas 1, Gas 2):

$$S=\frac{X_{Gas1}/X_{Gas2}}{Y_{Gas1}/Y_{Gas2}}$$

The Xe/Kr adsorption selectivity at room temperature for various compositions as a function of total pressure is plotted in Figure 51a. The Xe/Kr IAST selectivity is barely dependent on the composition. It has its highest value (~ 22) at very low pressure and decreases drastically as the pressure increases, reaching a plateau of ~12 at about 0.2 bar and remains relatively constant at higher pressure up to 1 bar. The steady selectivity of 12 represents the highest value reported to date among porous materials. We further studied the case of ternary mixture of equimolar Xe/Kr/Ar at room temperature. As shown in Figure 51b, clearly the MOF adsorbs Xe much more preferentially than Kr and Ar under mixed gases conditions.

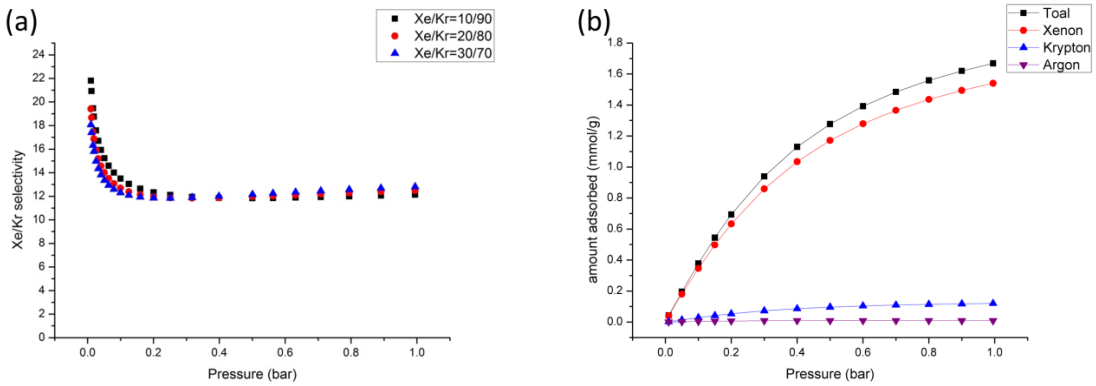

Figure 51. (a) calculated IAST selectivity for binary mixtures of Xe–Kr of varying compositions at 298 K. (b) simulated adsorption isotherms for a ternary mixture of Xe–Kr–Ar = 1 : 1 : 1 (298 K).

To evaluate the practical feasibility of using CoFA as a candidate for Xe/Kr separation under conditions that mimic a real-world situation, we conducted breakthrough experiments at room temperature on a binary gas mixture of Xe and Kr. In a typical breakthrough experiment, ~ 0.5 g of MOF sample was packed into a quarz column (5.8 mm I.D. × 150 mm long) with silica wool filled the void space. The sample was in situ activated in the column with a helium flow (10 mL/min) at 150 °C for 2 hours before the temperature was decreased to 25 °C. The flow of helium was then turned off while a gas mixture of Xe/Kr (90:10, v/v) at 10 mL/min was introduced into the column. The effluent from the column was monitored using a mass spectrometer (MS). The dead time was determined using the same column after adsorption saturation. Breakthrough times were calculated by subtracting the dead time from the observed breakthrough time. As shown in Figure 52, Kr was detected in the downstream shortly after the gas mixture was introduced into the column (152 s), while Xe was not detected until a breakthrough time of 463 s was reached. A Xe/Kr selectivity of 6 was calculated based on the adsorption capacity of the two gases, agreeable with the IAST selectivity derived from the single gas adsorption isotherms. These results indicate that CoFA exhibits high Xe/Kr selectivity not only at equilibrium, but also under kinetic conditions, suggesting that it is a promising candidate for Xe capture and separation from gas mixtures.

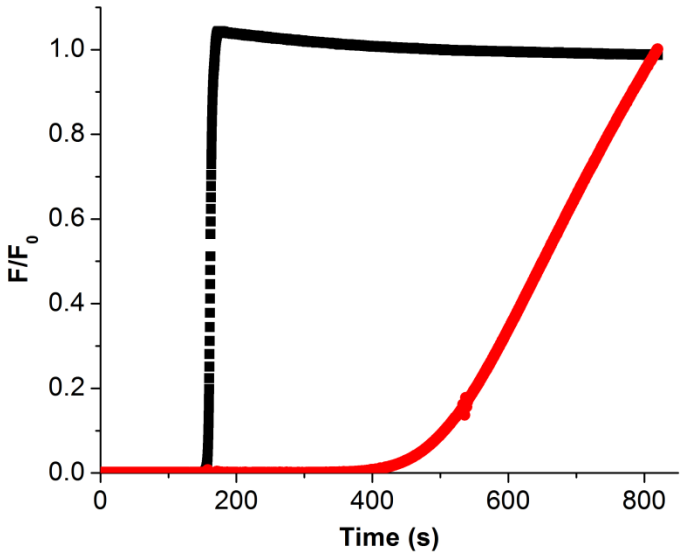

Figure 52. Column breakthrough result for Xe/Kr: 10/90 binary mixture at room temperature and a total pressure of 1 bar on CoFA. Black: Kr, Red: Xe.

3.5 Discussion and Conclusion

In this chapter, we have presented the separation of noble gases with a microporous MOF material.[77] Guided by calculation and molecular simulation, we focus on a known MOF structure, CoFA featuring one-dimensional channel with diameter slightly larger than the kinetic diameter of a Xe atom. Molecular simulation shows commensurate adsorption of Xe on CoFA where one Xe atom fits into each zig or zag segment of the channel while Kr atoms are randomly distributed in the channel with much less adsorbed amount. This has been confirmed by experimental results. Gas adsorption results show ~ 1 Xe atom per segment and the framework exhibit stronger interaction with Xe over Kr. Xe/Kr adsorption selectivity under mixed gases conditions was evaluated by IAST calculations and

multicomponent breakthrough experiments, which confirm the capability of CoFA for the separation of Xe and Kr mixtures.

4. Crystallizing atomic gas in a flexible microporous MOF and its unique temperature-dependent adsorption behaviors.

4.1 Introduction and background: gas adsorption on flexible MOFs

Among thousands of the MOF structures reported to date, most possess rigid networks and permit fully reversible guest adsorption and desorption; however, the others (roughly 0.5% of the total structures) exhibit markedly structural flexibility.[78-80] They are called flexible MOFs, i.e. they undergo structural transformation as response to external stimuli such as guest inclusion and removal. Flexible MOFs represent a unique type of materials which exhibit unexpected and often desirable properties for specific applications. For example, reversible structural transition of a MOF between 'collapsed' and 'expanded' phases toward gas adsorption and desorption can maximize its deliverable capacity for gas storage.[81] However, structural flexibility adds more difficulty to understanding their interaction with adsorbed guests and their structural changes.

The dynamic structural behavior of flexible MOFs can occur through to name a few.[82] These structural transformations are usually accompanied by enormous changes in crystal lattice parameters and pore volumes which can be reflected by peak shift in powder X-ray diffraction patterns and stepped gas adsorption isotherms. Nevertheless their in-depth characterizations are challenging and remain underexplored. Studies on the dynamic behavior of flexible MOFs have been largely relied on indirect approaches such as gas adsorption, computational modeling, powder X-ray diffraction, and IR/Raman spectroscopy.[83-85] While these techniques can assist in understanding the structural transformation and the underlying host-guest interactions, they are usually not sufficient to offer a full presentation of the process. In contrast, single crystal X-ray diffraction

(SCXRD) represents the most straightforward and powerful technique for the characterization of host-guest interactions and any crystallographic phase transitions. For example, it offers direct visualization of guest adsorption sites in MOFs which is critical to the design of new, better performing materials for targeted applications.[86-88] However, single crystal X-ray diffraction analysis of guest included MOF structures is demanding. It requires the guest molecules to be strongly adsorbed (trapped) and arranged in order so that they can be crystallographically identified. In addition, it is critical that the host structure retains single crystallinity upon activation, guest loading and removal. This is particularly challenging for flexible MOFs since the microscopic changes in crystal lattice accompanied with structural transformation upon guest removal and adsorption often lead to macroscopic damage of single crystals. Thus studies on guest-framework interactions for flexible MOFs by single crystal X-ray diffraction analysis are much rarer and their underlying dynamic structural behaviors remain not well understood.

The reversible phase transition of flexible MOFs in response to guest adsorption and desorption, referred to as breathing or gate-opening, largely depends on guest species and its pressure. Whether structural breathing occurs or not and at what pressure it occurs are correlated with the guest molecules. And for a specific guest, the breathing process is governed by its pressure. We report here that temperature can play a critical role in structural breathing of a flexible MOF and thus regulate its gas adsorption behavior. We use atomic gas as a probe to explore the dynamic phase transition of a flexible MOF structure, $Mn(ina)_2$ (ina^- = isonicotinate). Xe and Kr have been selected as guest molecules since their capture and separation are of industrial importance and the adsorption process of atomic gases in MOFs remains underexplored. The temperature-dependent structural

breathing leads to a counterintuitive adsorption behavior that gas uptake goes through a maximum as a function of temperature and an intriguing reverse of Xe/Kr selectivity.

4.2 Structural breathing and crystallization of Xe in $Mn(ina)_2$

$Mn(ina)_2$ was synthesized solvothermally: A mixture of $Mn(NO_3)_2 \cdot 4H_2O$ (142 mg, 0.57 mmol) and isonicotinic acid (140 mg, 1.14 mmol) were dispersed in 18 mL 95% ethanol. The mixture was stirred at room temperature for 2 hours and then kept at 100 °C for 1 day. After cooling down to room temperature, block shaped crystals were harvested through vacuum filtration and washed with ethanol (60 % yield based on Mn metal). The as synthesized crystal has a formula of $Mn(ina)_2 \cdot 0.5H_2O$. It is built on manganese octahedra as primary building units, with each octahedron connected to two pyridyl nitrogen and four carboxylates from six different ina^- liners, forming the three-dimensional framework. The framework possesses one-dimensional channels along crystallographic a axis. It exhibits structural breathing upon suitable guest inclusion and exclusion, as suggested by the characteristic profiles of gas adsorption isotherms (Figure 53). $Mn(ina)_2$ represents a robust flexible MOF that can well retain its single crystallinity under repeatedly guest loading and removal which permits us to direct visualize its structural transformation by single crystal X-ray diffraction analysis.

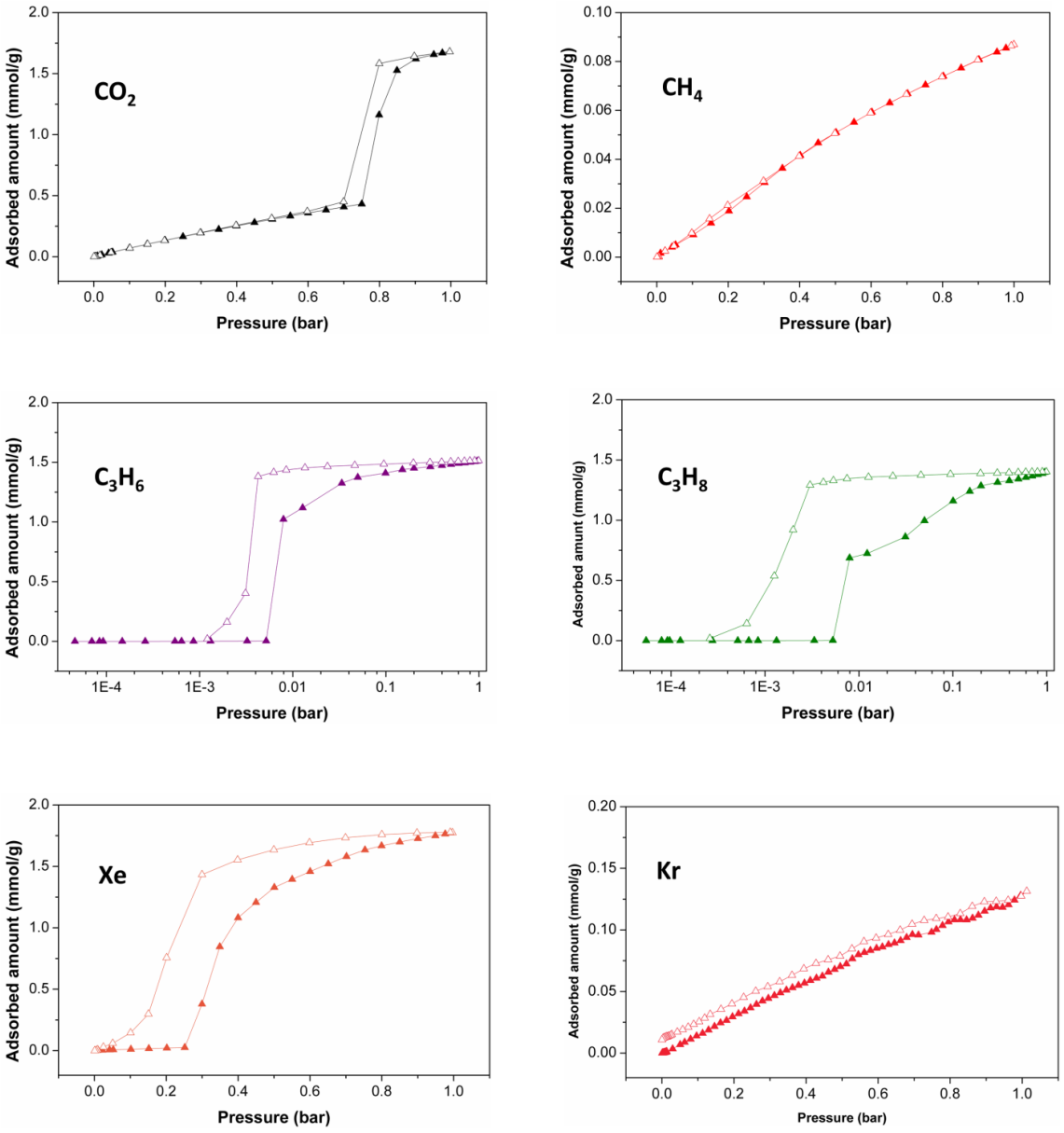

Figure 53. Adsorption isotherms of various gases on $Mn(ina)_2$ at room temperature.

As shown in Figure 54, In the as-synthesized structure of $Mn(ina)_2(EtOH)_{0.5}$, the open channels are not cylindrical but segmented comprising of repeating chambers and necks. They are decorated by pyridine rings and clearly the orientation of these aromatic rings influences the pore geometry. The chambers, where the initial solvent (ethanol) reside, are surrounded by four pyridine rings that are roughly parallel to the channel whereas the necks

are the regions composed of four pyridine rings that are approximately perpendicular to the channel. The necks have the smallest pore width of 2.0 Å, which is too narrow for ethanol molecules to fit in. Removal of the ethanol molecules by activating the as synthesized crystals at 120 °C under vacuum yields the activated phase, $Mn(ina)_2$. The activated compound crystallizes in space group *P21/c*, same as the as synthesized material and the overall connectivity of the original structure is retained. However, the activated form represents a new structure where the length of the crystallographic b-axis is approximately tripled compared to that of the as synthesized structure. Moreover, a structural transformation occurs upon guest removal involving rotation and rearrangement of pyridine rings, which leads to a dramatical change in pore geometry. In the activated structure, each channel segment is comprised of two pyridine rings perpendicular to the channels and the other two pyridine rings parallel to the channels. This closes up the chambers and results in shrinkage in pore size. The contracted channel is too small to accommodate large molecules such as propane, propene, or Xe, but can adsorb a moderate amount of smaller guests such as CO_2, CH_4 or Kr, as indicated by their adsorption isotherms.

By looking into the structure features of the as synthesized and activated compounds, we speculated that the guest-free structure must transform back to the original form in order to accommodate Xe atoms and the adsorbed Xe would likely reside at the chamber sites. To experimentally confirm our hypothesis, we attempt to structurally characterize Xe loaded compound ($Xe@Mn(ina)_2$) via single crystal X-ray diffraction analysis. After activating the as synthesized crystals under vacuum, the sample cell was filled by pure Xe gas to 1 bar and the crystals were kept under Xe atmosphere for sufficient time to reach

adsorption equilibrium. The crystals were subsequently subject to X-ray diffraction analysis. The crystal structure of Xe@Mn(ina)$_2$ adopts the same connectivity as the as synthesized one with similar segmented channels and alternating chambers and necks, confirming that the activated structure undergoes a structural transformation in order to accommodate Xe atoms into the channel. Apparently, the structural transformation involves the rotation and rearrangement of the pyridine rings as a result of the gas-framework interaction. The structure of Xe@Mn(ina)$_2$ appears to be more porous than the as synthesized Mn(ina)$_2$(EtOH)$_{0.5}$, as its calculated surface area (249 m^2/g) is larger than that of the latter (158 m^2/g). This indicates that the structural transformation is guest-dependent. As expected, Xe atoms reside at the chamber sites, leaving the necks unoccupied. Each chamber is able to accommodate two Xe atoms with a Xe-Xe distance of 4.08 Å. The simulated Xe adsorbed structure agrees well with the experimentally determined one in terms of both uptake amount and Xe adsorption sites. Physically adsorbed Xe atoms interact with the channel wall (hydrogen atoms and pyridine rings) through Van der Waals interactions (Figure 54 e-f).

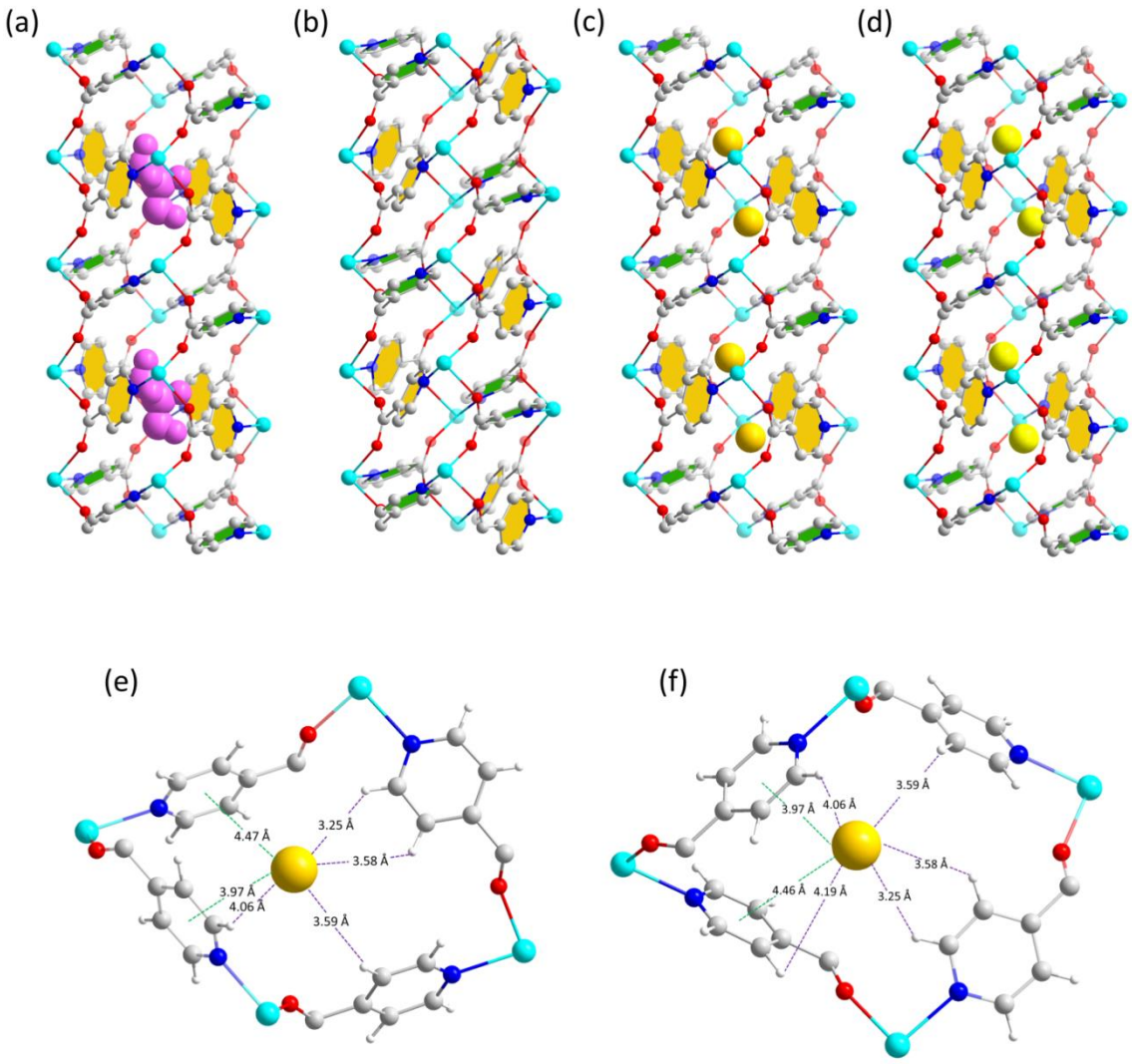

Figure 54. Cystallization of Xe in Mn(ina)2. Crystal structures of (a) as synthesized $Mn(ina)_2 \cdot 0.5EtOH$, (b) activated $Mn(ina)_2$, (c) simulated $Xe@Mn(ina)_2$ and (d) experimental $Xe@Mn(ina)_2$. (e) and (f) Xe adsorption sites in $Mn(ina)_2$. Color scheme: Mn (Cyan), O (red), N (blue), C (grey), H (white). Purple spacefill models represent ethanol and yellow/gold spheres represent Xe atoms. Green and orange colored hexagons represent pyridine rings that are roughly perpendicular and parallel to the channel, respectively.

4.3 Temperature-dependent Xe adsorption in $Mn(ina)_2$.

Xe adsorption isotherms collected at different temperature exhibit an abnormal yet very interesting phenomenon: The adsorption capacity of Xe goes through a maximum as a function of temperature. For a given temperature, there is essentially no Xe adsorption at

low pressure (before the structural change), indicating the pore size of the activated structure is too small for Xe atoms to fit in, as discussed earlier. When the applied pressure reaches a threshold, gate begins to open, where the adsorption isotherm shows a steep increase and then slowly levels out to a plateau up to 1 bar. The equilibrium uptake amount, however, follows a reversed order with respect to normal behavior of gas adsorption for all isotherms collected at and below 298 K. Above 298 K, the normal adsorption behavior is observe. Therefore, Xe uptake reaches a maximum at 298 K as temperature increases from 200 to 338 K. Also noted is the increase of gate-opening pressure as a function of increasing temperature, which is observed at all temperature studied (200 – 338 K). This observation is not unusual and is a common phenomenon for flexible MOFs. As generally recognized, gate-opening is a result of gas-framework interaction and, at lower temperature there would be more Xe atoms interacting with the framework so that a lower pressure is needed to induce the gate-opening.

Based on these observations we thus propose a temperature-dependent breathing mechanism. At lower temperatures ($T < 298$ K), Xe-framework interactions are sufficiently high to push the gate partially open to accommodate some gases into the pore, but the gate-opening is not complete. The extent of gate-opening is temperature dependent and as temperature increases, the gate is further opened so that more gases are adsorbed. The gate is fully opened when temperature reaches 298 K, giving rise to a maximum uptake at this temperature. At higher temperatures ($T > 298$ K), the adsorption behavior reverses back to normal (namely uptake amount decreases as temperature increases) since the pore space remains constant. It is noteworthy that the dynamic structural breathing is a result of the

synergetic effect of gas adsorption and temperature. Temperature variation alone cannot induce the structural transformation.

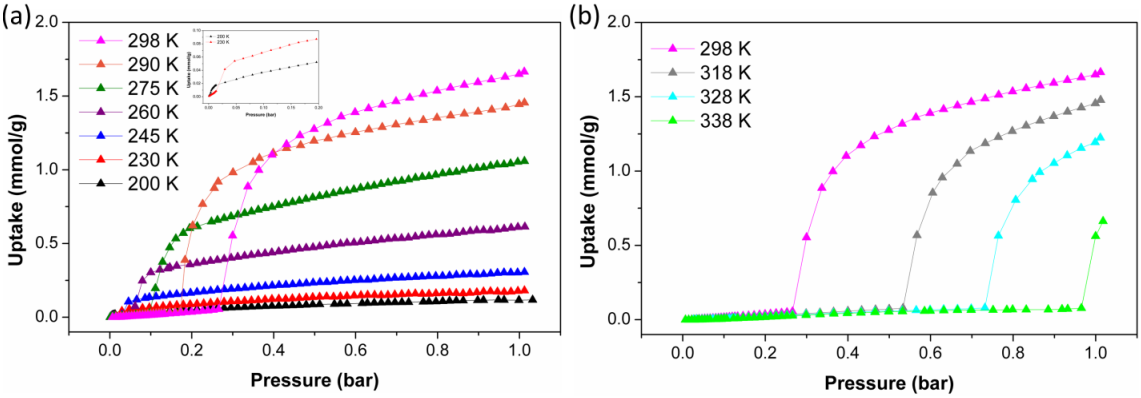

Figure 55. Xe adsorption isotherms at different temperatures on Mn(ina)2. (a) Xe adsorption isotherms at 200 – 298 K. Insert: isotherms at 200 K (black) and 230 K (red) at low pressure showing gate-opening. (b) Xe adsorption isotherms at 298 – 338 K.

4.4 Temperature-dependent reverse of Xe/Kr selectivity

We have also investigated the adsorption of Kr since the capture and separation of Xe and Kr represents a challenging task in industry. The adsorption isotherm of Kr at room temperature is a straight line, with a relatively low uptake amount of 0.13 mmol/g at 1 bar. This is very different from the adsorption of Xe which shows negligible adsorption at low pressure but undergoes a steep increase at ~ 0.25 bar and then gradually reaches a plateau up to 1 bar where ~ 1.7 mmol/g Xe is adsorbed. This observation suggests that Kr is not capable of inducing a gate-opening of the framework at room temperature and pressure up to 1 bar. However, we speculated that gate-opening will eventually occur if the pressure continues to increase or temperature decreases. High pressure adsorption measurements at room temperature indeed confirm our hypothesis and gate-opening for Kr takes place at ~3

bar (Figure 56). Kr adsorption isotherms at low temperatures also reveal a temperature-dependent adsorption which goes through an uptake maximum at 245 K, in a similar manner to that of Xe.

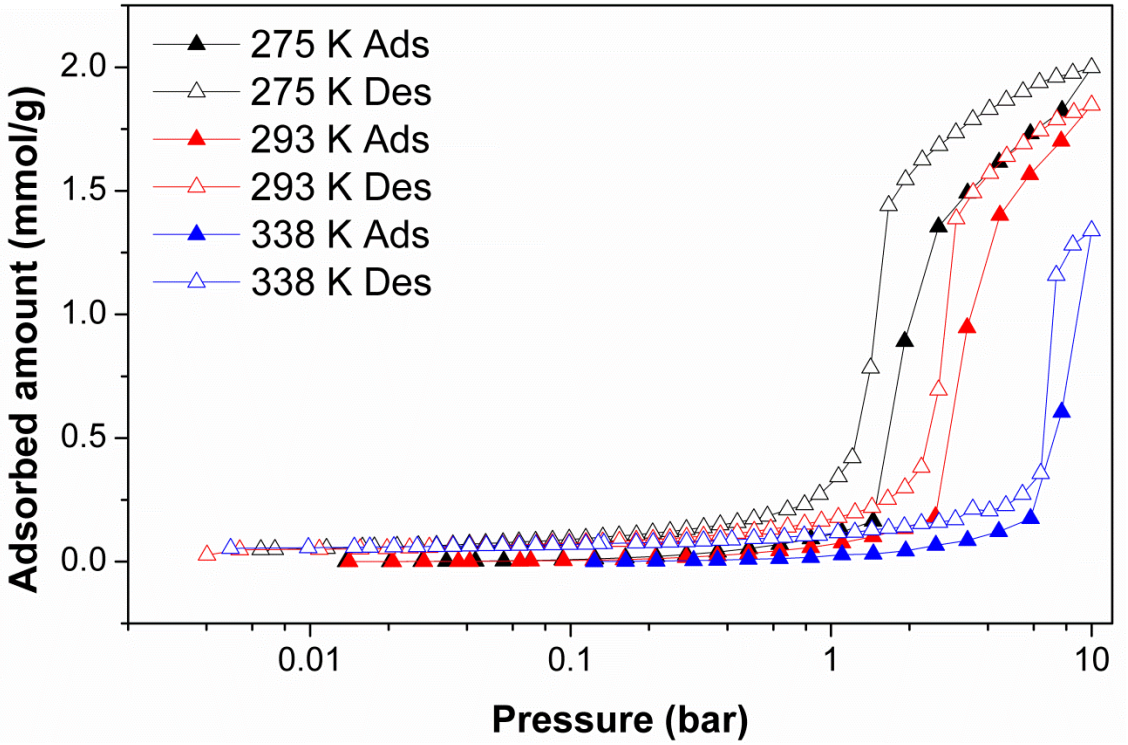

Figure 56. High pressure Kr adsorption isotherms at various temperatures.

Temperature-dependent structural transformation of $Mn(ina)_2$ leads to its unique adsorption behavior toward Xe and Kr, which results in intriguing temperature-dependent Xe/Kr adsorption selectivity, as shown in Figure 57. It is Xe selective at high temperatures ($T > 260$ K) whereas at lower temperatures ($T < 260$ K) it preferentially adsorbs Kr. At $T > 260$ K, Kr is not able to induce gate-opening at pressure up to 1 bar and thus the adsorbed amount is negligible. In contrast, due to the stronger interaction of Xe with the framework, it triggers gate-opening at a relatively low pressure thus a large amount of Xe are adsorbed

at 1 bar. Therefore in this temperature range the material shows a high Xe/Kr selectivity. This is not unexpected considering the differences in the atomic size (kinetic diameter: 4.05 vs 3.65 Å) and polarizability (40.4 vs 24.8 $\times 10^{25}/cm^3$) of Xe and Kr. Gate-opening is a response of the MOF framework to its interaction with guest molecules. The higher the interaction energy, the lower the force of a gas molecule will need to trigger the gate-opening. This has been commonly observed in the adsorption of many other gases on flexible MOFs. Higher adsorption affinity of Xe to the framework makes it easier to induce the gate-opening, resulting in a lower gate-opening pressure. To confirm this hypothesis, we calculated the adsorption enthalpies of Xe and Kr at the gate-opening inflection point. The results indicate the guest-induced structural transformation of $Mn(ina)_2$ follows a simple thermodynamic relationship between temperature and pressure of opening and the adsorption enthalpies for Xe and Kr are 26.5 and 17.9 kJ/mol, respectively, consistent with the aforementioned observations (Figure 58). The adsorption enthalpy of Xe is among the highest reported to date. The strong interaction between Xe atoms and the channel can be attributed to the tailored pore shape and size that fit favorably for Xe atoms. At low temperature ($T < 260$ K), gate-opening occurrs at relatively low pressure for both Xe and Kr. However, as the gate is only partially opened, Kr is preferably adsorbed due to its smaller atomic size and less diffusion restrictions. This is an interesting case since porous materials that are Kr selective have rarely been reported. Yet the phenomenon itself is not unexpected considering the fact that Xe is more polarizable thus it usually exhibits a stronger interaction with pore surface of materials that can adsorb both Xe and Kr.

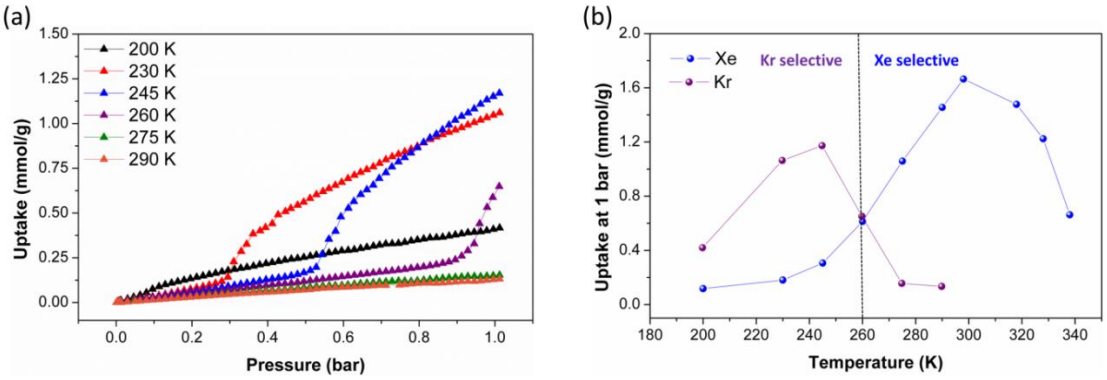

Figure 57. Reverse of Xe/Kr adsorption selectivity on Mn(ina)2. (a) Kr adsorption isotherm on Mn(ina)2 at 200 – 290 K. (b) Uptake amounts of Xe (blue) and Kr (purple) as a function of temperature at a fixed pressure (1 bar).

Table 9. Gate-opening pressure vs. temperature for Xe and Kr

Xe				Kr			
Temperature (T, K)	Gate-opening Pressure (P, mbar)	1/T (× 10^{-3})	lnP	Temperature (T, K)	Gate-opening Pressure (P, mbar)	1/T (× 10^{-3})	lnP
245	29.4	4.082	3.38	245	528	4.082	6.27
260	46.6	3.846	3.84	260	895	3.846	6.80
275	96	3.636	4.56	275	1450	3.636	7.28
290	172	3.448	5.15	293	2517	3.413	7.83
298	278	3.356	5.63	338	5832	2.959	8.67
318	507	3.145	6.23				
338	941	2.959	6.85				

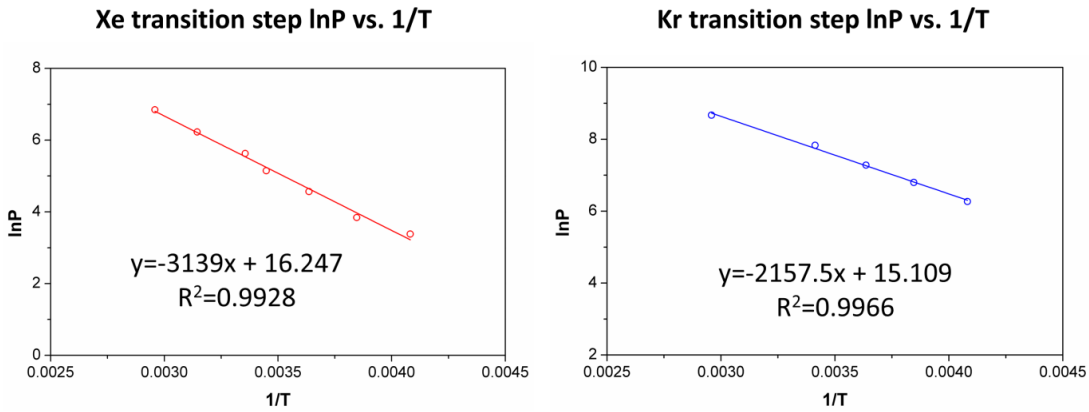

Figure 58. lnP vs. 1/T plot at transition step for Xe and Kr.

$$\Delta H = -R_g \partial \ln p / \partial (1/T)$$

ΔH (Xe) = 26.5 kJ/mol

ΔH (Kr) = 17.9 kJ/mol

4.5 Discussion and conclusion

We have used atomic gas xenon as a probe to investigate the structural transition of a flexible MOF, $Mn(ins)_2$ upon gas adsorption and desorption. The xenon loaded MOF structure has been revealed by single crystal X-ray diffraction. Adsorption of xenon at different temperatures on $Mn(ina)_2$ suggests an intriguing temperature-dependent adsorption which we believe is related to the temperature-dependent structural breathing of the MOF framework. The structural evidence by temperature variable *in situ* single crystal X-ray diffraction is ongoing. This temperature dependent structural response results in a reverse of Xe/Kr selectivity as a function of temperature.

5. Moisture triggered controlled release of a natural food preservative from a microporous MOF

5.1. Background and motivation

Food quality and safety are worldwide concerns that attract tremendous attention. Various food preservatives are used to keep food fresh. Compared to the extensively used synthetic ones, natural food preservatives are always preferred as they are more beneficial to our health.[88-90] For example, allyl isothiocyanate (AITC) is a major essential oil component found in plants from the Crucifera family, such as mustard, broccoli, and cabbage, which is widely used as natural food-flavoring and antimicrobial agents.[89,91,92] AITC can inhibit growth of a wide range of foodborne pathogens and spoilage-including microorganisms (including yeasts and molds) when used at low concentrations.[93,94] In addition, stronger antibacterial activity has been observed when it is in the vapor phase compared to the liquid phase. Despite its antimicrobial properties, the direct incorporation of AITC in food system is currently limited mainly because it is highly volatile and produces a pungent flavor at high concentrations.[95] To address this issue, controlled release of AITC from porous media has been proposed. In this strategy, AITC is first incorporated into a carrier material. Following well developed methods, AITC loaded carrier material can be packed within sachets and AITC will be released onto the food surface in a controlled manner upon external stimuli. This method is advantageous since there is no direct contact between food product and the carrier material or its component and it requires a smaller amount of AITC since it targets only the food surface where microbial contamination usually occurs instead of the entire food product. The key factor in this strategy is the performance of the carrier material. There have been a few studies using porous materials for the incorporation and

controlled release of AITC. For example, Park et al. showed that mesoporous silica SBA-15 can take up a large amount of AITC at room temperature.[96] Siahaan et al. tested Laminaria Japonica powder and mesoporous silica MCM-41 as AITC delivery vectors against bacteria and both materials were found to be capable of adsorbing and releasing AITC molecules, effectively delaying the growth of bacterial cells.[97] However, due to the relatively large pore size of these carrier materials tested and relatively weak adsorbate-adsorbent interaction, none of them can entrap AITC molecules resulting in a rapid loss of AITC without applying any external stimuli.

An ideal carrier material for the incorporation and controlled release of AITC should fulfill the following requirements: 1) it can take up a relatively large quantity of AITC and the loading process should be facile; 2) it is able to physically entrap and retain AITC molecules such that they will not desorb under normal conditions; and, most importantly, 3) the release of AITC from carrier material can be triggered by a select external stimulus and done in a controlled manner. Thus there is a pressing need to design suitable carrier materials for the incorporation and controlled release of AITC.

5.2. Material design, synthesis, and characterization

We propose to use MOFs as carrier materials due to its superior tunability in pore structure and its structure diversity. In this context, we focus our effort on a Zn based microporous MOF, $Zn_3(bpdc)_3(apy)$ or RPM6, for the following considerations. RPM6 is a three-dimensional, highly porous framework with a BET surface area of 609 m^2/g and a pore volume of 0.29 cm^3/g which provides enough void space for the accommodation of a modest amount of AITC. In addition, It features one-dimensional channels of ~ Å in diameter, slightly larger than the molecular size of AITC, which should have sufficient van

der Waals contacts with the adsorbate molecules. More importantly, this structure is water sensitive. It is stable under ambient conditions with low humidity. However, at high humidity, the structure tends to collapse and lose porosity.[97-99] This is especially desirable since it offers the possibility of stimulus induced controlled release.

5.2.1. Ligand and MOF synthesis

4,4'-azobispyridine (apy) was synthesized according to reported method with slight modifications. A solution of 4-aminopyridine (12 g, 0.128 mol) in DI water (240 mL) was added dropwise into a two-neck round bottom flask containing 1.6 L of sodium hypochlorite (14 wt% NaOCl aqueous solution, being chilled in ice-water bath and magnetically stirred) over a period of 1 hour. The mixture was stirred at 0 °C for another 30 minutes before the orange-colored precipitate was filtered and the filtrate extracted with chloroform (200 mL × 3). The extracted solution was dried over anhydrous sodium sulfate for 20 min and evaporated to let them dry with a rotary evaporator. Filtered precipitate and dried filtrate are combined and then recrystallized in DI water. The pure product was obtained as an orange solid (7.32 g, 64% yield based on 4-aminopyridine). ^{1}H NMR (300 MHz, $CDCl_3$): 7.75 (d, 4H, J = 6.2 Hz), 8.88 (d, 6H, J = 6.2 Hz).

RPM6 was prepared solvothermally by mixing $Zn(NO_3)_2 \cdot 6H_2O$ (0.1485 g, 0.5 mmol), apy (0.046 g, 0.25 mmol) and biphenyldicarboxylic acid (H_2bpdc, 0.121 g, 0.5 mmol) in 10 mL of DMF in a 20 mL glass vial. The mixture was sonicated for 5 minutes before being placed in a 100 °C oven. The reaction was heated for 20 hours and then cooled down naturally to room temperature. The reddish crystals were filtered and washed with DMF and dried in air (yield: 94.2%).

5.2.2. Crystal structure determination

Single crystal X-ray diffraction analysis on the crystal of RPM6 reveals that it crystallizes in the monoclinic space group *P2₁/c* (Table 10). In this structure, each asymmetric unit contains two crystallographically independent zinc centers which are five and six coordinated, respectively. Three zinc centers and six carboxylate groups from the $bpdc^{2-}$ ligands form the trinuclear secondary building unit (SBU) $Zn_3(\mu_2\text{-}OCO)_2(COO)_4$. Each Zn_3 SBU is connected to six adjacent SBUs through $bpdc^{2-}$ linkers, resulting in a two-dimensional layer parallel to the *bc* plane. The 2D layers are further pillared by apy ligands to generate a three-dimensional network. Two identical networks interpenetrate to yield the final framework of RPM6, which contains one dimensional cylindrical channels of 7 × 20 Å.

Table 10. Single crystal data for RPM6.

Compound	$[Zn_3(bpdc)_3(apy)]\cdot 6DMF$
Formula	$C_{70}H_{76}N_{10}O_{18}Zn_3$
M	1024.58
Crystal system	Monoclinic
Space group	$P2_1/c$
a, Å	19.698(2)
b, Å	13.800(1)
c, Å	26.288(3)
α, °	90.00
β, °	96.244(2)
γ, °	90.00

V, $Å^3$	7103.54
Z	4
Temperature, K	100(2)
λ(Mo Kα), Å	0.71073
D, g/cm^3	1.154
Reflections collected	59805
R1[a] [I > 2σ(I)]	0.0644
wR2[b] [I > 2σ(I)]	0.2006
Goodness-of-fit	1.017
CCDC number	979464

[a]$R1 = \sum \left| Fo - Fc \right| / \sum \left| Fo \right|$

[b]$wR2 = \sum [w(Fo2 - Fc2)2] / w(Fo2)2]1/2$

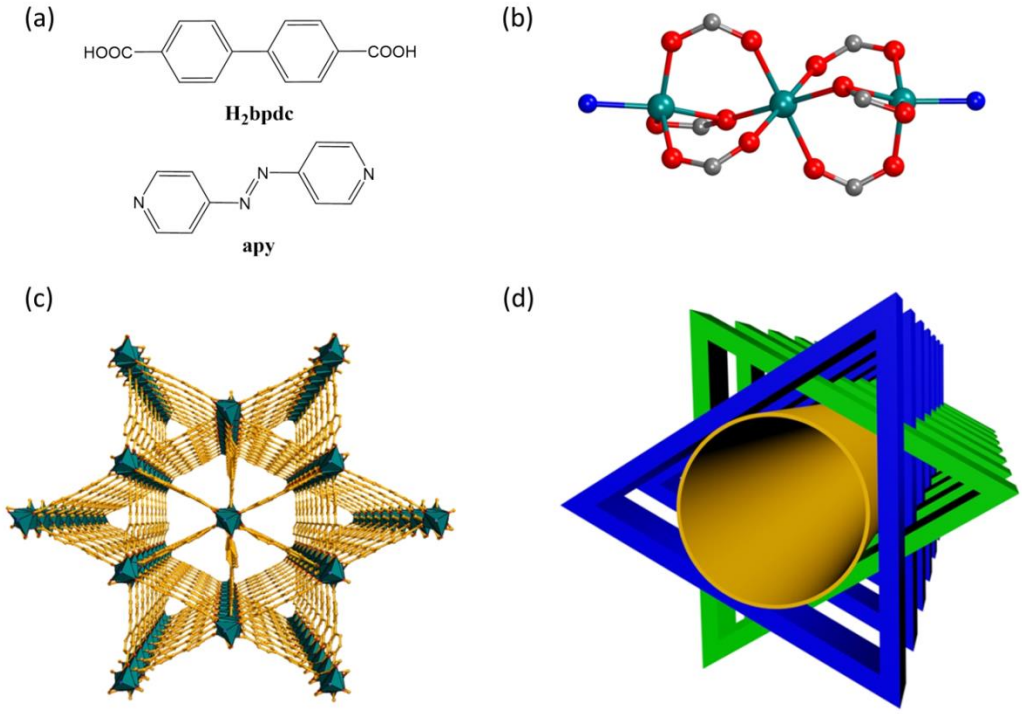

Figure 59. (a) Organic ligands used in RPM6, (b) $Zn_3(\mu_2\text{-}OCO)_2(COO)_4N_2$ SBU. (c) Perspective view of a single 3D net, (d) The two-fold interpenetrated nets and the 1D channel.

5.2.3. Powder X-ray diffraction and thermogravimetric analysis

Phase purity of RPM6 has been confirmed by powder X-ray diffraction analysis (Figure 60). Thermogravimetric analysis (TGA) shows a weight loss of 23.56% before 150 °C, followed by a plateau up to 350 °C, indicating the framework possesses relatively high thermal stability.

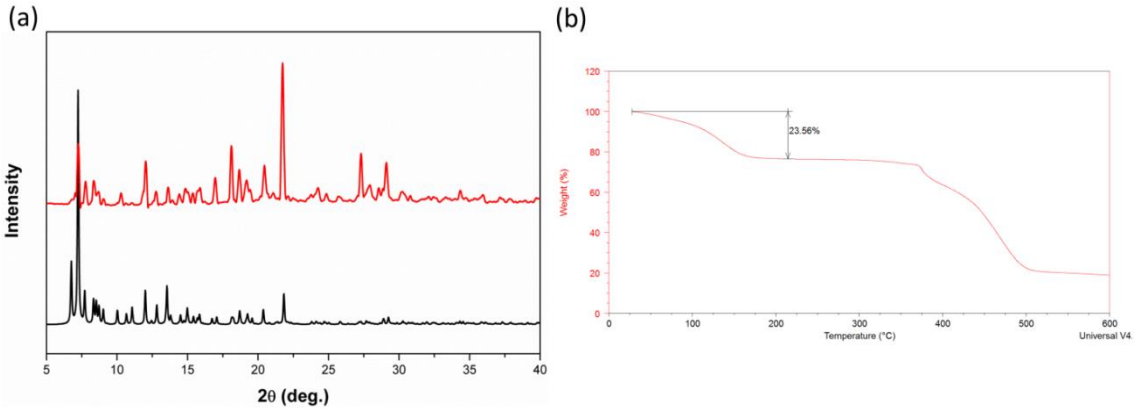

Figure 60. (a) PXRD patterns of RPM6, bottom: simulated; top: as synthesized. (b) TGA curve of as synthesized RPM6.

5.3. AITC loading and its controlled release

Ar adsorption measurement at 87 K confirms the permanent porosity of RPM6, showing a BET surface area of 609 m^2/g and a pore volume of 0.29 cm^3/g. The pore size distribution curve agrees well with the pore size measured from crystal structure with a peak centered at ~6 Å (Figure 61).

AITC loading onto the MOF was conducted with a homemade gravimetric adsorption analyzer modified from a TGA Q50 unit (TA instruments). The sample was first activated at 180 °C under N_2 to remove any residual solvent. After cooling down to room temperature, pure N_2 flow was switched to another N_2 flow passing through an AITC bubbler. Sample weight was recorded over the experiment time period. Desorption was carried out by switch the gas flow back to pure N_2 flow. As shown in Figure 62, RPM6 can take up as much as 27.3% w/w AITC at room temperature. Notably, more than 90% of the adsorbed AITC was retained in the pores even after 10 hours of flushing by pure N_2. The negligible desorption may come from surface adsorbed AITC. This suggests RPM6 can effectively entrap AITC molecules at room temperature.

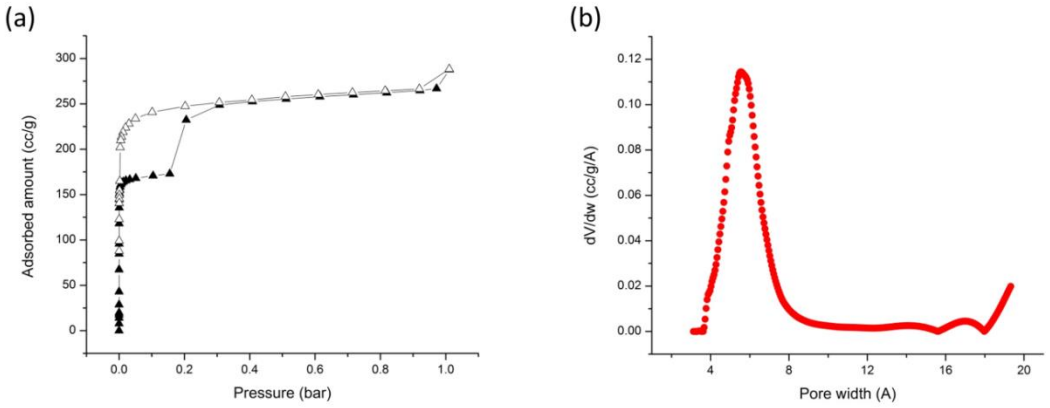

Figure 61. Porosity characterization of RPM6. (a) Ar adsorption-desorption isotherm at 87 K. (b) Pore size distribution curve.

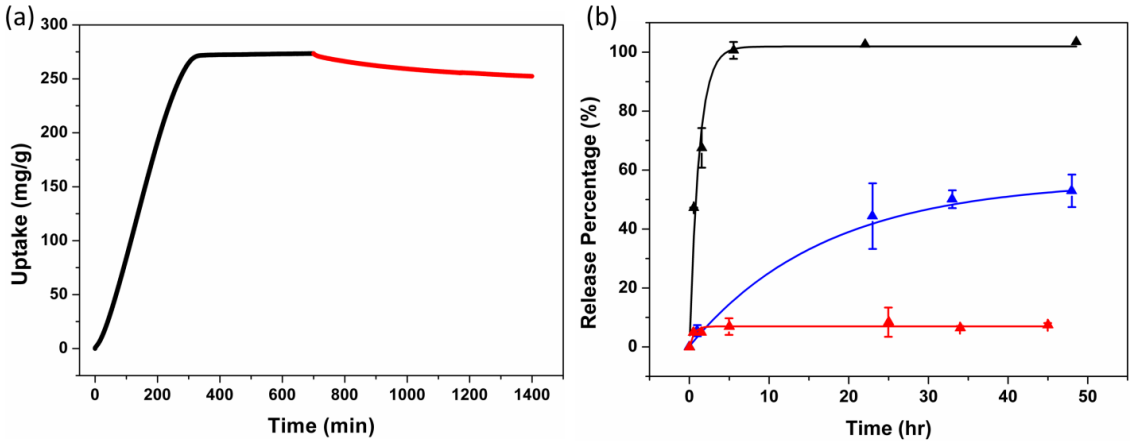

Figure 62. (a) AITC adsorption (black) and desorption (red) curve on RPM6 at room temperature (b) Release profiles of pure AITC under room humidity (black), AITC loaded RPM6 at room humidity (red) and at 100% relative humidity (blue).

Based on these findings and the face that the MOF framework breaks down upon exposure to water, we further evaluated the controlled release of AITC from RPM6 under elevated humidity. The controlled release experiment was first performed under room humidity (30% < RH% < 35%). AITC was loaded onto RPM6 using the above mentioned method to obtain AITC loaded RPM6 (AITC@RPM6). ~ 50 mg AITC@RPM6 was added to a 250 mL glass

jar and sealed properly. The glass jar was maintained at room temperature (25 ± 1 °C) and room humidity to mimic regular conditions for food storage. The headspace samples (0.5 mL) were taken on a timely manner to measure AITC concentration changes in the gaseous phase. As shown in Figure 62b red curve, The AITC concentration in the headspace remained constant throughout the experimental period (~ 2 days) after an initial increase in the first few hours corresponding to ~ 10% of the loaded AITC. Again, this confirms that RPM6 can entrap AITC in its pore space at room temperature and room humidity. This is significant, as encapsulation of AITC has so far not been achieved by any other porous carrier materials. To test the effectiveness of using moisture as an external stimulus for triggering the release of AITC from AITC@RPM6, in a parallel experiment, a relative humidity of 95-100% was generated in the glass jar to mimic the highly humid atmosphere within a package of fresh produce. The obtained release profile (Figure 62b blue curve) shows that AITC was gradually released the headspace and reached a release level of ~55% of the total adsorbed AITC after ~2 days of the experimental period in two consecutive phases. The early moderately high release of gaseous AITC molecules within the first 10–20 hours generates a rapidly lethal dose or concentration of AITC that inhibits the growth of selected food-borne pathogens, while the extended slow release of AITC during the second phase can distinctly reduce the remaining viable counts of these harmful microorganisms.[98,100,101] Thus the release performance in this work makes RPM6 an excellent carrier material of AITC for food safety applications. Evaporation of the pure AITC sample (without MOF) was also carried out as a control experiment. A total release of AITC was completed in less than 2 hours (Figure 62b, black curve). All release measurements were carried out multiple times and the results were consistent. These results

confirm that RPM6 represents an excellent encapsulant and releasing agent that is not only capable of effectively entrapping and retaining AITC within its pores but can also be triggered to start the controlled and slow release of AITC when exposed to an atmosphere of high moisture content. Moisture is a readily achievable external stimulus which is particularly desirable for the controlled release of food packaging materials as the process is simple, natural, and nontoxic.

5.4. Controlled release mechanism study

The underlying mechanism of controlled release of AITC from RPM6 triggered by moisture is related to the structural transformation of the MOF upon exposure to a high concentration of water vapor. Due to the poor water stability of the Zn-N bonds, when humidity is sufficiently high, the water molecules gradually replace the apy pillars by forming stronger Zn-O bonds. This results in a structural transformation from the three-dimensional framework of RPM6 to a nonporous one-dimensional Zn(bpdc)(H_2O)$_2$ chain compound. In order to confirm this hypothesis, we performed powder X-ray diffraction (PXRD) analysis on the sample after controlled release experiments. The PXRD pattern of the sample after release study matches very well with that of the one-dimensional compound.

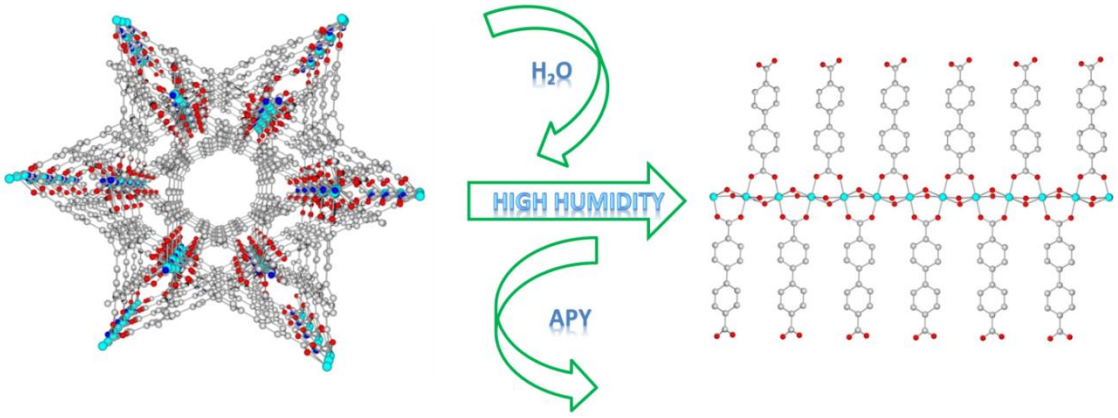

Figure 63. Proposed mechanism of controlled release of AITC from RPM6 under high humidity (teal: Zn, red: O, blue: N, grey: C, white: H).

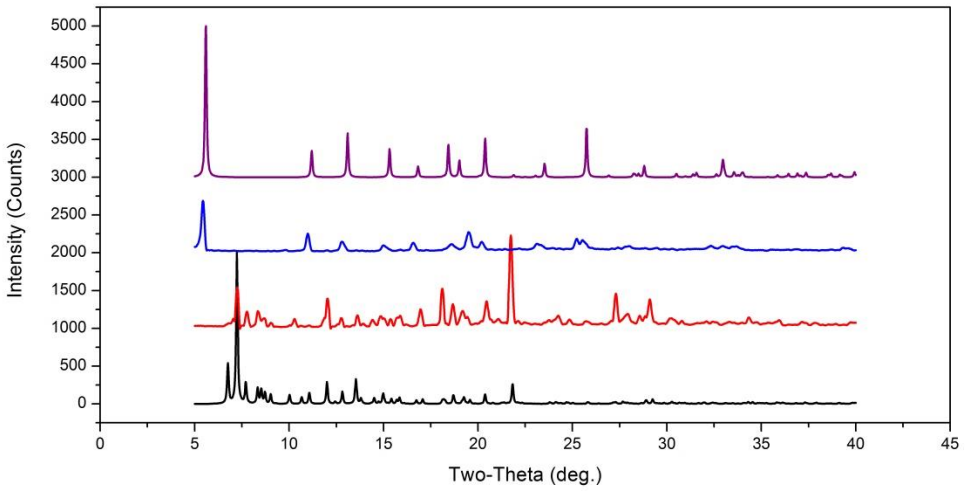

Figure 64. PXRD patterns from bottom to top: simulated (black) and as synthesized (red) RPM6, simulated (blue) and as synthesized (purple) Zn(bpdc)(H_2O)$_2$.

In order to further explore the correlation of the structural transformation to humidity, we studied the structural change under different humidity levels as a function of time. As shown in Figure 65, the structural transformation is closely related to the relative humidity, indicating the controlled release of AITC from RPM6 can be triggered in a fully controlled manner.

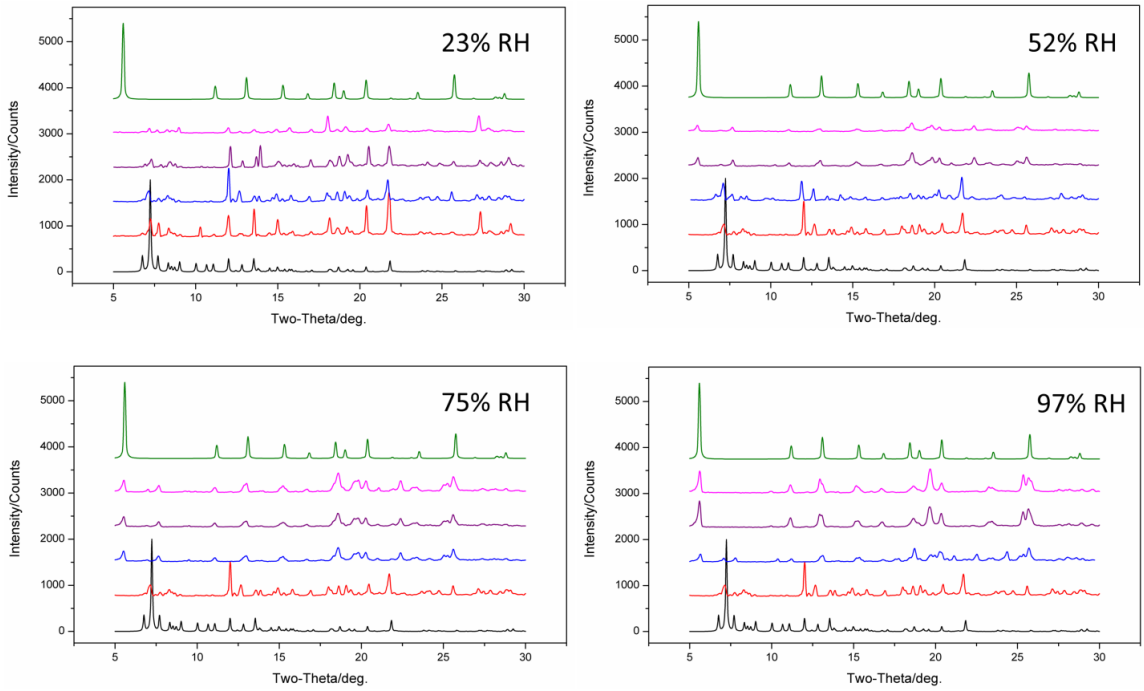

Figure 65. PXRD patterns of RPM6 under various humidity conditions. From bottom to top: simulated (black), as synthesized (red), after exposure to humid air for 10 hours (blue), 3 days (purple), 5 days (magenta). The top one is the simulated pattern of $Zn(bpdc)(H_2O)_2$.

5.5. Discussion and conclusion

Compared to traditional porous solids, MOFs suffer from relatively poor moisture/water stability which has limited their potential for industrial applications. In this study, we take advantage of this shortcoming and apply it to food chemistry.[102] We use a porous, water sensitive MOF for the encapsulation and controlled release of AITC, a widely used natural food preservative. This material takes up a large amount of AITC at room temperature and the adsorbed AITC molecules were trapped inside the pores under room humidity. However, at elevated humidity level, the adsorbed AITC molecules are gradually released due to the structural collapse of the MOF framework. Our result shows the MOF can serve

as an excellent carrier material for AITC and its controlled release with an simple, natural, and nontoxic external stimulus.

6. Highlight of other work

6.1 Temperature dependent selective molecular sieving of alkane isomers

Here we show a calcium based microporous MOF, Ca-TCPB, which shows temperature dependent selective molecular sieving of alkane isomers. This is significant as separation of three components through selective molecular sieving was never achieved for traditional materials. Due to the slight flexible nature of Ca-TCPB framework we found the structure respond differently toward different adsorbates at different temperature, which thus render it complete separation between these components.

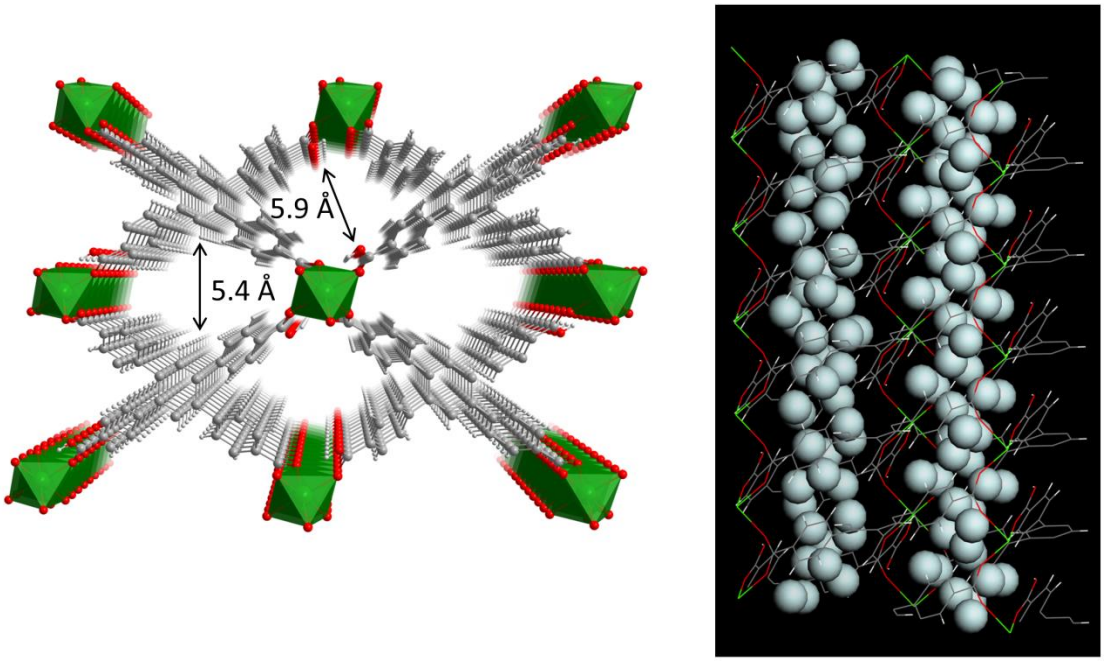

Figure 66. Structure of Ca-TCPB and its channel depicted by helium simulation.

Ca-TCPB was synthesized according our previously reported procedure and the phase purity was confirmed by PXRD analysis.[103,104]

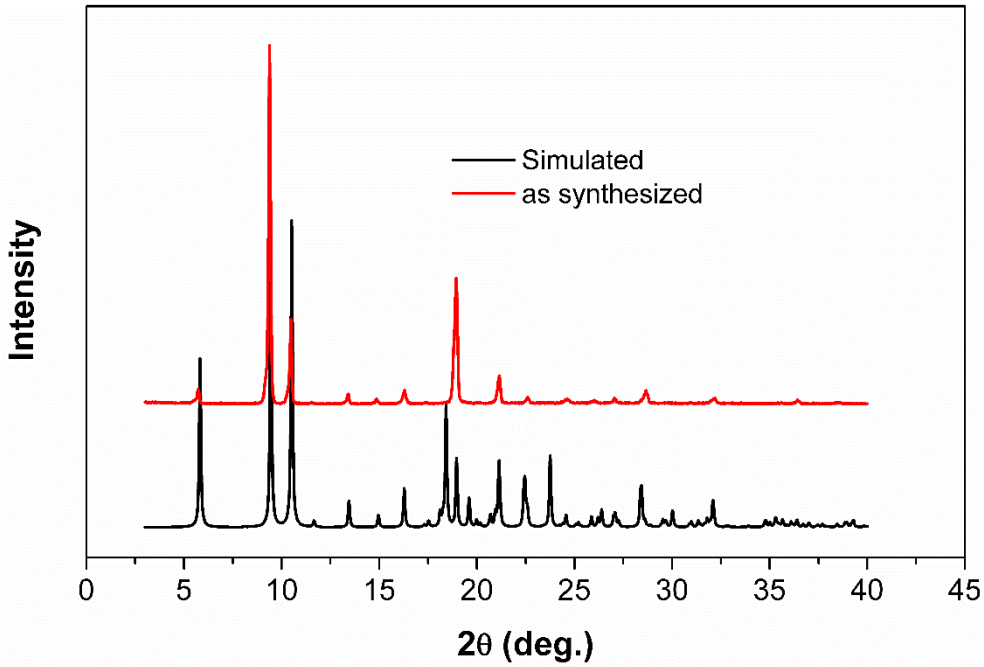

Figure 67. PXRD pattern of Ca-TCPB.

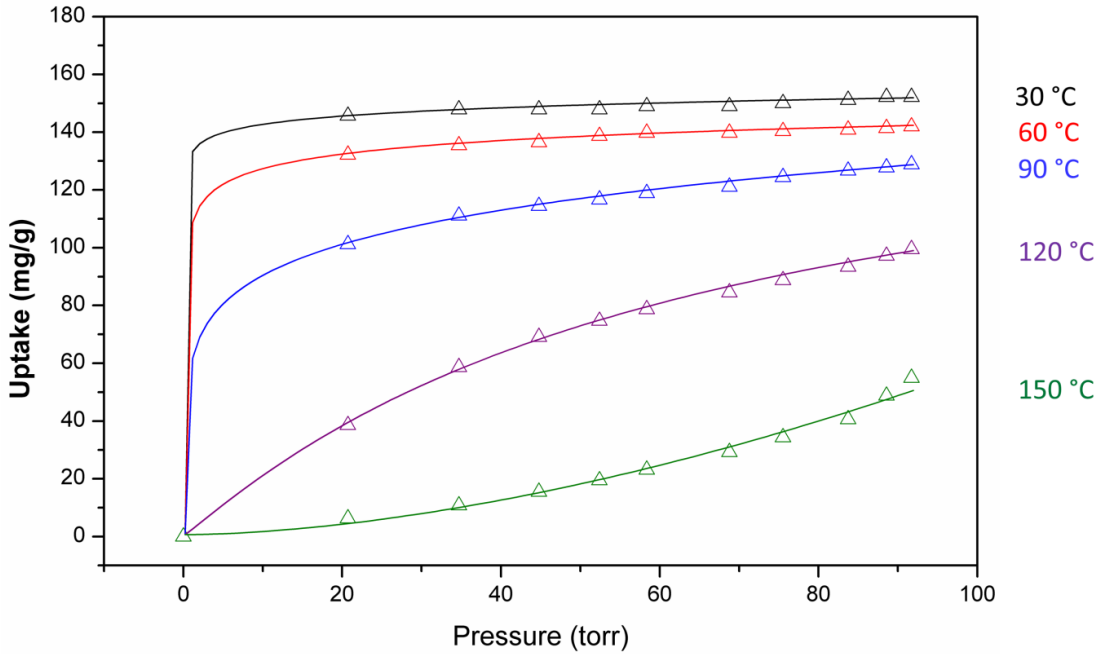

Figure 68. n-hexane adsorption isotherm on Ca-TCPB.

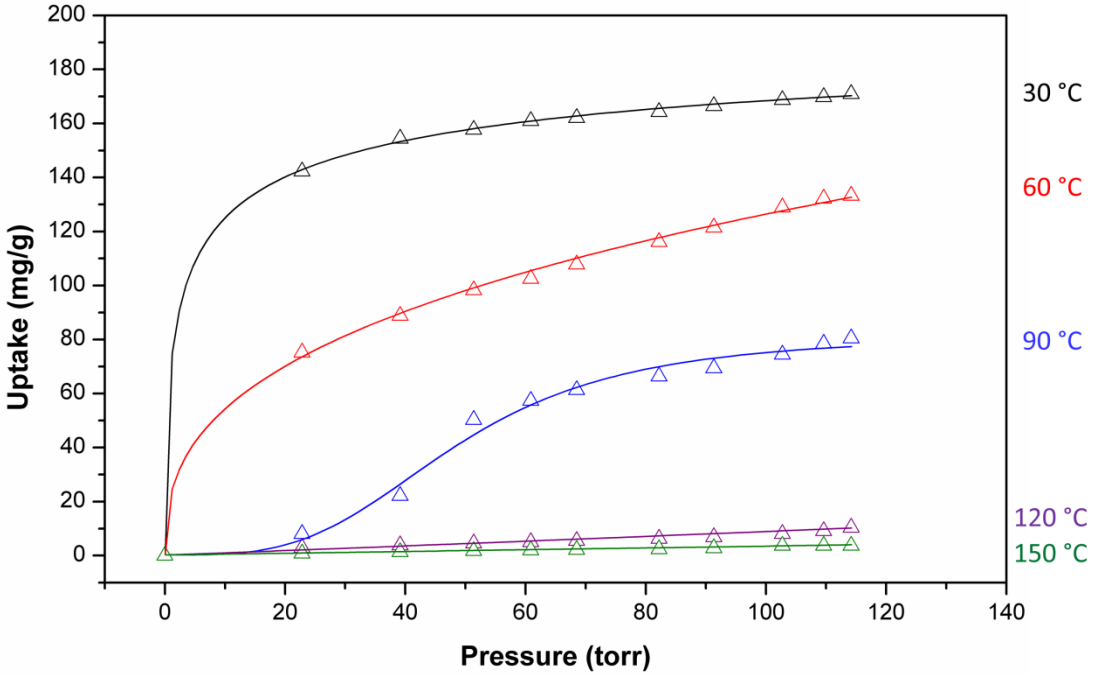

Figure 69. 3-methylpentane adsorption isotherm on Ca-TCPB.

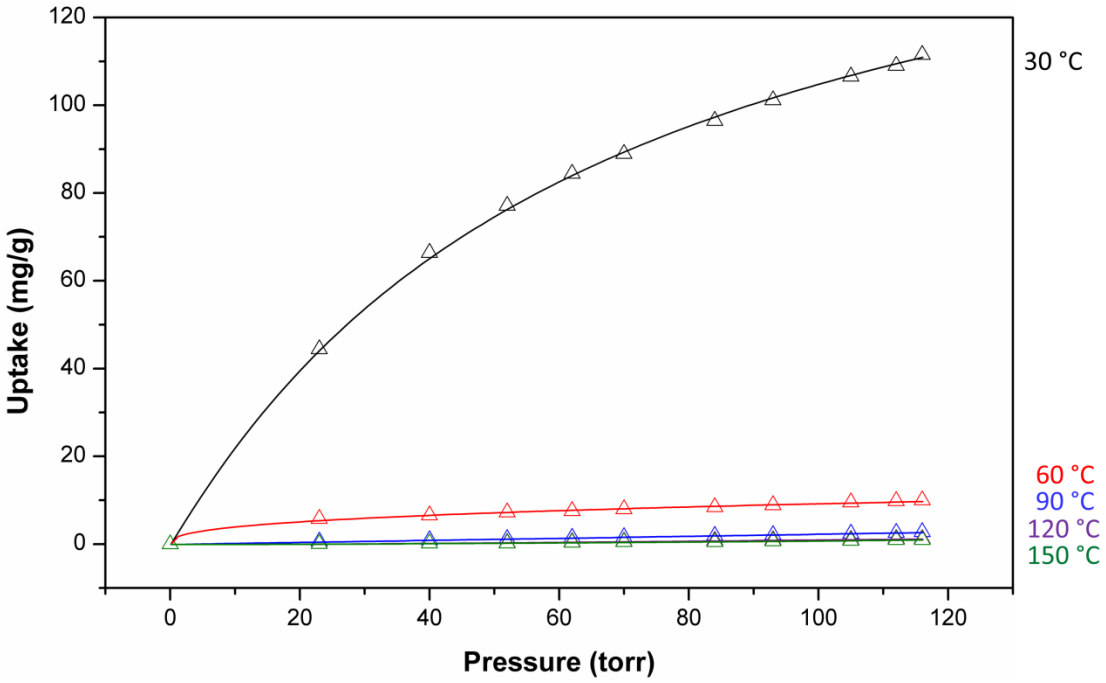

Figure 70. 2,2-dimethylbutane adsorption isotherm on Ca-TCPB.

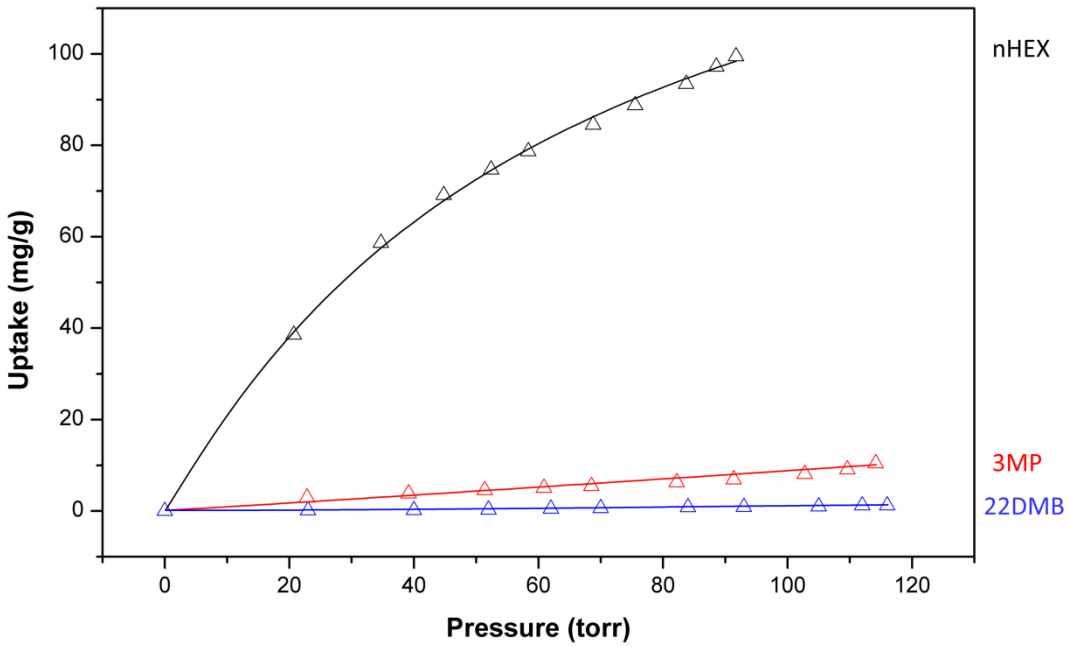

Figure 71. Comparison of adsorption isotherms at 120 °C for all three C6 alkane isomers.

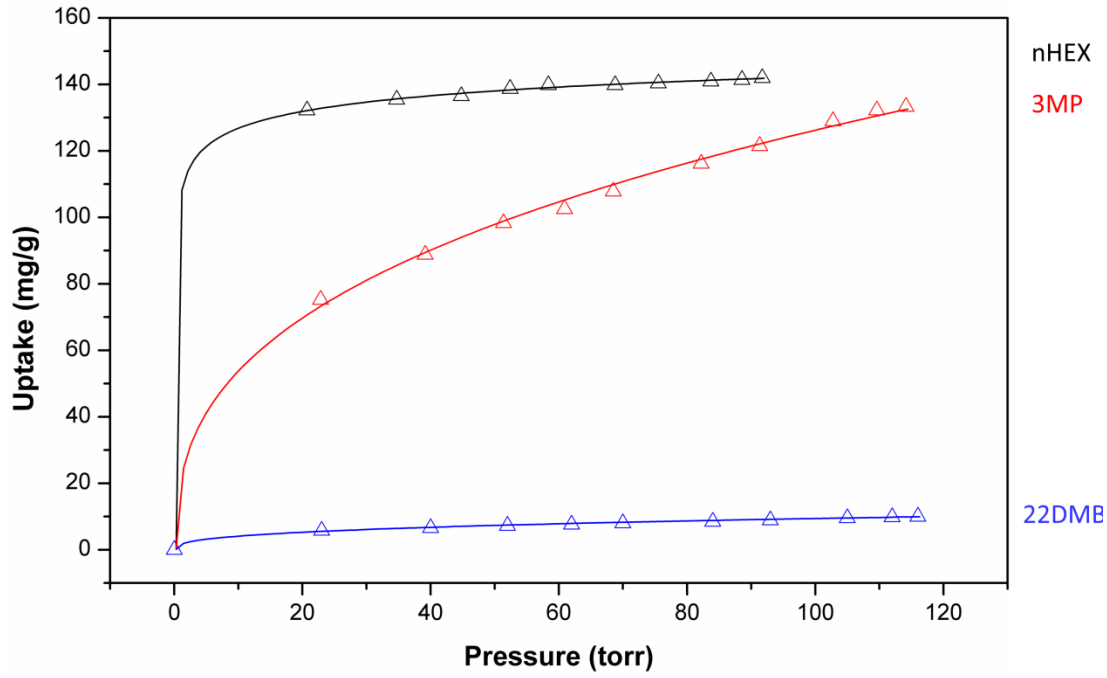

Figure 72. Comparison of adsorption isotherms at 60 °C for all three C6 alkane isomers.

Adsorption isomers of three C6 alkane isomers with different degree of branching (n-hexane, 3-methylpentane, and 2,2-dimethylbutane) were collected at different temperatures (30, 60, 90, 120, and 150 °C). As shown in Figure 68-70, the three isomers show very different adsorption profiles, especially their dependence on temperature. We believe this is due to the flexibility of the framework. That is, the structure has different response toward the adsorption of different isomers at different temperature. As a result, sweet spots can be found for complete separation of these isomers. As shown in Figure 71-72, at 120 °C, Ca-TCPB adsorbs only linear alkane but excludes both monobranched and dibranched isomers. In contrast, at 60 °C, it adsorbs both linear and monobranched C6 alkane but excludes 2,2-dimethylbutane. This makes it possible for complete separation of all three alkane isomers with one compound. We proposed the following flowchart for the separation process which involves two adsorption beds at 60 °C and 120 °C. This process will enable the production of pure products of each of the three isomers.

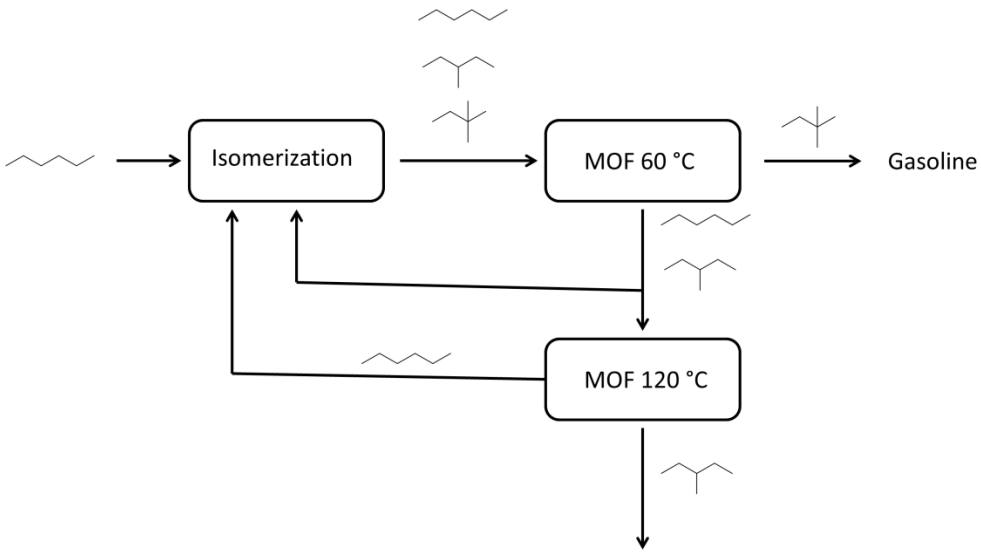

Figure 73. Schematic show of the proposed temperature dependent separation of C6 alkane isomers.

6.2 Highly porous and hydrophobic MOFs for chlorocarbon capture

Two highly porous UiO type MOFs have been designed and synthesized making use of reticular chemistry.[12,105] Fluorinated ligands were used in order to enhance the hydrophobicity of the material.

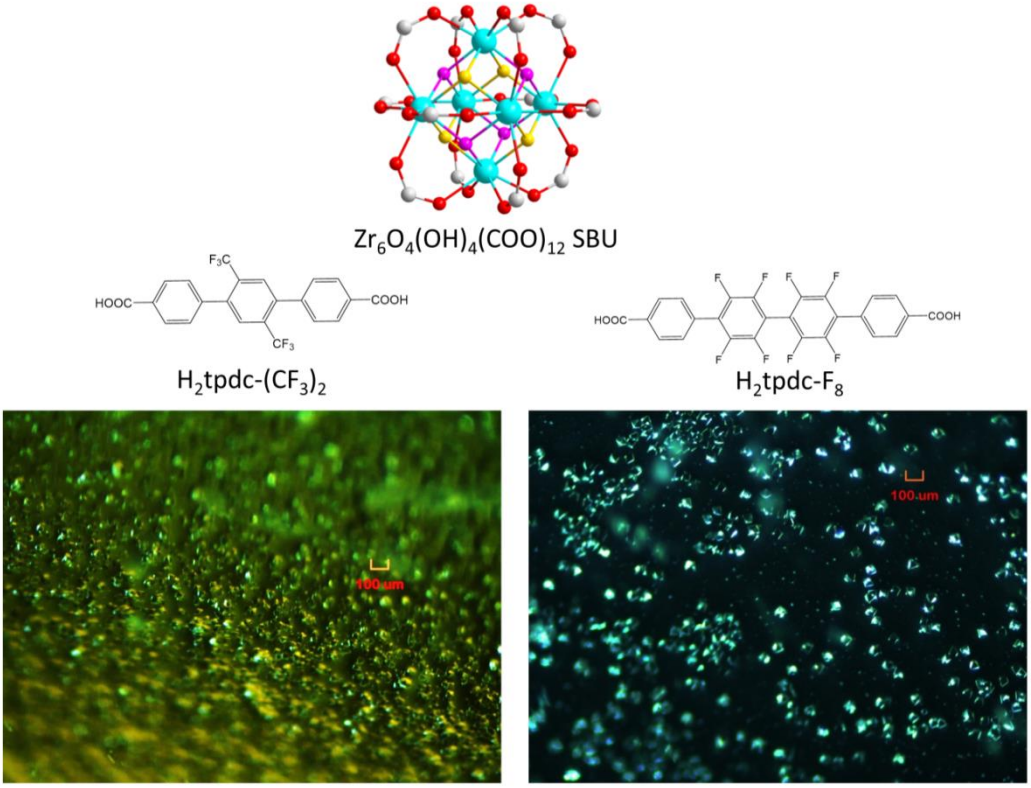

Figure 74. SBU, organic ligands, and crystal images.

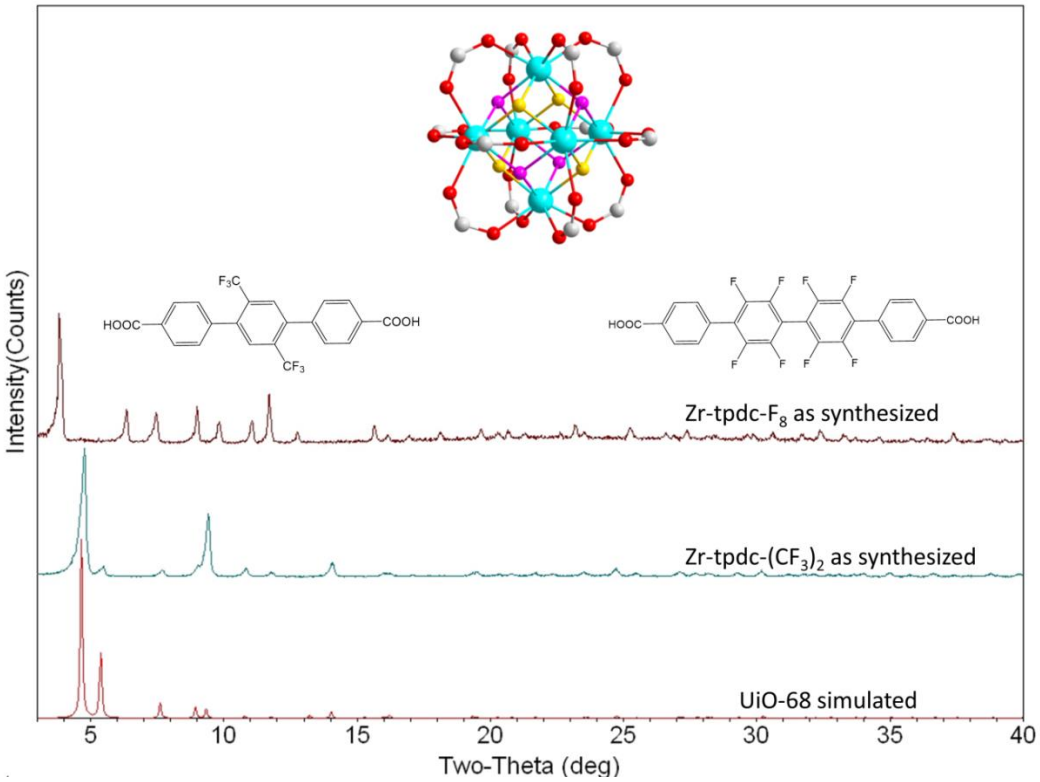

Figure 75. PXRD pattern of as synthesized Zr-tpdc-$(CF_3)_2$ and Zr-tpdc-F_8.

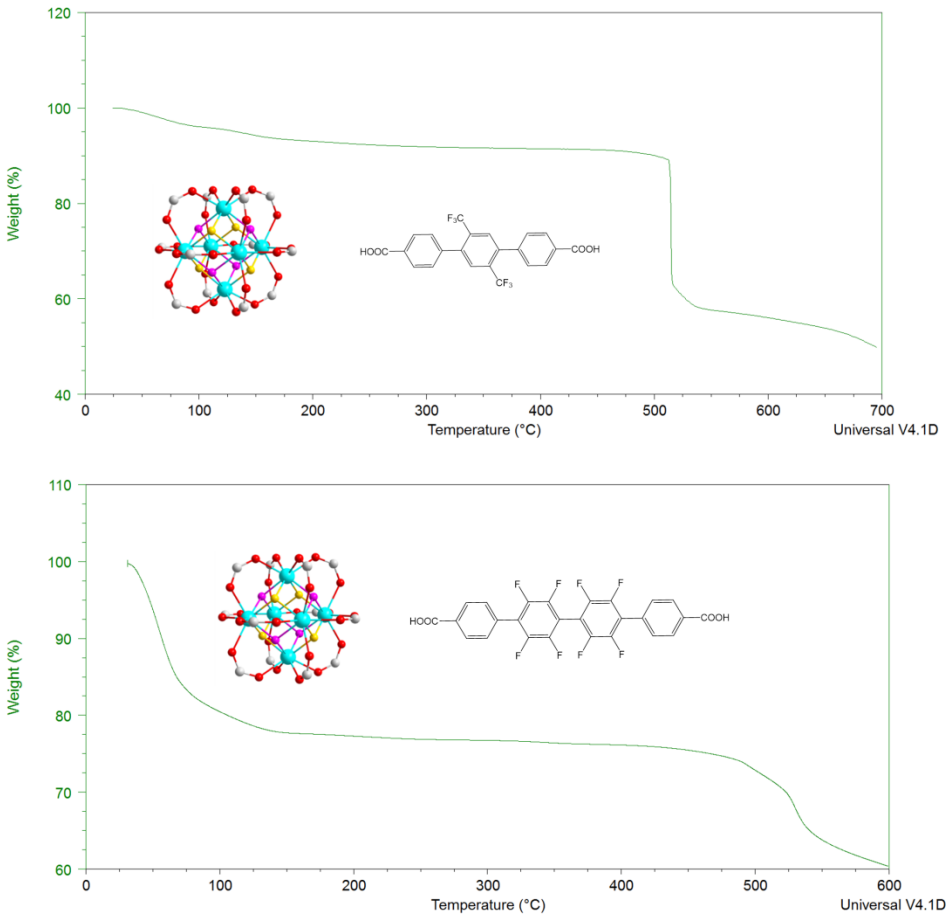

Figure 76. TGA curves of the two synthesized compounds.

N_2 adsorption measurements at 77 K confirmed the highly porous nature of the obtained two MOFs. Both materials show BET surface areas of ~ 3000 m^2/g (Figure 77-78). Interestingly, Zr-tpdc-$(CF_3)_2$ represents a very rear example of highly porous material with exceptional hydrophobicity. As shown in Figure 79, the activated form of Zr-tpdc-$(CF_3)_2$ does not readsorb water from air as no corresponding weight loss observed for the sample being exposed in air for 2 days. This indicates that the alkyl fluorinated functional group – CF_3 is more effective in enhancing the hydrophobicity of the MOF compared to aromatic fluoro atoms. We thus use Zr-tpdc-$(CF_3)_2$ for chlorocarbon (tetrachloroethylene, TCE) capture and removal since they are common water contaminant.

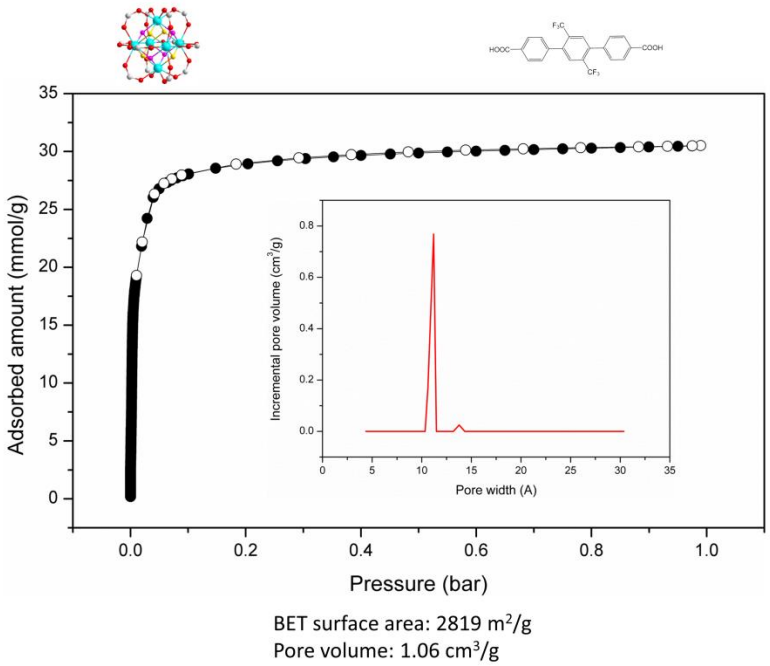

Figure 77. Porosity analysis of Zr-tpdc-$(CF_3)_2$ by N_2 adsorption measurement at 77 K.

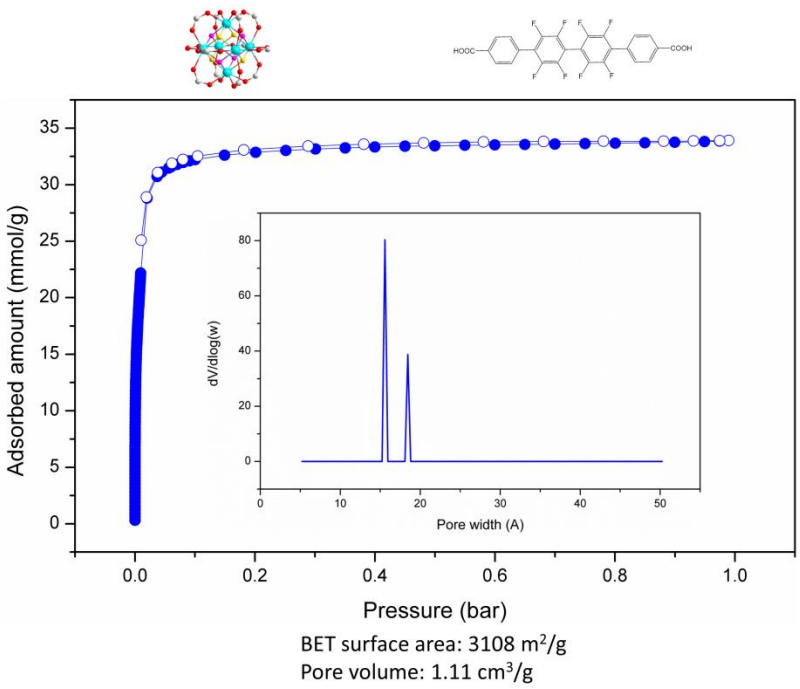

Figure 78. Porosity analysis of Zr-tpdc-F_8 by N_2 adsorption measurement at 77 K.

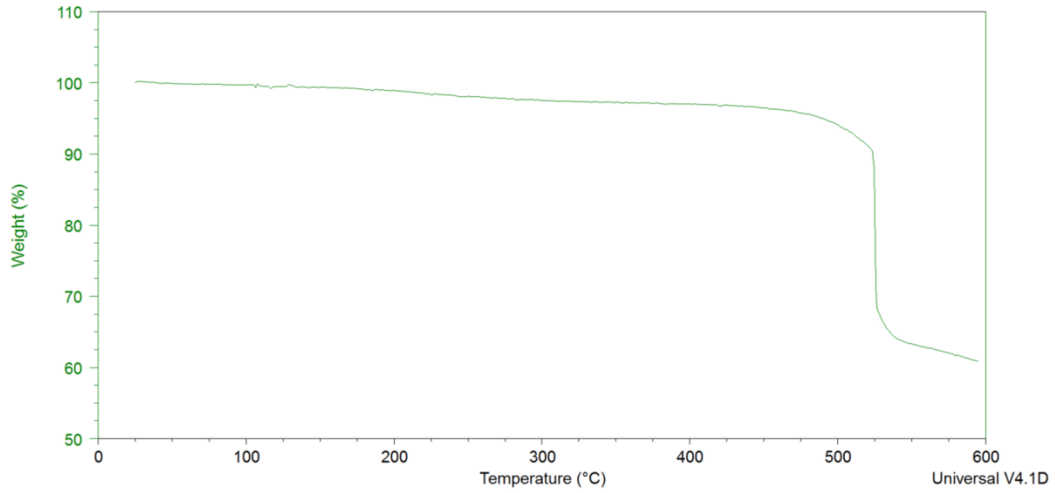

Figure 79. TGA curve of activated Zr-tpdc-$(CF_3)_2$ after being exposed in open air for 2 days.

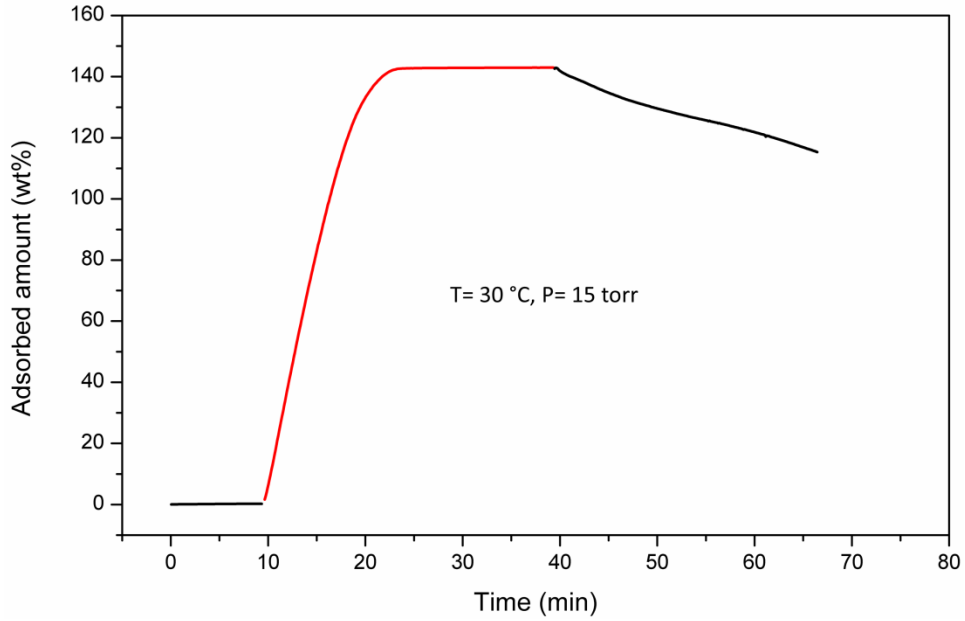

Figure 80. TCE adsorption on Zr-tpdc-$(CF_3)_2$ at 30 °C under a partial pressure of 15 torr.

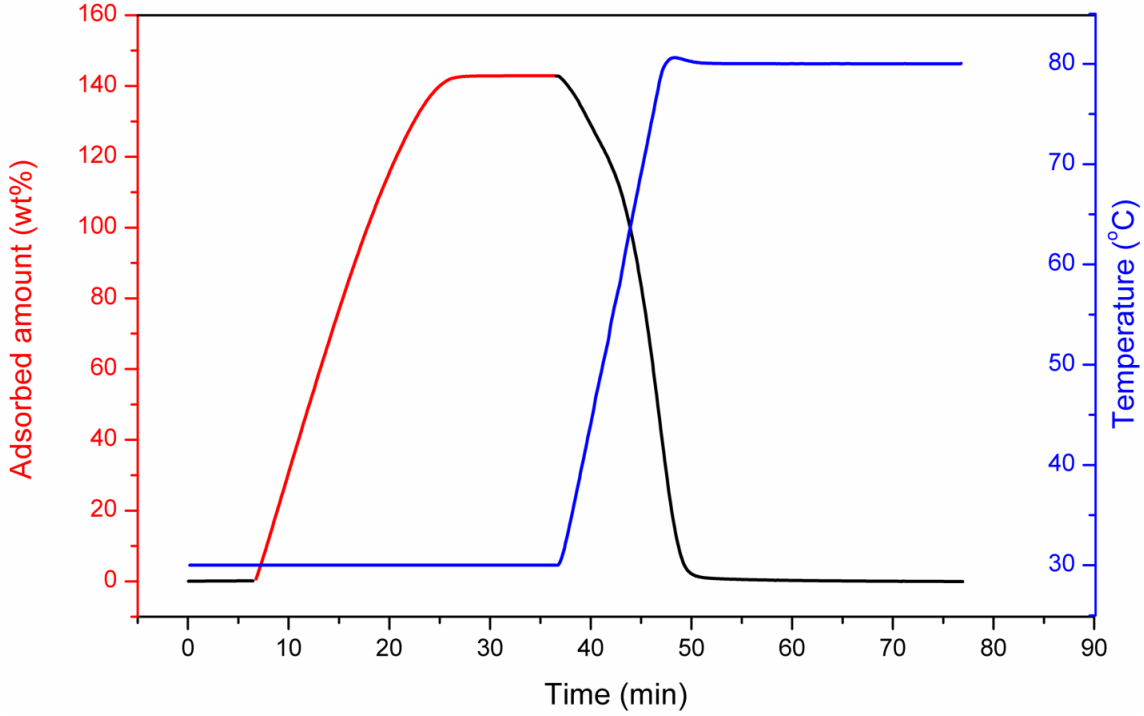

Figure 81. TCE adsorption (at 30 °C) and desorption (at 80°C) curves.

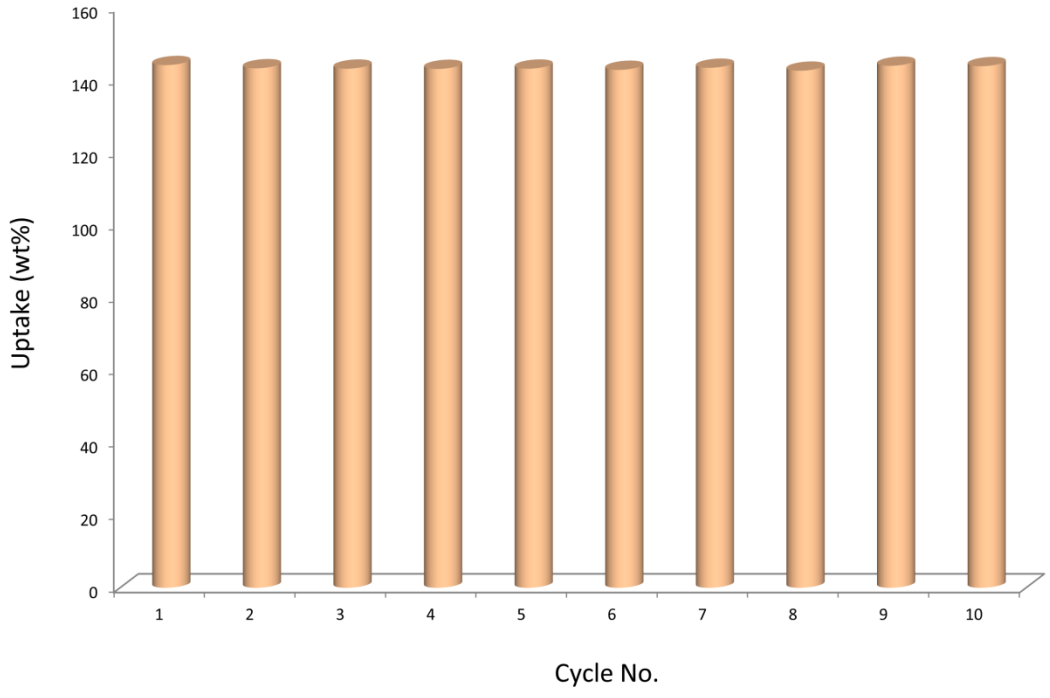

Figure 82. TCE adsorption-desorption cycles (adsorption: 30 °C and 15 torr, desorption: 80 °C under pure nitrogen).

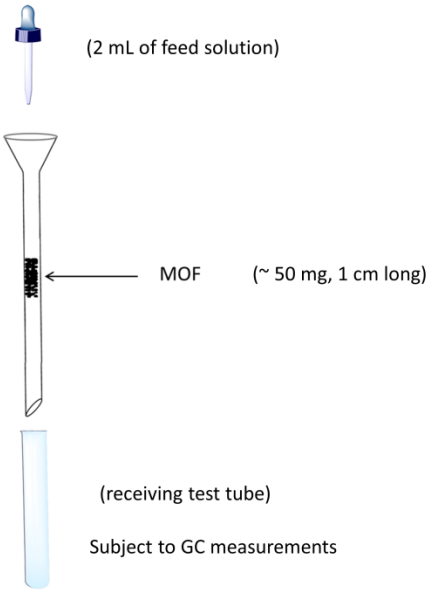

Figure 83. Schematic show of the setup for TCE removal.

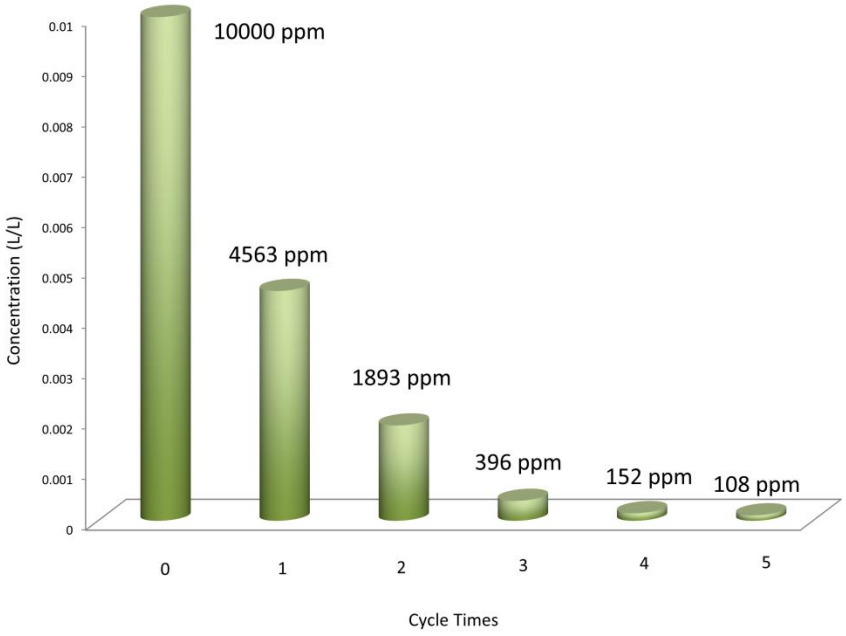

Figure 84. TCE removal results.

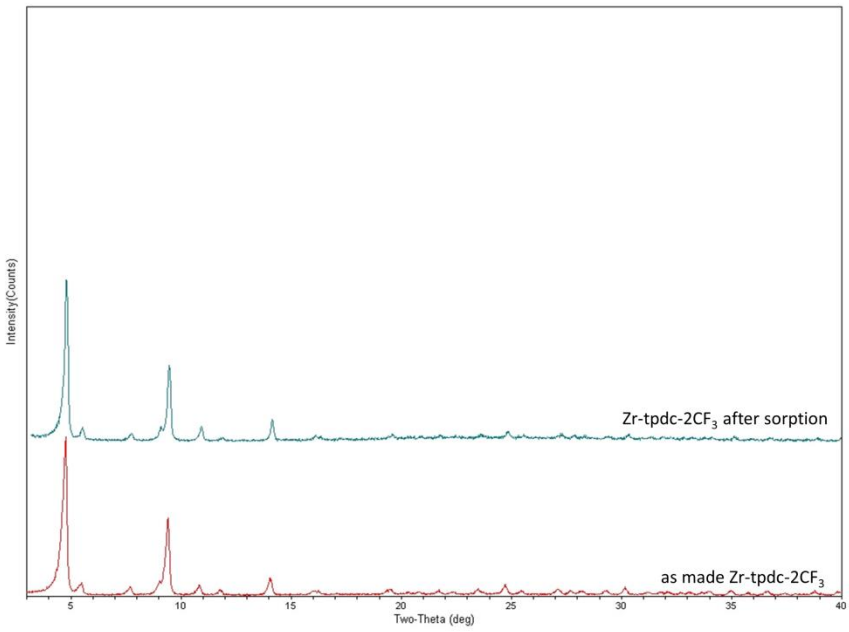

Figure 85. PXRD pattern of the Zr-tpdc-$(CF_3)_2$ sample after adsorption measurements.

As shown in Figure 80, at 30 °C Zr-tpdc-$(CF_3)_2$ adsorbs more than 140 wt% of TCE and most of the adsorbed TCE won't desorb upon short time nitrogen flush. This indicates the adsorbed TCE molecules are strongly held in the pore. However, when slight heat is applied, say 80 °C (Figure 81), all adsorbed TCE will desorb completely in minutes. Cycle test show that the material does not loss any capacity after 10 adsorption-desorption cycles, indicating the robustness of the adsorbent (Figure 82). We thus designed a simple setup to evaluate the feasibility of TCE removal. As the solubility of TCE in aqueous solution is extremely low, we use methanol as the solvent. For a typical measurement, 2 mL TCE methanol solution (known concentration) goes through a short column packed with activated MOF sample, and the receiving solution was subject to GC test of the TCE concentration. The results are shown in Figure 83. We started with a concentration of 1% (10000 ppm) and after five cycles, the TCE concentration in the solution has decreased to

~ 100 ppm. PXRD analysis was performed on the sample after adsorption measurements and the crystallinity of the sample was well maintained. These results suggest Zr-tpdc-$(CF_3)_2$ is a promising candidate for TCE removal.

6.3 Synthesis, structure, and fluorocarbon adsorption of a UiO-66 type Zr-MOF[106]

By applying reticular chemistry, we synthesized a new UiO-66 type structure with a linear dicarboxylate ligand (4-carboxycinnamic acid, H_2cca). Single crystal X-ray diffraction analysis reveals that the synthesized MOF, Zr-cca, employs the same connectivity as the porotype Zr-MOF, UiO-66.[50] It shows two types of pores, a tetrahedron cage and an octahedron cage, as shown in Figure 86. N_2 adsorption measurement at 77 K confirmed its permanent porosity which gives a BET surface area of 1178 m^2/g (Figure 87), comparable to that of UiO-66.

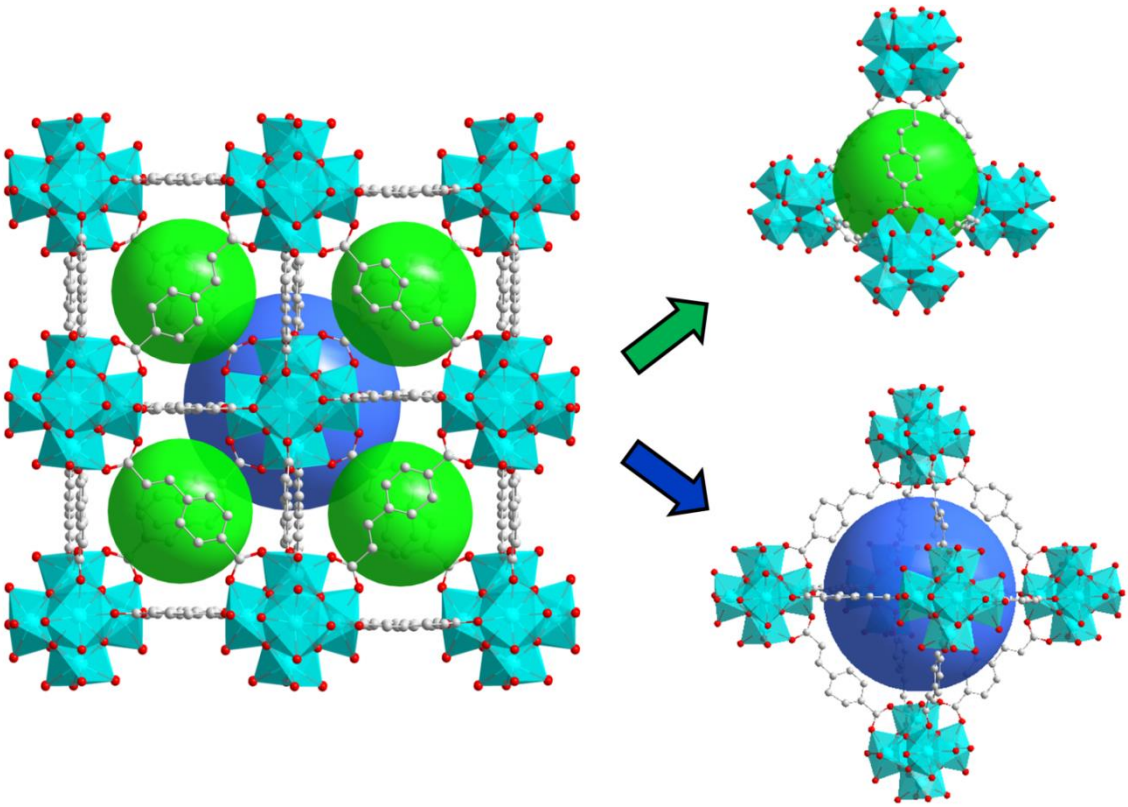

Figure 86. Crystal structure of Zr-cca. Green and blue spheres represent the tetrahedral and octahedral cages in the structure, respectively. Color scheme: cyan (Zr), red (O), grey (C). Hydrogen atoms are omitted for clarity.

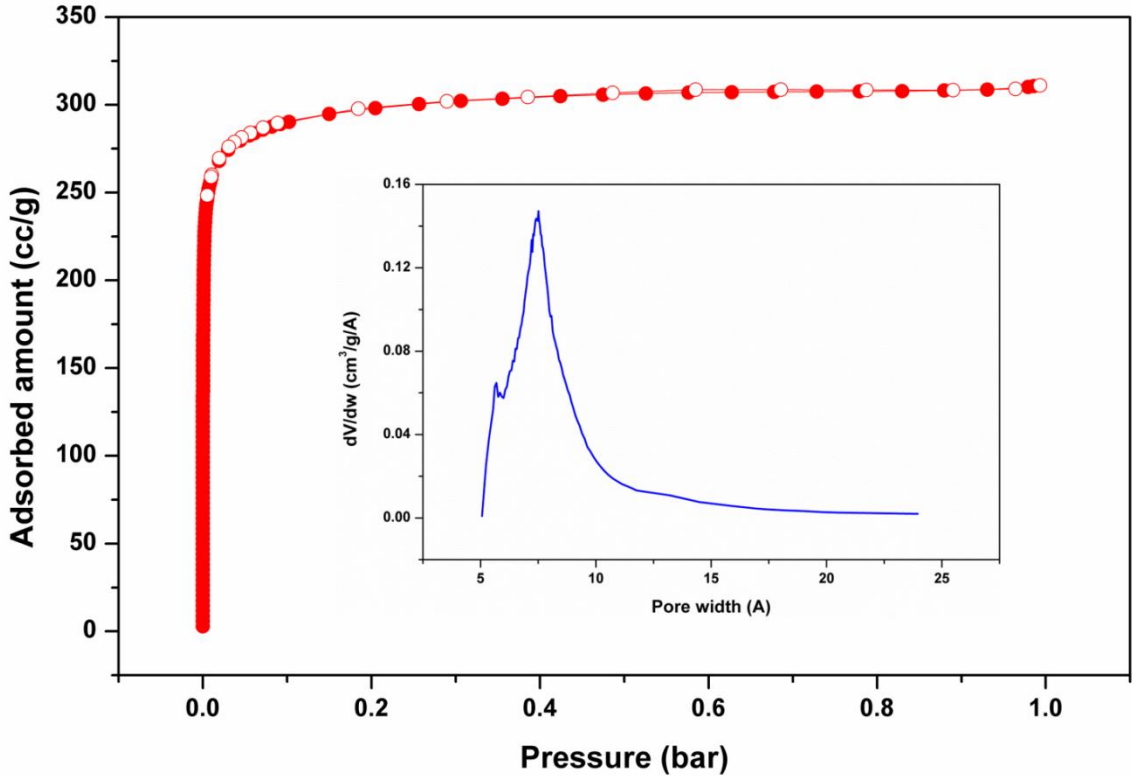

Figure 87. Nitrogen adsorption-desorption isotherm at 77 K for Zr-cca. Insert: pore size distribution.

We tested the ability of Zr-cca for the adsorption of perfluorohexane, a fluorocarbon is a potent greenhouse gas with much higher GWP than carbon dioxide. The results show the material can take up more than 50 wt% of perfluorohexane and after 10 adsorption-desorption cycles it does not loss any capacity. These results suggest that stable Zr-MOFs represent a family of promising porous solids for the capture sequestration of fluorocarbons.

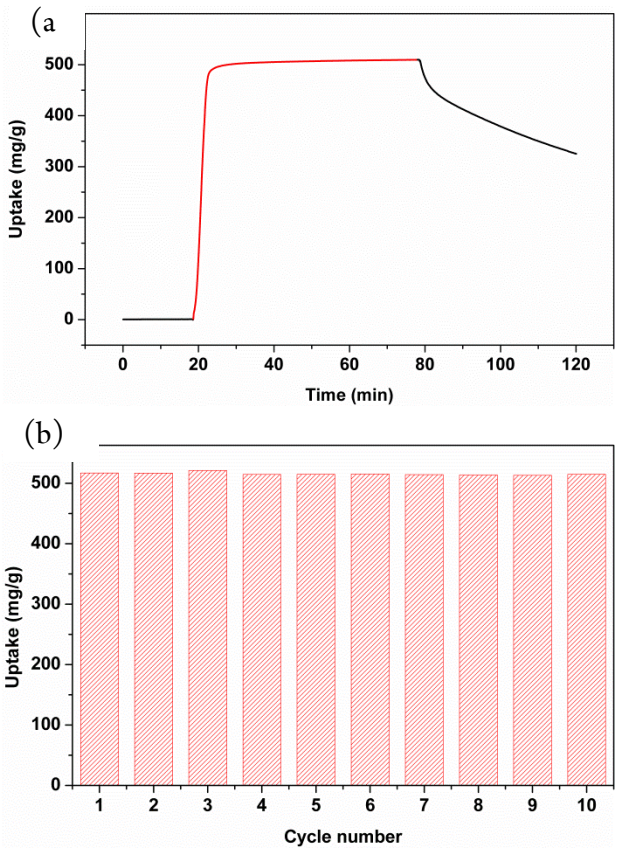

Figure 88. (a) Adsorption-desorption curve of perfluorohexane on Zr-cca at 30 °C. Black and red curves indicate pure nitrogen and a mixture of nitrogen and perfluorohexane vapor (partial pressure: 20 kPa) as feed gases, respectively. (b) Perfluorohexane adsorption cycles on Zr-cca. Desorption was carried out at 100°C for 30 min under nitrogen.

6.4 Optimization of the synthetic conditions of selected MOFs

1. $Co_3(HCOO)_6$

Single crystal growth: $Co(ClO_4)_2 \cdot 6H_2O$ (36.6 mg) was dissolved in 8 mL DMF in a 20 mL glass vial. 20 μL HCOOH and 4 mL 1,4-dioxane were added to the solution and the mixture was sonicated for 5 min and then placed in 120 °C oven for 2 days. Block shaped single crystals were obtained after cooling down to room temperature.

Synthesis of crystalline powder: 1.3 g $Co(NO_3)_2 \cdot 6H_2O$ was dissolved in 10 mL DMF in a 20 mL glass vial. 1 mL of formic acid was added and the mixture was sonicated for 5 min

and then placed in 100 °C oven for 24 hours. After the reaction cools down to room temperature crystalline powder was collected by centrifuge.

2. CaSDB

$CaCl_2$ (222 mg, 0.18 mmol) and H_2SDB (594 mg, 0.18 mmol) were added to 30 mL of 95% ethanol. The mixture was stirred for 2 hours to achieve homogeneity. The resultant solution was heated at 180 °C for 5 days. After cooling down to room temperature, colorless crystals were obtained.

3. $Mn(ina)_2$

$Mn(NO_3)_2 \cdot 4H_2O$ (142 mg) and Hina (128 mg) were added to 18 mL ethanol (95%) in a bomb. The mixture was sonicated and stirred for 2 hours before being placed in a 100 °C oven. The reaction took 1 day and block shaped crystals were obtained after cooling down to room temperature.

4. MOF-74 (Need methanol exchange for a week prior to adsorption study)

MOF-74-Zn: $Zn(NO_3)_2 \cdot 6H_2O$ (200 mg) and H_4DOBDC (50 mg) were dissolved in a mixture of 10 mL DMF and 0.5 mL H_2O. The reaction was placed in 100°C oven for 1 day.

MOF-74-Mg: $Mg(NO_3)_2 \cdot 6H_2O$ (160 mg) and H_4DOBDC (40 mg) were dissolved in a mixture of 15 mL DMF, 1.0 mL H_2O, and 1.0 mL ethanol. The reaction was placed in 120°C oven for 1 day.

MOF-74-Co: $Co(NO_3)_2 \cdot 6H_2O$ (120 mg) and H_4DOBDC (24 mg) were dissolved in a mixture of 3 mL DMF, 3 mL H_2O, and 3 mL ethanol. The reaction was placed in 100°C oven for 1 day.

MOF-74-Ni: $Ni(NO_3)_2 \cdot 6H_2O$ (120 mg) and H_4DOBDC (24 mg) were dissolved in a mixture of 3 mL DMF, 3 mL H_2O, and 3 mL ethanol. The reaction was placed in 100°C oven for 1 day.

References

1 Sing K.S.W., E. D. H., Haul R.A.W., Moscou L., Pierotti R.A., Rouquerol l. and & T., S. *Pure Appl. Chem* **57**, 603 (1985).

2 Sakintuna, B., Lamari-Darkrim, F. & Hirscher, M. Metal hydride materials for solid hydrogen storage: A review. *International Journal of Hydrogen Energy* **32**, 1121-1140 (2007).

3 Struzhkin, V. V., Militzer, B., Mao, W. L., Mao, H.-k. & Hemley, R. J. Hydrogen Storage in Molecular Clathrates. *Chemical Reviews* **107**, 4133-4151 (2007).

4 Chen, J. & Wu, F. Review of hydrogen storage in inorganic fullerene-like nanotubes. *Applied Physics A* **78**, 989-994 (2004).

5 Murray, L. J., Dinca, M. & Long, J. R. Hydrogen storage in metal-organic frameworks. *Chemical Society Reviews* **38**, 1294-1314 (2009).

6 Suh, M. P., Park, H. J., Prasad, T. K. & Lim, D.-W. Hydrogen Storage in Metal–Organic Frameworks. *Chemical Reviews* **112**, 782-835 (2012).

7 Herm, Z. R., Bloch, E. D. & Long, J. R. Hydrocarbon Separations in Metal–Organic Frameworks. *Chemistry of Materials* **26**, 323-338 (2014).

8 Li, H., Eddaoudi, M., O'Keeffe, M. & Yaghi, O. M. Design and synthesis of an exceptionally stable and highly porous metal-organic framework. *Nature* **402**, 276-279 (1999).

9 Chui, S. S. A Chemically Functionalizable Nanoporous Material [Cu3(TMA)2(H2O)3]n. *Science* **283**, 1148-1150 (1999).

10 Furukawa, H., Cordova, K. E., O'Keeffe, M. & Yaghi, O. M. The Chemistry and Applications of Metal-Organic Frameworks. *Science* **341** (2013).

11 Zhou, H.-C., Long, J. R. & Yaghi, O. M. Introduction to Metal–Organic Frameworks. *Chemical Reviews* **112**, 673-674 (2012).

12 Yaghi, O. M. *et al.* Reticular synthesis and the design of new materials. *Nature* **423**, 705-714 (2003).

13 O'Keeffe, M. & Yaghi, O. M. Deconstructing the Crystal Structures of Metal–Organic Frameworks and Related Materials into Their Underlying Nets. *Chemical Reviews* **112**, 675-702 (2012).

14 Stock, N. & Biswas, S. Synthesis of Metal-Organic Frameworks (MOFs): Routes to Various MOF Topologies, Morphologies, and Composites. *Chemical Reviews* **112**, 933-969 (2012).

15 Klinowski, J., Almeida Paz, F. A., Silva, P. & Rocha, J. Microwave-Assisted Synthesis of Metal-Organic Frameworks. *Dalton Transactions* **40**, 321-330 (2011).

16 Sun, J.-K. *et al.* Mechanical grinding of a single-crystalline metal-organic framework triggered emission with tunable violet-to-orange luminescence. *Chemical Communications* **50**, 15956-15959 (2014).

17 Schoedel, A., Li, M., Li, D., O'Keeffe, M. & Yaghi, O. M. Structures of Metal–Organic Frameworks with Rod Secondary Building Units. *Chemical Reviews* **116**, 12466-12535 (2016).

18 Davies, R. P., Less, R., Lickiss, P. D., Robertson, K. & White, A. J. P. Structural Diversity in Metal−Organic Frameworks Built from Rigid Tetrahedral [Si(p-C6H4CO2)4]4− Struts. *Crystal Growth & Design* **10**, 4571-4581 (2010).

19 Marin, G. *et al.* Structural Diversity in Metal−Organic Frameworks Derived from Binuclear Alkoxo-Bridged Copper(II) Nodes and Pyridyl Linkers. *Crystal Growth & Design* **8**, 964-975 (2008).

20 Li, B., Wen, H.-M., Zhou, W. & Chen, B. Porous Metal–Organic Frameworks for Gas Storage and Separation: What, How, and Why? *The Journal of Physical Chemistry Letters* **5**, 3468-3479 (2014).

21 Ma, S. & Zhou, H.-C. Gas storage in porous metal-organic frameworks for clean energy applications. *Chemical Communications* **46**, 44-53 (2010).

22 Peng, Y. *et al.* Methane Storage in Metal–Organic Frameworks: Current Records, Surprise Findings, and Challenges. *Journal of the American Chemical Society* **135**, 11887-11894 (2013).

23 Li, J.-R., Kuppler, R. J. & Zhou, H.-C. Selective gas adsorption and separation in metal-organic frameworks. *Chemical Society Reviews* **38**, 1477-1504 (2009).

24 Sumida, K. *et al.* Carbon Dioxide Capture in Metal–Organic Frameworks. *Chemical Reviews* **112**, 724-781 (2012).

25 Lustig, W. P. *et al.* Chromophore-Based Luminescent Metal–Organic Frameworks as Lighting Phosphors. *Inorganic Chemistry* **55**, 7250-7256 (2016).

26 Sun, C.-Y. *et al.* Efficient and tunable white-light emission of metal–organic frameworks by iridium-complex encapsulation. **4**, 2717 (2013).

27 Gong, Q. *et al.* Solution Processable MOF Yellow Phosphor with Exceptionally High Quantum Efficiency. *Journal of the American Chemical Society* **136**, 16724-16727 (2014).

28 Huang, Y.-B., Liang, J., Wang, X.-S. & Cao, R. Multifunctional metal-organic framework catalysts: synergistic catalysis and tandem reactions. *Chemical Society Reviews* **46**, 126-157 (2017).

29 Ranocchiari, M. & Bokhoven, J. A. v. Catalysis by metal-organic frameworks: fundamentals and opportunities. *Physical Chemistry Chemical Physics* **13**, 6388-6396 (2011).

30 Shimizu, G. K. H., Taylor, J. M. & Kim, S. Proton Conduction with Metal-Organic Frameworks. *Science* **341**, 354-355 (2013).

31 Taylor, J. M., Dekura, S., Ikeda, R. & Kitagawa, H. Defect Control To Enhance Proton Conductivity in a Metal–Organic Framework. *Chemistry of Materials* **27**, 2286-2289 (2015).

32 Horcajada, P. *et al.* Porous metal-organic-framework nanoscale carriers as a potential platform for drug delivery and imaging. *Nat Mater* **9**, 172-178 (2010).

33 Rojas, S. *et al.* Nanoscaled Zinc Pyrazolate Metal–Organic Frameworks as Drug-Delivery Systems. *Inorganic Chemistry* **55**, 2650-2663 (2016).

34 Farha, O. K. *et al.* Metal–Organic Framework Materials with Ultrahigh Surface Areas: Is the Sky the Limit? *Journal of the American Chemical Society* **134**, 15016-15021 (2012).

35 Shekhah, O. *et al.* Made-to-order metal-organic frameworks for trace carbon dioxide removal and air capture. **5**, 4228 (2014).

36 McDonald, T. M. *et al.* Cooperative insertion of CO2 in diamine-appended metal-organic frameworks. *Nature* **519**, 303-308 (2015).

37 Planas, N. *et al.* The Mechanism of Carbon Dioxide Adsorption in an Alkylamine-Functionalized Metal–Organic Framework. *Journal of the American Chemical Society* **135**, 7402-7405 (2013).

38 McDonald, T. M. *et al.* Capture of Carbon Dioxide from Air and Flue Gas in the Alkylamine-Appended Metal–Organic Framework mmen-Mg2(dobpdc). *Journal of the American Chemical Society* **134**, 7056-7065 (2012).

39 Cadiau, A., Adil, K., Bhatt, P. M., Belmabkhout, Y. & Eddaoudi, M. A metal-organic framework–based splitter for separating propylene from propane. *Science* **353**, 137-140 (2016).

40 Assen, A. H. *et al.* Ultra-Tuning of the Rare-Earth fcu-MOF Aperture Size for Selective Molecular Exclusion of Branched Paraffins. *Angewandte Chemie International Edition* **54**, 14353-14358 (2015).

41 Vaughn, J. *et al.* Encapsulated recyclable porous materials: an effective moisture-triggered fragrance release system. *Chemical Communications* **49**, 5724-5726 (2013).

42 Yee, K.-K. *et al.* Effective Mercury Sorption by Thiol-Laced Metal–Organic Frameworks: in Strong Acid and the Vapor Phase. *Journal of the American Chemical Society* **135**, 7795-7798 (2013).

43 Myers, R. A. *Handbook of Petroleum Refining Processes*. (McGraw-Hill, 2004).

44 Herm, Z. R. *et al.* Separation of Hexane Isomers in a Metal-Organic Framework with Triangular Channels. *Science* **340**, 960-964 (2013).

45 Silva, J. A. C. & Rodrigues, A. E. Equilibrium and kinetics ofn– hexane sorption in pellets of 5A zeolite. *AIChE J.* **43**, 2524-2534 (1997).

46 Burtch, N. C., Jasuja, H. & Walton, K. S. Water Stability and Adsorption in Metal–Organic Frameworks. *Chemical Reviews* **114**, 10575-10612 (2014).

47 Kizzie, A. C., Wong-Foy, A. G. & Matzger, A. J. Effect of Humidity on the Performance of Microporous Coordination Polymers as Adsorbents for CO2 Capture. *Langmuir* **27**, 6368-6373 (2011).

48 Wang, C., Liu, X., Keser Demir, N., Chen, J. P. & Li, K. Applications of water stable metal-organic frameworks. *Chemical Society Reviews* **45**, 5107-5134 (2016).

49 Bai, Y. *et al.* Zr-based metal-organic frameworks: design, synthesis, structure, and applications. *Chemical Society Reviews* (2016).

50 Cavka, J. H. *et al.* A New Zirconium Inorganic Building Brick Forming Metal Organic Frameworks with Exceptional Stability. *Journal of the American Chemical Society* **130**, 13850-13851 (2008).

51 Zhang, Q. *et al.* Piezofluorochromic Metal–Organic Framework: A Microscissor Lift. *Journal of the American Chemical Society* **137**, 10064-10067 (2015).

52 Zheng, J., Wu, M., Jiang, F., Su, W. & Hong, M. Stable porphyrin Zr and Hf metal-organic frameworks featuring 2.5 nm cages: high surface areas, SCSC transformations and catalyses. *Chemical Science* **6**, 3466-3470 (2015).

53 Wang, B. *et al.* Highly Stable Zr(IV)-Based Metal–Organic Frameworks for the Detection and Removal of Antibiotics and Organic Explosives in Water. *Journal of the American Chemical Society* **138**, 6204-6216 (2016).

54 Ma, J., Tran, L. D. & Matzger, A. J. Toward Topology Prediction in Zr-Based Microporous Coordination Polymers: The Role of Linker Geometry and Flexibility. *Cryst. Growth Des.* **16**, 4148-4153 (2016).

55 Huang, Y.-G. *et al.* Thermally Induced Intra-Carboxyl Proton Shuttle in a Molecular Rack-and-Pinion Cascade Achieving Macroscopic Crystal Deformation. *Angew. Chem. Int. Ed.* **55**, 14628-14632 (2016).

56 Miller, S. R. *et al.* A rare example of a porous Ca-MOF for the controlled release of biologically active NO. *Chem. Commun.* **49**, 7773-7775 (2013).

57 He, Y., Li, B., O'Keeffe, M. & Chen, B. Multifunctional metal-organic frameworks constructed from meta-benzenedicarboxylate units. *Chemical Society Reviews* **43**, 5618-5656 (2014).

58 Pal, T. K., Neogi, S. & Bharadwaj, P. K. Versatile Tailoring of Paddle-Wheel ZnII Metal–Organic Frameworks through Single-Crystal-to-Single-Crystal Transformations. *Chem. Eur. J.* **21**, 16083-16090 (2015).

59 Wen, H.-M. *et al.* A microporous metal-organic framework with rare lvt topology for highly selective C2H2/C2H4 separation at room temperature. *Chem. Commun.* **51**, 5610-5613 (2015).

60 Mendes, P. A. P., Rodrigues, A. E., Horcajada, P., Serre, C. & Silva, J. A. C. Single and multicomponent adsorption of hexane isomers in the microporous ZIF-8. *Micro. Meso. Mater.* **194**, 146-156 (2014).

61 Lane, G. *et al.* Anesthetics as teratogens: nitrous oxide is fetotoxic, xenon is not. *Science* **210**, 899-901 (1980).

62 Fontaine, J. P., Pointurier, F., Blanchard, X. & Taffary, T. Atmospheric xenon radioactive isotope monitoring. *Journal of Environmental Radioactivity* **72**, 129-135 (2004).

63 Marshall, J. & Bird, A. C. A comparative histopathological study of argon and krypton laser irradiations of the human retina. *British Journal of Ophthalmology* **63**, 657-668 (1979).

64 Saxton, C. G., Kruth, A., Castro, M., Wright, P. A. & Howe, R. F. Xenon adsorption in synthetic chabazite zeolites. *Microporous and Mesoporous Materials* **129**, 68-73 (2010).

65 Couderc, G., Hertzsch, T., Behrnd, N. R., Krämer, K. & Hulliger, J. Reversible sorption of nitrogen and xenon gas by the guest-free zeolite tris(o-phenylenedioxy)cyclotriphosphazene (TPP). *Microporous and Mesoporous Materials* **88**, 170-175 (2006).

66 Liu, J., Thallapally, P. K. & Strachan, D. Metal–Organic Frameworks for Removal of Xe and Kr from Nuclear Fuel Reprocessing Plants. *Langmuir* **28**, 11584-11589 (2012).

67 Sikora, B. J., Wilmer, C. E., Greenfield, M. L. & Snurr, R. Q. Thermodynamic analysis of Xe/Kr selectivity in over 137 000 hypothetical metal-organic frameworks. *Chemical Science* **3**, 2217-2223 (2012).

68 Li, K. *et al.* Multifunctional Microporous MOFs Exhibiting Gas/Hydrocarbon Adsorption Selectivity, Separation Capability and Three-Dimensional Magnetic Ordering. *Advanced Functional Materials* **18**, 2205-2214 (2008).

69 Zhang, Z., Liu, J., Li, Z. & Li, J. Experimental and theoretical investigations on the MMOF selectivity for CO2vs. N2 in flue gas mixtures. *Dalton Transactions* **41**, 4232-4238 (2012).

70 Myers, A. L. & Prausnitz, J. M. Thermodynamics of mixed-gas adsorption. *AIChE Journal* **11**, 121-127 (1965).

71 Heuchel, M., Snurr, R. Q. & Buss, E. Adsorption of CH4−CF4 Mixtures in Silicalite: Simulation, Experiment, and Theory. *Langmuir* **13**, 6795-6804 (1997).

72 Bae, Y.-S. *et al.* Separation of CO2 from CH4 Using Mixed-Ligand Metal−Organic Frameworks. *Langmuir* **24**, 8592-8598 (2008).

73 Bae, Y.-S. *et al.* Carborane-based metal-organic frameworks as highly selective sorbents for CO2 over methane. *Chemical Communications*, 4135-4137 (2008).

74 Chen, J., Loo, L. S. & Wang, K. An Ideal Absorbed Solution Theory (IAST) Study of Adsorption Equilibria of Binary Mixtures of Methane and Ethane on a Templated Carbon. *Journal of Chemical & Engineering Data* **56**, 1209-1212 (2011).

75 Chen, H. & Sholl, D. S. Examining the Accuracy of Ideal Adsorbed Solution Theory without Curve-Fitting Using Transition Matrix Monte Carlo Simulations. *Langmuir* **23**, 6431-6437 (2007).

76 Mason, J. A., Sumida, K., Herm, Z. R., Krishna, R. & Long, J. R. Evaluating metal-organic frameworks for post-combustion carbon dioxide capture via temperature swing adsorption. *Energy & Environmental Science* **4**, 3030-3040 (2011).

77 Wang, H. *et al.* The first example of commensurate adsorption of atomic gas in a MOF and effective separation of xenon from other noble gases. *Chemical Science* **5**, 620-624 (2014).

78 Carrington, E. J. *et al.* Solvent-switchable continuous-breathing behaviour in a diamondoid metal–organic framework and its influence on CO2 versus CH4 selectivity. *Nat Chem* advance online publication (2017).

79 Schneemann, A. *et al.* Flexible metal-organic frameworks. *Chemical Society Reviews* **43**, 6062-6096 (2014).

80 Chang, Z., Yang, D.-H., Xu, J., Hu, T.-L. & Bu, X.-H. Flexible Metal–Organic Frameworks: Recent Advances and Potential Applications. *Advanced Materials* **27**, 5432-5441 (2015).

81 Mason, J. A. *et al.* Methane storage in flexible metal–organic frameworks with intrinsic thermal management. *Nature* **527**, 357-361 (2015).

82 Bezuidenhout, C. X., Smith, V. J., Esterhuysen, C. & Barbour, L. J. Solvent- and Pressure-Induced Phase Changes in Two 3D Copper Glutarate-Based Metal–Organic Frameworks via Glutarate (+gauche ⇄ −gauche) Conformational Isomerism. *Journal of the American Chemical Society* **139**, 5923-5929 (2017).

83 Nijem, N. *et al.* Understanding the Preferential Adsorption of CO2 over N2 in a Flexible Metal–Organic Framework. *Journal of the American Chemical Society* **133**, 12849-12857 (2011).

84 Nijem, N. *et al.* Spectroscopic Evidence for the Influence of the Benzene Sites on Tightly Bound H2 in Metal−Organic Frameworks with Unsaturated Metal Centers: MOF-74-Cobalt. *Journal of the American Chemical Society* **133**, 4782-4784 (2011).

85 Vanduyfhuys, L., Verstraelen, T., Vandichel, M., Waroquier, M. & Van Speybroeck, V. Ab Initio Parametrized Force Field for the Flexible Metal–Organic Framework MIL-53(Al). *Journal of Chemical Theory and Computation* **8**, 3217-3231 (2012).

86 Banerjee, D. *et al.* Direct structural evidence of commensurate-to-incommensurate transition of hydrocarbon adsorption in a microporous metal organic framework. *Chemical Science* **7**, 759-765 (2016).

87 Banerjee, D. *et al.* Direct Structural Identification of Gas Induced Gate-Opening Coupled with Commensurate Adsorption in a Microporous Metal–Organic Framework. *Chemistry – A European Journal* **22**, 11816-11825 (2016).

88 Plonka, A. M. *et al.* Mechanism of Carbon Dioxide Adsorption in a Highly Selective Coordination Network Supported by Direct Structural Evidence. *Angewandte Chemie International Edition* **52**, 1692-1695 (2013).

89 Gálvez, A., Abriouel, H., López, R. L. & Omar, N. B. Bacteriocin-based strategies for food biopreservation. *International Journal of Food Microbiology* **120**, 51-70 (2007).

90 Holley, R. A. & Patel, D. Improvement in shelf-life and safety of perishable foods by plant essential oils and smoke antimicrobials. *Food Microbiology* **22**, 273-292 (2005).

91 Hasegawa, N., Matsumoto, Y., Hoshino, A. & Iwashita, K. Comparison of effects of Wasabia japonica and allyl isothiocyanate on the growth of four strains of Vibrio parahaemolyticus in lean and fatty tuna meat suspensions. *International Journal of Food Microbiology* **49**, 27-34 (1999).

92 Jordt, S.-E. *et al.* Mustard oils and cannabinoids excite sensory nerve fibres through the TRP channel ANKTM1. *Nature* **427**, 260-265 (2004).

93 LIN, C.-M., KIM, J., DU, W.-X. & WEI, C.-I. Bactericidal Activity of Isothiocyanate against Pathogens on Fresh Produce. *Journal of Food Protection* **63**, 25-30 (2000).

94 LIN, C.-M., JAMES F. PRESTON III & WEI, C.-I. Antibacterial Mechanism of Allyl Isothiocyanate. *Journal of Food Protection* **63**, 727-734 (2000).

95 Nadarajah, D., Han, J. H. & Holley, R. A. Inactivation of Escherichia coli O157:H7 in packaged ground beef by allyl isothiocyanate. *International Journal of Food Microbiology* **99**, 269-279 (2005).

96 Park, S.-Y. & Pendleton, P. Mesoporous silica SBA-15 for natural antimicrobial delivery. *Powder Technology* **223**, 77-82 (2012).

97 Siahaan, E. A. *et al.* Controlled release of allyl isothiocyanate from brown algae Laminaria japonica and mesoporous silica MCM-41 for inhibiting food-borne bacteria. *Food Science and Biotechnology* **22**, 19-24 (2013).

98 Pan, L. *et al.* ℝPM-1: A Recyclable Nanoporous Material Suitable for Ship-In-Bottle Synthesis and Large Hydrocarbon Sorption. *Angewandte Chemie International Edition* **42**, 542-546 (2003).

99 Lan, A. *et al.* ℝPM3: A Multifunctional Microporous MOF with Recyclable Framework and High H2 Binding Energy. *Inorganic Chemistry* **48**, 7165-7173 (2009).

100 Siahaan, E. A., Pendleton, P., Woo, H.-C. & Chun, B.-S. Brown seaweed (Saccharina japonica) as an edible natural delivery matrix for allyl isothiocyanate inhibiting food-borne bacteria. *Food Chemistry* **152**, 11-17 (2014).

101 Park, S.-Y., Barton, M. & Pendleton, P. Mesoporous silica as a natural antimicrobial carrier. *Colloids and Surfaces A: Physicochemical and Engineering Aspects* **385**, 256-261 (2011).

102 Wang, H. *et al.* The moisture-triggered controlled release of a natural food preservative from a microporous metal-organic framework. *Chemical Communications* **52**, 2129-2132 (2016).

103 Plonka, A. M. *et al.* Light Hydrocarbon Adsorption Mechanisms in Two Calcium-Based Microporous Metal Organic Frameworks. *Chemistry of Materials* **28**, 1636-1646 (2016).
104 Chen, X. *et al.* Direct Observation of Xe and Kr Adsorption in a Xe-Selective Microporous Metal–Organic Framework. *Journal of the American Chemical Society* **137**, 7007-7010 (2015).
105 Ockwig, N. W., Delgado-Friedrichs, O., O'Keeffe, M. & Yaghi, O. M. Reticular Chemistry: Occurrence and Taxonomy of Nets and Grammar for the Design of Frameworks. *Accounts of Chemical Research* **38**, 176-182 (2005).
106 Wang, H., Wang, Q., Teat, S. J., Olson, D. H. & Li, J. Synthesis, Structure, and Selective Gas Adsorption of a Single-Crystalline Zirconium Based Microporous Metal–Organic Framework. *Crystal Growth & Design* **17**, 2034-2040 (2017).

Acknowledgements of Previous Publications

Chapter 3 is adapted from reference 77. Copyright 2014 The Royal Society of Chemistry

Chapter 5 is adapted from reference 102. Copyright 2016 The Royal Society of Chemistry

Chapter 6.3 is adapted from reference 106. Copyright 2016 American Chemical Society.

Chapter 2, 4, 6 will be published in the near future.